

## UNCLASSIFIED

SECURITY CLASSIFICATION OF THIS PAGE (When Data Entered)

REPORT DOCUMENTATION PAGE		READ INSTRUCTIONS BEFORE COMPLETING FORM
1. REPORT NUMBER NORDA Report 51	2. GOVT ACCESSION NO.	3. RECIPIENT'S CATALOG NUMBER
4. TITLE (and Subtitle) Digital Processing of Passive Ka-band Microwave Images for Sea-Ice Classification		5. TYPE OF REPORT & PERIOD COVERED  FINAL
		6. PERFORMING ORG. REPORT NUMBER
7. AUTHOR(s) Duane T. Eppler                      Mervyn Hoover* L. Dennis Farmer Alan W. Lohanick		8. CONTRACT OR GRANT NUMBER(s)
9. PERFORMING ORGANIZATION NAME AND ADDRESS Naval Ocean Research & Development Activity Ocean Science Directorate NSTL, Mississippi 39529		10. PROGRAM ELEMENT, PROJECT, TASK AREA & WORK UNIT NUMBERS  PE 61153N
11. CONTROLLING OFFICE NAME AND ADDRESS  Same		12. REPORT DATE May 1984
		13. NUMBER OF PAGES 54
14. MONITORING AGENCY NAME & ADDRESS (if different from Controlling Office)		15. SECURITY CLASS. (of this report)  UNCLASSIFIED
		15a. DECLASSIFICATION/DOWNGRADING SCHEDULE
16. DISTRIBUTION STATEMENT (of this Report)  Approved for public release Distribution unlimited		
17. DISTRIBUTION STATEMENT (of the abstract entered in Block 20, if different from Report)		
18. SUPPLEMENTARY NOTES  *Attached to the Naval Weapons Center, China Lake, California		
19. KEY WORDS (Continue on reverse side if necessary and identify by block number)  Arctic      Ice classification KRMS      Beaufort Sea Sea-ice		
20. ABSTRACT (Continue on reverse side if necessary and identify by block number) The primary objective of NORDA's Ka-band Radiometric Mapping System (KRMS) program is to provide basic research needed for Navy development of an operational imaging system that can produce detailed information concerning ice conditions over broad regions of the Arctic. To this end, methods suitable for automated identification and classification of sea ice types and open water are being developed. An experimental plan has been formulated that will lead to an automated system to provide real-time ice classification information onboard Navy aircraft. This report represents completion of the initial state of this plan.		

NORDA Report 51

# **Digital Processing of Passive $K_a$ -band Microwave Images for Sea-Ice Classification**

**Duane T. Eppler  
L. Dennis Farmer  
Alan W. Lohanick**

Oceanography Division  
Ocean Science Directorate

**Mervyn Hoover**

Naval Weapons Center  
China Lake, California

MAY 1984



Approved for Public Release  
Distribution Unlimited

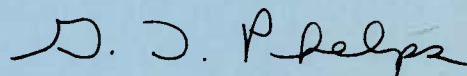
Naval Ocean Research and Development Activity  
NSTL, Mississippi 39529

# Foreword

---

Field trials of an airborne passive-microwave imaging system (MICRAD) in April 1976 demonstrated the utility of K-band microwave imagery as an all-weather reconnaissance tool in polar regions. In 1978 Dr. J. P. Welsh of NORDA, with sponsorship from Mr. Charles Luther (ONR) and Dr. Herbert Eppert (NORDA), began a long-term 6.1 research program directed toward application of passive microwave imagery to Arctic naval problems. A new imaging instrument, designated the K-band Microwave Imaging System (KRMS), was developed as part of this program by engineers at Naval Weapons Center, China Lake, California, with support from CNR (Admiral Albert J. Baciocco) and OP-952 (Rear Admiral Ross Williams). Engineering field tests of the KRMS were completed in December 1982. First use of the KRMS in support of an Arctic research experiment occurred in March 1983. Results of this experiment are presented here.

This work reaffirms the efficacy of K-band passive microwave images to polar research and reconnaissance. Image processing techniques and sea ice classification schemes suggested here illustrate the applicability of airborne single-band microwave sensors for operational reconnaissance of sea ice conditions. Continuation of this effort is being sponsored by NAVMAT (Captain John Harlett) through NAVAIR (Mr. Barry Dillon).



G. T. Phelps, Captain, USN  
Commanding Officer, NORDA

# Executive summary

---

The primary objective of NORDA's  $K_a$ -band Radiometric Mapping System (KRMS) program is to provide basic research needed for Navy development of an operational imaging system that can produce detailed information concerning ice conditions over broad regions of the Arctic. To this end, methods suitable for automated identification and classification of sea ice types and open water are being developed. An experimental plan has been formulated that will lead to an automated system that will provide real-time ice classification information onboard Navy aircraft. This report represents completion of the initial state of this plan.

During March 1983 extensive high-quality KRMS imagery and coincident high-resolution photography were obtained of ice in the Beaufort Sea. Analysis of these data suggests that four classes of winter surfaces can be distinguished solely on the basis of  $K_a$ -band brightness temperature: open water, frazil, old ice, and young/first-year ice. New ice (excluding frazil) and nilas display brightness temperatures that overlap the range of temperatures characteristic of old ice and young/first-year ice. Scenes in which new ice or nilas are present in appreciable amounts are subject to substantial errors in classification. Textural characteristics of nilas and new ice, however, differ significantly from textural features characteristic of other ice types and probably can be used with brightness temperature data to classify single-band microwave images.

# Acknowledgments

---

Bruce Heydlauff of Naval Weapons Center, China Lake, California, served as KRMS engineer during collection of the March 1983 data and provided needed expertise in signal processing theory. John Seybold of Naval Weapons Center, China Lake, converted analog KRMS data to digital images. Assistance required to operate NORDA's I<sup>2</sup>S image processing facility was provided by Remote Sensing Branch personnel (Robert Arnone, Ronald Holyer, Jeffrey Hawkins, John Schmidt, Gerald Stevenson) and by Computer Sciences Corporation contractor personnel (Nita Chase, Ramon "Sam" Oriol). Figures were drafted by Sheila Kahle and Maryellen Turcotte. Critical readings by J. P. Welsh and R. D. Ketchum of NORDA's Polar Oceanography Branch and by Bruce Heydlauff of Naval Weapons Center, China Lake, improved the manuscript. The project is funded by NORDA program element 61153N, Herbert Eppert, Director, Ocean Science Directorate.

# Contents

---

Illustrations and tables	iv
Introduction	1
KRMS description	1
Radiometer calibration	2
Theory of calibration method used	2
Calibration of KRMS data	5
Effect of incidence angle on brightness temperature	6
Numerical approach to image classification	11
Field data	13
Histograms	14
Training regions	14
Open water	14
Old ice	15
First-year and young ice	15
Other ice types	26
Summary statistics	26
Piecewise linear interpolation	27
Interpretation of KRMS images	27
Example 1	27
Example 2	29
Example 3	29
Classification error	36
Discussion	36
Textural analysis	38
Shape analysis	38
Image enhancement	38
Differencing	39
Two-dimensional Fourier transform	39
Level slicing	39
Conclusions	39
References	45
Appendix: Symbols	47

# Illustrations and tables

---

## Illustrations

Figure 1. Passive $K_a$ -band microwave imagery of sea ice	3
Figure 2. Generalized schematic of KRMS circuit	4
Figure 3. Schematic of KRMS circuit for the cold source (sky temperature, $T_{\text{sky}}$ ) used to calibrate the instrument	4
Figure 4. Schematic of KRMS circuit for the hot source (heated load, $T_H$ ) used to calibrate the instrument	5
Figure 5. Range of digitized voltages shown with respect to the range of voltages measured ( $dV_m$ )	6
Figure 6. Scan geometry of the KRMS antennas	6
Figure 7. KRMS image of shore-fast first-year ice near Barrow, Alaska	7
Figure 8. Brightness temperature of fresh water ice as a function of incidence angle for a simple dielectric model	8
Figure 9. Brightness temperature at 37 GHz as a function of incidence angle from Kong <i>et al.</i> (1979)	9
Figure 10. Brightness temperature as a function of incidence angle from Fung and Chen (1981)	9
Figure 11. Vertically polarized brightness temperature as a function of incidence angle from Stogryn's (1981) dielectric model	10
Figure 12. Brightness temperature as a function of incidence angle for KRMS images of shore-fast first-year ice and open water	10
Figure 13. KRMS image of open water	11
Figure 14. Radiometric brightness temperature as a function of frequency between 14 and 90 GHz for four ice types	11
Figure 15. Aerial photo mosaic of the March 1983 NORDA ice camp	12
Figure 16. Mosaic of KRMS images of the camp floe	13
Figure 17. Location map of the Beaufort Sea	15

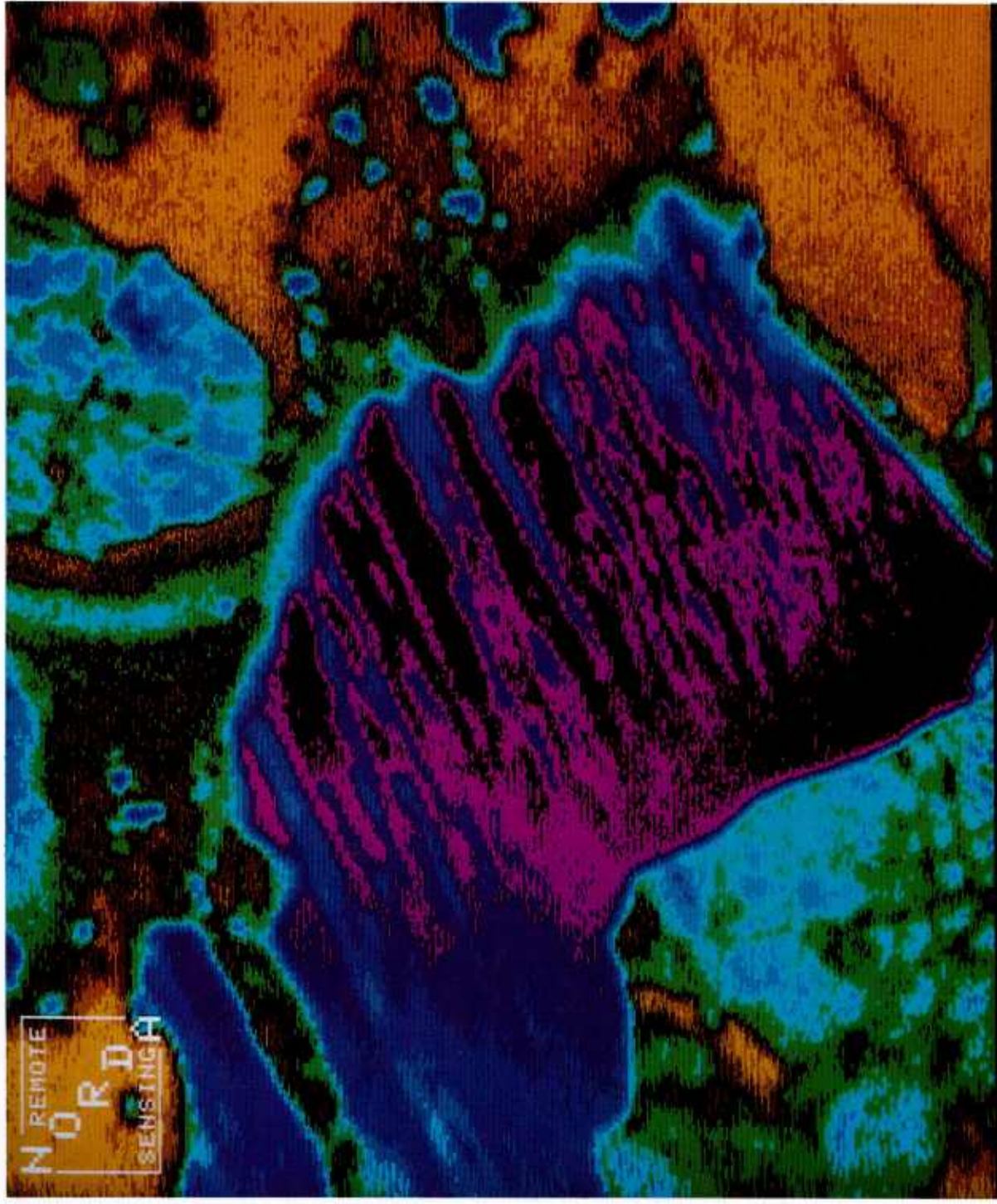
Figure 18. Frequency distribution of brightness temperatures in a KRMS scene	15
Figure 19. Example of training regions selected to characterize open water	16
Figure 20. Example of training regions selected to characterize second-year ice	18
Figure 21. Example of training regions selected to characterize multi-year ice	20
Figure 22. Example of training regions selected to characterize young ice	22
Figure 23. Example of training regions selected to characterize first-year ice	24
Figure 24. Summary statistics for training class data	26
Figure 25. Color scheme used to classify KRMS images based on measured brightness temperature	28
Figure 26. Color-classified KRMS image of second-year and first-year ice	30
Figure 27. Color-classified KRMS image of second-year and first-year ice	32
Figure 28. Color-classified KRMS image of multi-year ice, first-year ice, young ice, and open water	34
Figure 29. Minimum, mean, and maximum values for training areas	37
Figure 30. Differenced image of multi-year ice	40
Figure 31. Differenced image of second-year ice	42

## Tables

Table 1. KRMS technical characteristics	1
Table 2. KRMS system constants for losses and temperatures	5
Table 3. Training class statistics	26



NORAD  
REMOTE  
SENSING



NORDA POLAR OCEANOGRAPHY  
135K

K-BAND RADIOMETRIC MAPPING SYSTEM  
248K



# Digital processing of passive K<sub>a</sub>-band microwave images for sea ice classification

## Introduction

During March 1983 extensive, high-quality passive K<sub>a</sub>-band imagery and coincident high-resolution photography were obtained of ice in the Beaufort Sea offshore from Barrow, Alaska. Shortly before the data set was acquired, personnel at Naval Weapons Center in China Lake, California, completed development of hardware and software required to convert microwave imagery obtained with the K<sub>a</sub>-band Radiometric Mapping System (KRMS) from analog to digital form. The March 1983 data set, thus, is the first sequence of KRMS imagery to lend itself to digital processing techniques of calibration, rectification, enhancement, and classification. Numeric methods of image analysis now can be applied to KRMS data.

Work described in this report represents an initial approach to digital processing of KRMS imagery. We have four objectives:

First, we develop and implement algorithms for converting raw KRMS data to rectified and calibrated digital images. To do this we remove geometric distortion arising from aircraft motion and system scan geometry, normalize measured brightness temperatures to nadir values, and then calibrate the imagery so that brightness temperatures displayed represent true radiometric measures of surfaces imaged.

Second, we formulate a statistical basis for characterizing specific ice types imaged during the March 1983 mission. To accomplish this we select training regions that encompass areas in which specific surface types are best displayed. Then we use the means, standard deviations, and ranges of pixel values characteristic of each ice category to assess potential classification techniques based solely on single-band brightness temperature.

Third, we establish a preliminary sea ice classification algorithm for winter KRMS data based on brightness temperature. To do this we use statistics generated as part of objective two to formulate a semi-automated classification scheme in which images are color-coded to delineate major ice types (new, nilas, young, first-year, old) and open water.

Fourth, we assess the accuracy and utility of the ice classification algorithm as it applies to in-house imagery by classifying and color coding KRMS images acquired during March 1983. We can estimate error by noting misclassification of surface types using aerial photography as ground truth.

## KRMS description

The KRMS is an airborne microwave imager that operates at a center frequency of 33.6 GHz. The instrument is pod mounted and, in its present configuration, is hung from the bomb bay of an RP-3A aircraft. Important characteristics of the instrument are given in Table 1.

Three parabolic antennas mounted 120° apart on a single shaft rotate about a horizontal axis parallel to the direction of flight and provide between 7 and 25 scans of the ground per second. Use of three antennas permits continuous ground coverage to be obtained at flying altitudes of 1000 ft and above. Although each antenna scans 120° centered at nadir, only 100° of the available 120° cross-track scan is used. Resultant cross-track coverage is equal to 2.38 times altitude, or approximately 2 nmi at 5000 ft. Antenna beamwidth is 1° so that spatial resolution of the unprocessed signal is 16 ft per 1000 ft of flight altitude.

Table 1. KRMS technical characteristics

<b>ANTENNAS</b>	
number	3
diameter	24 inches
polarization	vertical
beam width	1.0°
isolation	40 dB (minimum)
<b>SCANNER</b>	
maximum scan rate	25 scans/second (40 ms/scan)
minimum scan rate	7.5 scans/second (133 ms/scan)
scan angle	60° from nadir
midscan incidence angle	0° (nadir)
scan width	3.46 x altitude
antenna position accuracy	2.5 minutes of arc
<b>STABILIZATION</b>	
method	cross-track roll gyro
accuracy	less than 0.25°
<b>RF AMPLIFIER</b>	
type	Superheterodyne (DSB)
noise	less than 5.0 dB
bandwidth	1.3 GHz
gain	greater than 60 dB
loss	1.2 dB (maximum)
<b>RADIOMETER</b>	
type	pulse stabilized, total power
pulse width	4.0 MS
local oscillator frequency	33.6 GHZ
IF bandwidth	greater than 500 MHz
video bandwidth	1.7 kHz (maximum)
video gain	72 dB (nominal)
minimum detectable signal	0.05 K/second
sensitivity	50 mV/K (nominal)
dynamic range	370 K



Resolution of 12 ft per 1000 ft of altitude is achieved using conventional signal processing techniques. Radiometric sensitivity measured in the laboratory is 0.05 K/sec. Operational sensitivity is 0.5 K or better.

The speed of the rotating antenna assembly is controlled by a servo loop consisting of a tachometer, servo board, and servo amplifier. Rotation speed is set by the operator during flight and is dependent on aircraft altitude and airspeed. Sweep position is adjusted electronically using an optical position encoder and a gyro in the pod. The beginning of each scan thus is adjusted automatically so that the antenna observing the ground is pointed toward aircraft nadir at midscan. Only the downward facing antenna is sampled at any given time. Switching between antennas is accomplished using a ferrite switch network.

Microwave radiation emanating from the surface is directed to the RF (radio frequency) electronics where it is mixed down to IF (intermediate frequency), amplified, and then detected. The detected signal is converted to an RF signal and split into two channels. One channel is recorded on analog tape for subsequent processing in the laboratory. The other channel is fed to the on-board display processor, converted to digital form, and displayed in real time as a video image having 16 grey levels. Simultaneously, a VHS format video tape is made of all imagery that is acquired. Hard-copy paper prints are produced directly from the video signal and can be dropped to ground parties minutes after they are acquired. A limited number of image processing functions can be stored in the onboard display processor, allowing standard enhancement techniques to be applied to the real-time image.

Upon completion of a mission, the analog tape is returned to the laboratory for processing. Geometric and radiometric aberrations are corrected. Cross-track distortion at image edges that arises from beam spreading is corrected by applying a simple tangent function to compensate for increased incidence angle. (This correction is also applied to the image processed in real time onboard the aircraft.) Variation in the signal that arises from differences in the response characteristics of each of the three antennas is removed. Finally, the signal is digitized and calibrated brightness temperatures are calculated according to procedures described in subsequent sections. Once calibration is complete, KRMS imagery is stored in digital form on magnetic tape or disk.

The result of this procedure is a digital representation of the surface overflow. Images are composed of pixels, each of which is assigned an integral value between 0 and 4095. Each value corresponds to a narrow range of brightness temperatures and is represented by a specific shade of grey. In this system pixels that represent warm temperatures are depicted in dark greys. Pixels that represent cool temperatures are depicted in light greys (Fig. 1). Radiometric characteristics of the surface thus are described by a spectrum of 4096 tones.

## Radiometer calibration

The final KRMS image of a scene is a digital map of brightness temperatures displayed by the imaged surface. The problem of calibration is to define the relationship between the analog voltage produced by the radiometer ( $V_m$ ) and the brightness temperature of the imaged surface ( $T_B$ ) so that a faithful representation of the microwave characteristics of the surface is produced.

## Theory of calibration method used

Relevant features of the KRMS radiometer circuit are shown in schematic form in Figure 2. Antenna temperature ( $T_s$ ) is a function of characteristics of this circuit. The relationship between recorded voltage ( $V_m$ ) and antenna temperature can be expressed as:

$$T_s = L_R L_F L_J \frac{K V_m}{G} - L_R (T_R T_F) - L_R L_F (T_F T_J) - \frac{L_R L_F L_J}{L'_J} (T_J T_L) + T_R \quad (1)$$

where  $T_R$ ,  $T_F$ ,  $T_J$ , and  $T_L$  are radiometric temperatures of the radome, feed path, ferrite switches, and reference load respectively;  $L_R$ ,  $L_F$ ,  $L_J$ , and  $L'_J$  are fixed insertion losses associated with the radome, feed path, source-path ferrite switch, and reference load-path ferrite switch respectively; and  $G$  is the total gain. The value of  $G$  is determined both by procedures used to record  $V_m$  on analog tape in the field, and by subsequent procedures used to read and process  $V_m$  in the laboratory. This process is discussed in the next section.  $K$  is a constant that relates brightness temperature in degrees Kelvin sensed by the KRMS antenna to volts produced by the KRMS circuitry.

The value of  $K$  is derived from the ratio between the known brightness temperature and the circuit output voltage measured from two sources, one cold ( $K_1$ ) and the other hot ( $K_2$ ). The cold source is the sky ( $T_{sky}$ ), with a radiometric temperature of 20.0 K. The hot source is a heated load ( $T_H$ ) with a measured temperature of 336.5 K. Schematic diagrams of circuits used for these measurements are given in Figures 3 and 4. Values of  $K$  are computed for the sky source using:

$$T_1 = \frac{1}{L_J} \left( \frac{T_{sky} T_A}{L_A} + T_A T_J \right) \quad (2)$$

and for the heated load using:

$$T_2 = \frac{T_H T_J}{L_j} \quad (3)$$

where  $T_A$  and  $L_A$  are the temperature and fixed loss respectively of a precision attenuator placed in the circuit, and  $T_J$  and  $L_J$  are the temperature and loss associated with the ferrite switches. Values for each variable in both equations are known.  $K_1$  and  $K_2$  then can be computed from:

$$K_n = \frac{T_n}{V_n} \quad (4)$$

However, small values of  $V_n$  produce large errors in  $K_n$  due to noise on  $V_n$ . Therefore, a weighted mean of the two

measurements (sky and heated load) is computed:

$$K = \frac{\frac{K_1}{V_2} + \frac{K_2}{V_1}}{\frac{1}{V_1} + \frac{1}{V_2}} \quad (5)$$

Substituting this value of  $K$  into Eq. (1) gives a calibrated value for antenna temperature  $T_s$  in Kelvins.

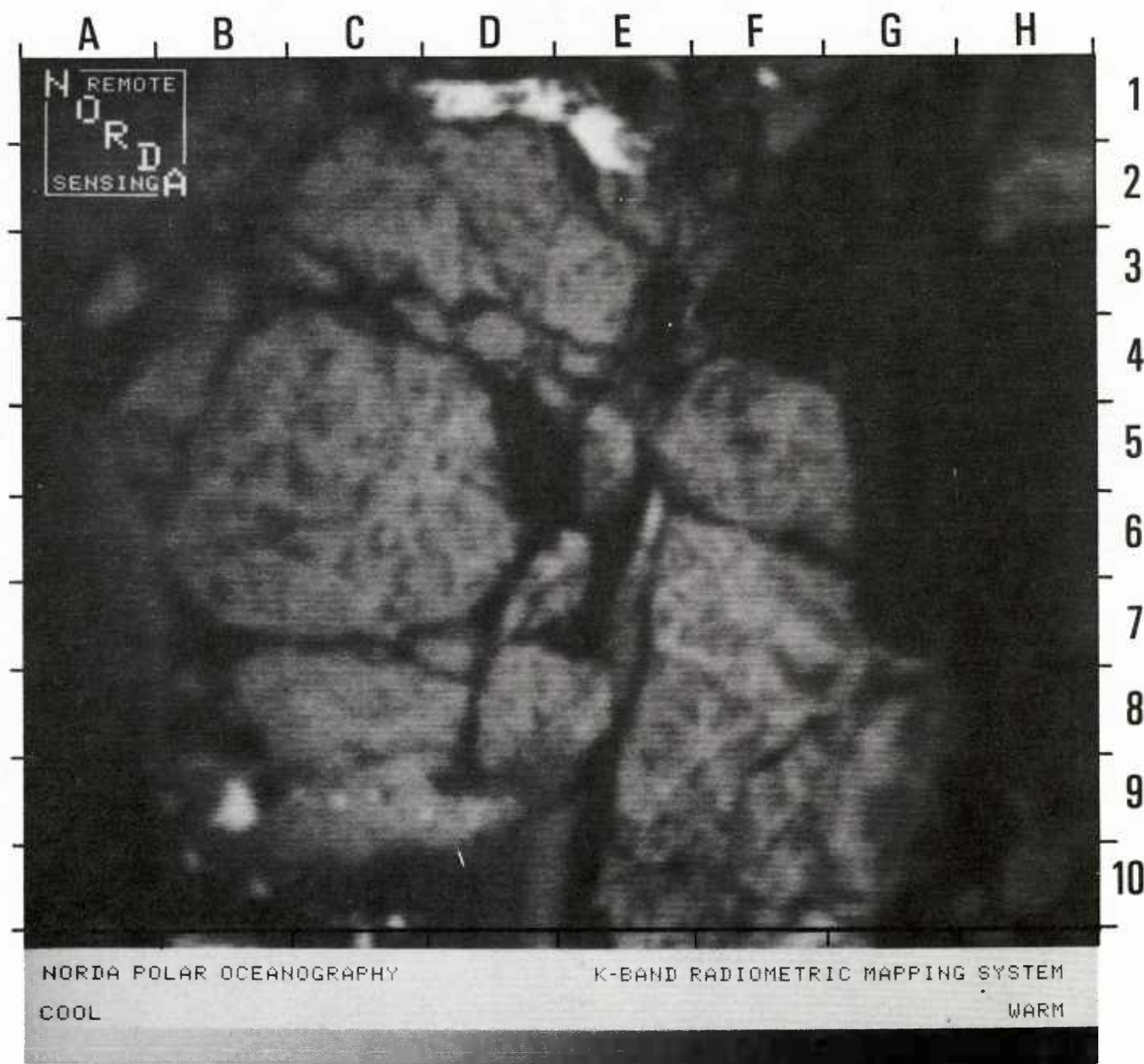


Figure 1. Passive  $K_a$ -band microwave imagery of sea ice. Radiometrically cool surfaces (open water, new (frazil), old ice) are depicted by light tones. Radiometrically warm surfaces (young/first-year ice) are depicted by dark tones. Multi-year floes predominate in the central portion of the scene. A small body of open water is present at top center (light tone). First-year ice is present along the right side of the image (dark tone). New and nilas ice are present at bottom center and along the left margin of the scene. Area imaged is 3600 m (11,900 ft) cross-track (side to side) and 3200 m (10,500 ft) down-track (top to bottom).

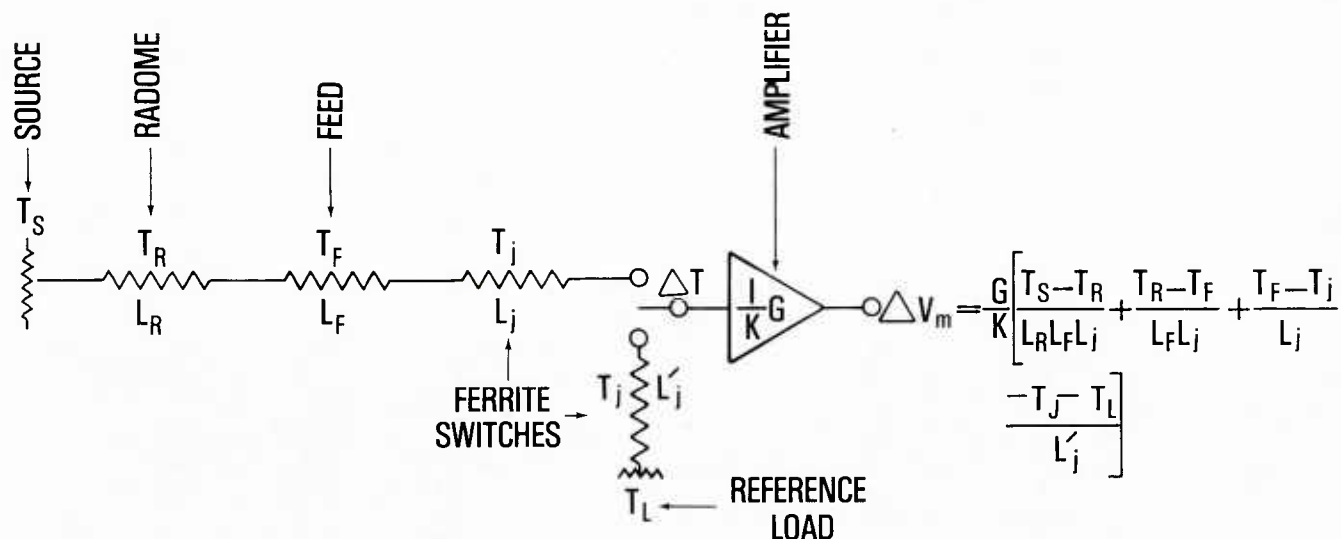


Figure 2. Generalized schematic of KRMS circuit. Measured voltage ( $V_m$ ) is a function of temperatures and losses of components within the circuit.

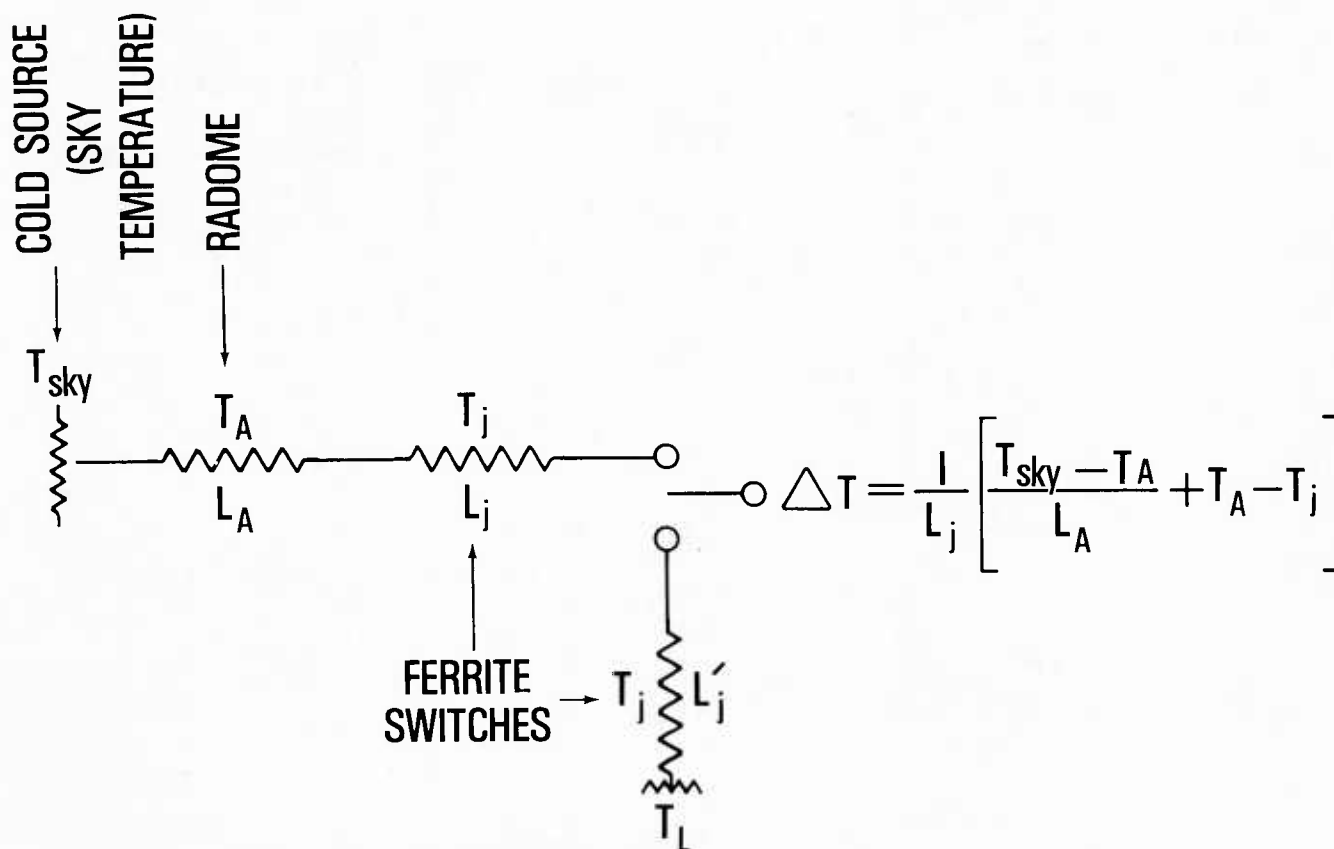


Figure 3. Schematic of KRMS circuit for the cold source (sky temperature,  $T_{sky}$ ) used to calibrate the instrument.

Critical variables in determining  $T_s$  from Eq. (1) are  $G$  and  $K$ .  $G$  typically is a known quantity, the value of which is determined either by fixed characteristics of the system, or by manual settings that produce known values. But  $K$  is extremely difficult to measure. Accurate values for  $K$ , when used in Eq. (1), will produce brightness temperatures that are calibrated accurately. In some cases, better results are achieved when ground truth data are used to determine the value of  $K$ . If  $T_s$  is known for a given  $dV_m$  from field data, then  $K$  can be expressed in terms of  $T_s$  and  $V_m$ . From Eq. (1):

$$K = \frac{G}{V_m L_R L_F L_J} T_s + L_R (T_R T_F) + L_R L_F (T_F T_J) + \frac{L_R L_F L_J}{L'_J} (T_J T_L) - T_R. \quad (6)$$

With  $K$  established,  $T_s$  is calculated for other values of  $V_m$  using Eq. (1).

### Calibration of KRMS data

Using values given in Table 2 for temperatures and fixed losses in the KRMS system, Eq. (1) reduces to:

$$T_s = 292 + 1.35 \frac{KV_m}{G}. \quad (7)$$

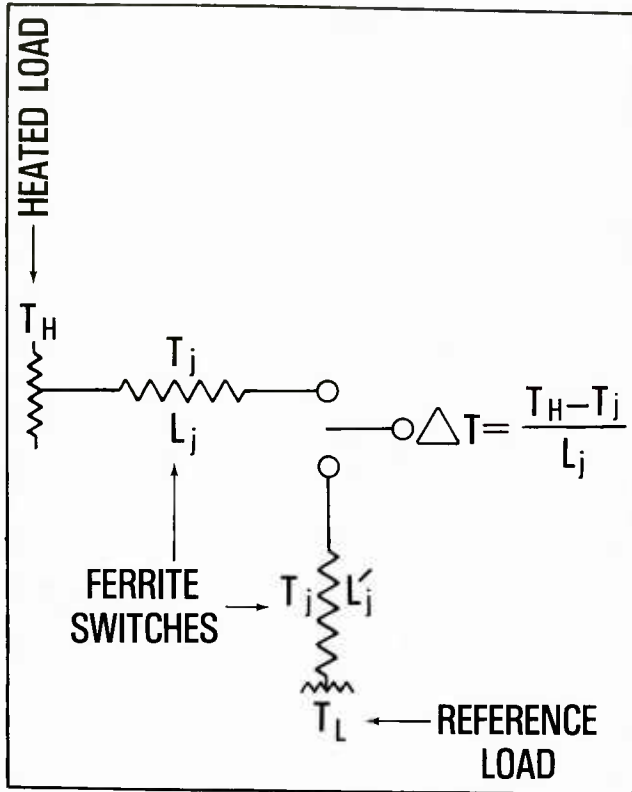


Figure 4. Schematic of KRMS circuit for the hot source (heated load,  $T_H$ ) used to calibrate the instrument.

Table 2. KRMS system constants for losses and temperatures

PARAMETER	VALUE
$L_F$	1.10
$L_J$	1.18
$L'_J$	1.11
$L_R$	1.04
$T_F$	263 Kelvins
$T_J$	288 Kelvins
$T_L$	288 Kelvins
$T_R$	253 Kelvins

The radiometer voltage ( $V$ ) first is attenuated to recorder levels by  $A_R$ . The value of  $A_R$  is fixed over the course of each mission. The input-output gain  $G_R$  used to record the signal is predetermined. Finally, upon reading the recorded voltage, processing circuits amplify the signal by a gain of  $G'$ .  $G$  in Eq. (6) thus is replaced by:

$$G = \frac{G_R G'}{A_R}. \quad (8)$$

Conversion of the analog signal to digital format is done at a 12-bit level of precision. That is, the range of analog voltages that encompass all surface types encountered in a given mission is represented in digital form by a spectrum that consists of 4096 discrete values (grey levels). The range of antenna temperatures that the KRMS can measure is greater than the range of brightness temperatures typical of surfaces in polar regions. Of course, only the range of brightness temperatures that are characteristic of snow, ice, and open water need be captured fully. This smaller  $T_B$  range can be expanded to fill to 4096 grey levels. The voltage ( $V_1$ ) that corresponds to the minimum digitizing level ( $N=0$ ) is determined (Fig. 5). The maximum digitizing level is taken from the voltage that corresponds to sky temperature.  $V_m$  then can be rewritten in terms of  $V_1$  and  $N$ , the digital level value:

$$V_m = V_1 - NV_D \quad (9)$$

where  $V_D$  is the number of volts per digital level (Fig. 5) and here is equal to 0.00488.

Now, substituting Eqs. (8) and (9) into Eq. (7):

$$T_s = 292 + 1.35 \frac{K(V_1 - 4.88 \times 10^{-3} N) A_R}{G_R G'} \quad (10)$$

Ground truth data were used to solve Eq. (7) for  $K$ ,  $A_R$ ,  $G_R$ , and  $G'$ . Let:

$$K = \frac{K A_R}{G_R G'}. \quad (11)$$



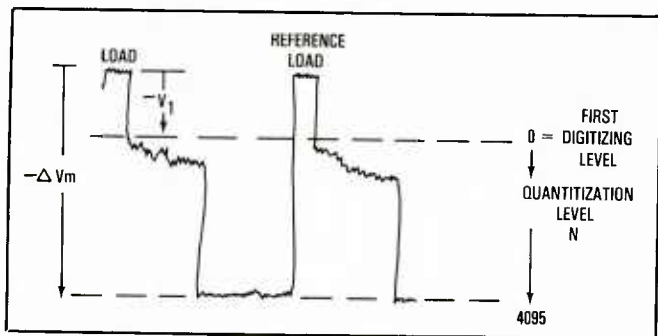


Figure 5. Range of digitized voltages shown with respect to the range of voltages measured ( $dV_m$ ).

Then, from Eq. (10):

$$T_s = 292 - (37.5)(K').$$

The radiometric brightness temperature ( $T_s$ ) of sea water was determined to be 135 K with NORDA's portable 33.6-GHz radiometer. Gain and attenuator settings were constant for the mission. Thus:

$$K' = \frac{292-135}{37.5} = 4.19.$$

Substituting 4.19 for  $K'$  in Eq. (7), a calibrated antenna temperature

$$T_s = 248 - 2.76 \times 10^{-2} N$$

is obtained from the digital data where  $N$  is the digitized level between 0 and 4095.

## Effect of incidence angle on brightness temperature

The microwave brightness temperature of a substance is a function not only of its physical characteristics, but also of the angle from which the material is viewed and the polarization of the received RF energy. The KRMS antennas rotate clockwise about a horizontal axis (viewed from the rear of the plane) and scan perpendicular to the aircraft ground track from  $50^\circ$  right of nadir to  $50^\circ$  left of nadir. Although the polarization at nadir is undefined, orientation of waveguides fed by the antennas makes off-nadir polarization vertical (Fig. 6).

Because of the vertical polarization off-nadir, brightness temperatures appear higher near image edges for each type of surface imaged as a result of differences in incidence angle. This effect, though observed in all unnormalized KRMS images, is most visible in scenes in which a single surface type

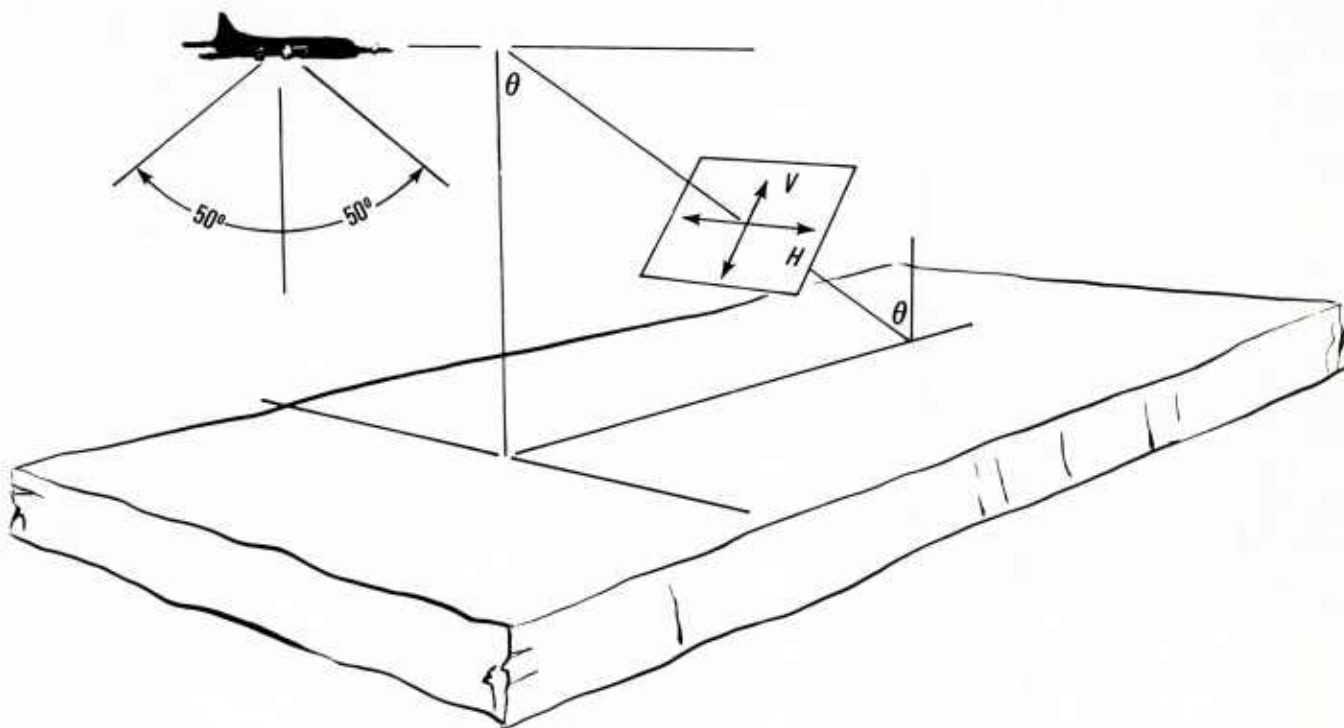


Figure 6. Scan geometry of the KRMS antennas. Measured radiation is vertically polarized at all off-nadir angles. At nadir, measured radiation is nonpolarized.

predominates. Figure 7 shows extensive, shore-fast first-year ice near Barrow, Alaska. Ice imaged near nadir is lighter in tone (colder) than ice imaged at scene edges as a result of the incidence angle effect. As this example shows, the brightness temperature of a given surface cannot be characterized by a single value. Rather, it is described by a functional relationship including the physical properties of the surface and the incidence angle from which it is imaged.\*

\*Notation used here to signify brightness temperature thus is written at  $T_p(\theta)$ , where  $p$  is the polarization of the detecting antenna and  $\theta$  is the angle between a normal drawn to the imaged surface and the axis of the antenna (the direction of the center of its main lobe) (Fig. 6).

If brightness or antenna temperature can be determined as a function of incidence angle for the range of temperatures represented in KRMS images, then off-nadir temperatures can be normalized to their nadir values. Normalization of off-nadir brightness temperatures is desirable if automated or semi-automated classification procedures are to be applied to KRMS imagery. Computerized image classification is optimized when the variance and range of values descriptive of each classification category (training class) are minimized. Effects of incidence angle increase the apparent variance by broadening the range of antenna temperature values descriptive of each surface. Overlap between classes is more likely to occur as a result. Unambiguous classification is achieved only when a given brightness temperature or set of brightness temperatures corresponds to

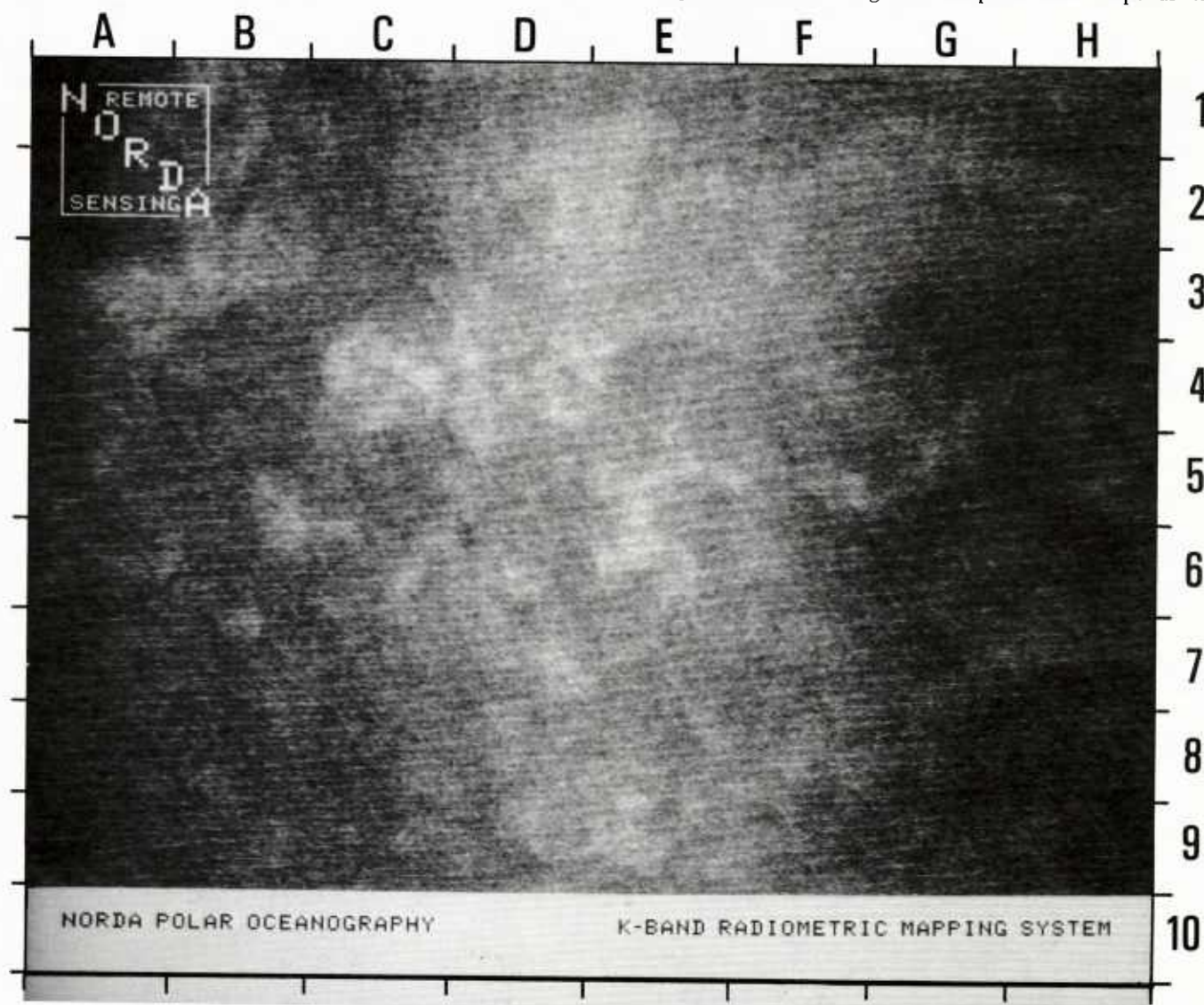


Figure 7. KRMS image of shore-fast first-year ice near Barrow, Alaska. Darkening of the scene at image limbs shows the effect of incidence angle on measured brightness temperature. Temperatures measured at nonnadir angles for a given sample of ice are warmer than temperatures measured at nadir for the same ice sample.



a specific surface type uniquely. Normalization of off-nadir brightness temperatures to their nadir values will minimize the spread of temperatures that define a given class.

The effect of incidence angle can be modeled by treating the emitting substance as a semi-infinite dielectric slab and calculating the Fresnel reflection coefficients. The Fresnel coefficients give the fraction of the electric field strength that is reflected back into the dielectric. The angular dependence of  $T_p(\theta)$  and its partition into polarizations is due to the Fresnel coefficients that are a property of the surface.

For completeness we will take the dielectric to be lossy, resulting in a complex dielectric constant:

$$\epsilon = \epsilon' + i\epsilon'' \quad (12)$$

The Fresnel coefficients for an electromagnetic wave emerging from the dielectric are:

$$R_h(\theta) = \frac{\cos\theta - S}{\cos\theta + S} \quad (13a)$$

$$R_v(\theta) = \frac{\epsilon\cos\theta - S}{\epsilon\cos\theta + S} \quad (13b)$$

where

$$S = \sqrt{\epsilon - \sin^2\theta}$$

and h and v indicate horizontal and vertical polarizations respectively.

In the microwave portion of the spectrum, the intensity of radiation emitted by a "grey" body is frequency-dependent and is proportional to physical temperature  $T_O$ . Since the intensity is proportional to the square of the field strength, we have outside the dielectric (Stogryn, 1970):

$$T_p(\theta) = |R_p|^2 T_{sky} + (1 - |R_p|^2) T_O \quad (14)$$

$T_{sky}$  is the radiometric temperature of the sky, which in the microwave portion of the spectrum is typically less than 30 K.  $T_{sky}$  is not polarized. (Since the energy measured by  $T_O$  arises from random molecular transitions in the material, it is randomly polarized and propagates uniformly in all directions in the material.)

One popular notation used in describing the brightness temperature of a surface is the emissivity,  $e$ , defined by:

$$T_p = e_p T_O \quad (15)$$

so that in the simplest case described above (ignoring contribution from the sky) we have:

$$T_p = (1 - |R_p|^2) T_O$$

and

$$e_p = 1 - |R_p|^2$$

However, the emissivity of a substance that emits from its bulk (*i.e.*, well below its surface) and that contains a nonlinear vertical physical temperature profile is not described accurately by Eq. (15). Since snow and ice may both behave in this way, Eq. (15) should not be applied here, and we will use  $T_p(\theta)$  for the rest of this discussion.

Eq. (14) is plotted in Figure 8 for values of  $\epsilon'$  and  $\epsilon''$  which are those given by Stogryn (1981) for fresh-water ice. These curves show the essential features of  $T_p(\theta)$  for most physical situations. Addition of surface roughness, vertical temperature profile, scattering centers, finite thickness, and vertical physical structure to the dielectric complicate the mathematics considerably, but do not change the essential behavior of the curves. We give two examples from the literature to demonstrate this point.

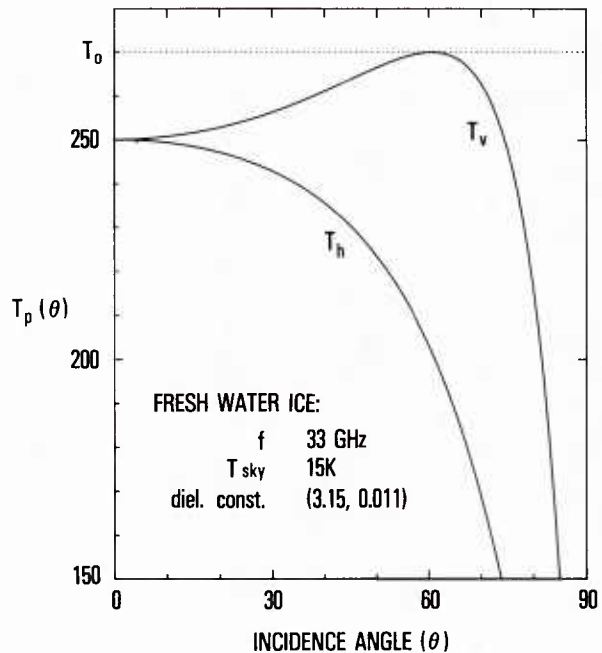


Figure 8. Brightness temperature of fresh water ice as a function of incidence angle for a simple dielectric model (Eq. (14), this report). Ice is treated as a semi-infinite dielectric slab with constants appropriate for 33-GHz radiation. Values of  $\epsilon'$  and  $\epsilon''$  are from Stogryn (1981).

Figure 9 is taken from Kong *et al.* (1979) who modeled snow as a lossy dielectric layer containing spherical scatterers. The snow is modeled as a 66-cm layer over ground. Black dots are field data to which theory is being compared. Note that although  $T_v(\theta)$  of the model does not exhibit a maximum value (as do the simple theoretical curves of Fig. 8), the data show a maximum. Both theory and experiment in this case, though, still do not deviate far from the simple Fresnel coefficient model. Figure 10 shows a group of curves derived from a model discussed by Fung and Chen (1981) who consider the effect of a rough boundary layer on  $T_p(\theta)$ . Their snow layer is a nonlossy dielectric characterized by a rough top layer. In the case shown, the effect of scattering is stronger than the effect of absorption in the snow.

In cases where thermal surface temperatures of Arctic Sea ice have been shown to be uniform to within a few Kelvins (Gloersen *et al.*, 1973), large brightness temperature variations arise almost entirely from changes in the physical properties of the surface (e.g., salinity, liquid water content). (Surface temperatures measured with a Barnes PRT-5 radiometer show that this is

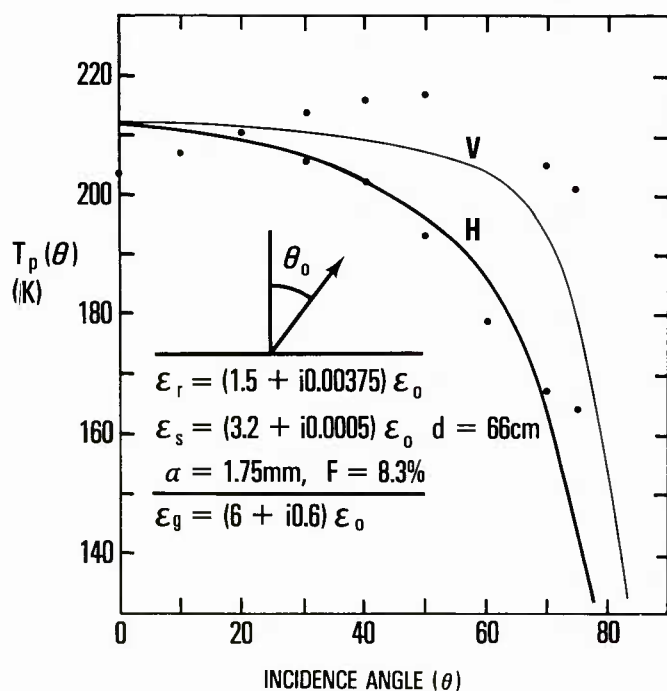


Figure 9. Brightness temperature at 37 GHz as a function of incidence angle, from Kong, *et al.* (1979).  $\epsilon_r$  is the dielectric constant of the dielectric layer,  $\epsilon_s$  is the dielectric constant of assumed spherical scatterers, and  $\epsilon_g$  is the dielectric constant of ground under snow.  $d$  is the thickness of the dielectric layer. Parameters  $a$  (effective radius of a scatterer) and  $F$  (effective fractional volume of a scatterer) are fitted empirically.

the case for KRMS data used in this report.) For a surface having uniform physical temperature and varying physical properties, we expect a family of curves such as those in Figure 11. When nadir brightness temperature ( $T_v(\theta=0)$ ) is low (open water), in general, the surface emits less radiation and its reflection coefficients are somewhat high (Eq. 13b). Under these conditions, brightness temperature ( $T_v(\theta)$ ) rises rapidly as  $\theta$  increases. When  $T_v(\theta=0)$  is high (first-year ice), the opposite is true. Reflection coefficients are low and the curve rises more slowly with increasing  $\theta$ .

KRMS data collected over first-year ice and open water show this relationship and are presented in Figure 12. Open water data were taken from an image in which open water is the predominant surface type (Fig. 13). The coldest brightness temperature measured in each column of the image is plotted as a function of the incidence angle for that column (Fig. 12). (A column represents a line parallel to the flight direction and corresponds to a constant incidence angle.) Use of the coldest

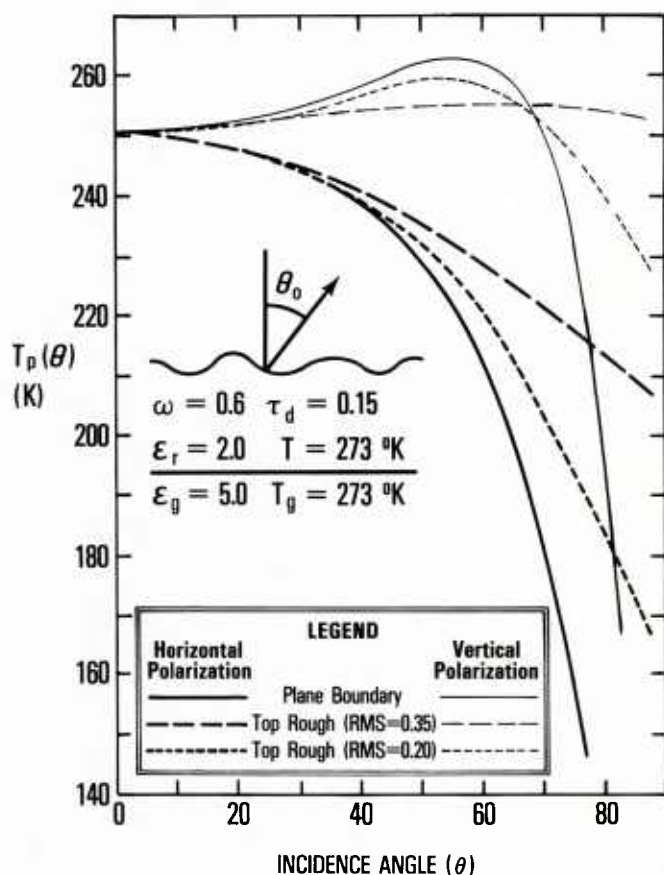


Figure 10. Brightness temperature as a function of incidence angle, from Fung and Chen (1981).  $\epsilon_r$  is the dielectric constant of the dielectric layer, in this case snow, and  $\epsilon_g$  is the dielectric constant of underlying ground.  $\omega$  (albedo of snow) and  $\tau_d$  (optical depth of snow) are related to absorption and volume scattering coefficients, respectively.

temperature reduces or eliminates the confounding effect of radiometrically warmer slush and frazil that also are present in the scene.

First-year ice data (Fig. 12) were taken from imagery of shorefast ice near Barrow, Alaska (Fig. 7). Two curves are presented (Fig. 12). First, the warmest temperature observed in each column of the digital first-year scene is plotted as a function of incidence angle. Although scatter of these data is somewhat high, a general trend that is less steep than that observed for open water is defined. The second first-year curve (Fig. 12) represents the mean temperature of all 512 pixels in each column of the same first-year image (Fig. 7). Scatter displayed by these averaged data is less than that of the maximum data. The relationship defined by the mean curve parallels that suggested by the maximum data curve.

Because nadir brightness temperatures measured for most surfaces fall between nadir temperatures of open water and first-year ice (Figs. 14 and 11), normalization curves for other surfaces probably fall between the curves for open water and first-year ice shown in Figure 12. It is not clear from available data, however, whether we can expect such a family of curves to be free of crossings. If no curves cross, then for a given incidence angle each temperature measured corresponds uniquely

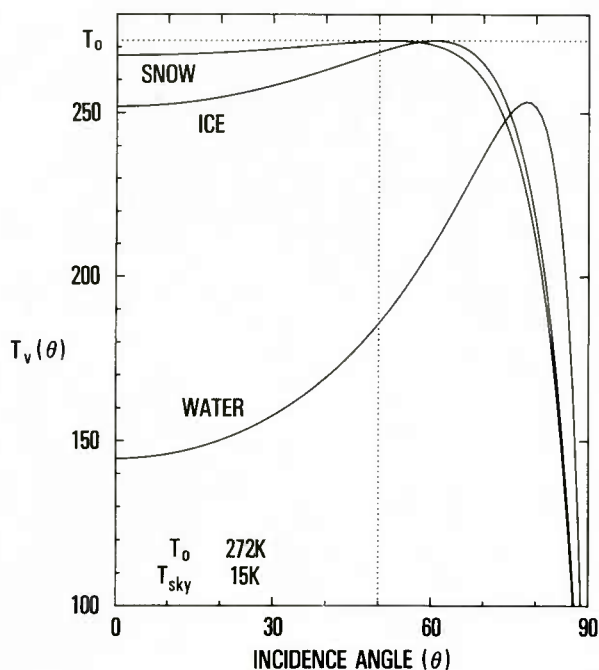


Figure 11. Vertically polarized brightness temperature as a function of incidence angle from a dielectric model by Stogryn (1981) for three dielectrics: dry snow (1.7, 0.01), fresh water ice (3.15, 0.004), and water of salinity 34 parts per thousand (11.0, 21.0). The vertical dotted line marks the KRMS imaging limit.

to a single brightness temperature curve. If this is the case, then it is possible to construct an algorithm that will "normalize" all brightness temperatures in an image to nadir values. Winter data on which this report is based indicate that we cannot interpolate linearly between cold and warm brightness temperatures. However, nadir temperatures might be estimated, perhaps with reasonable accuracy, by interpolating between

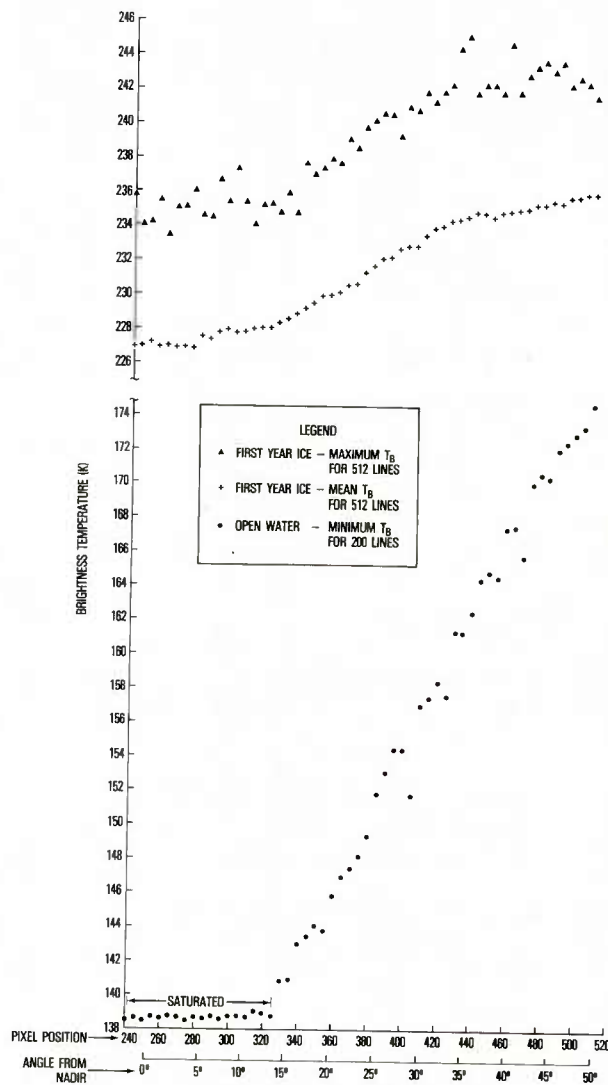


Figure 12. Brightness temperature as a function of incidence angle for KRMS images of shorefast first-year ice (Fig. 8, this report) and open water (Fig. 13, this report). Brightness temperatures recorded for off-nadir angles were determined for each ice type from the mean, maximum, or minimum temperature values present in a given column of pixels. Data are plotted at 5° intervals for the right half of each image. Nadir (0°) falls between pixels 256 and 257.

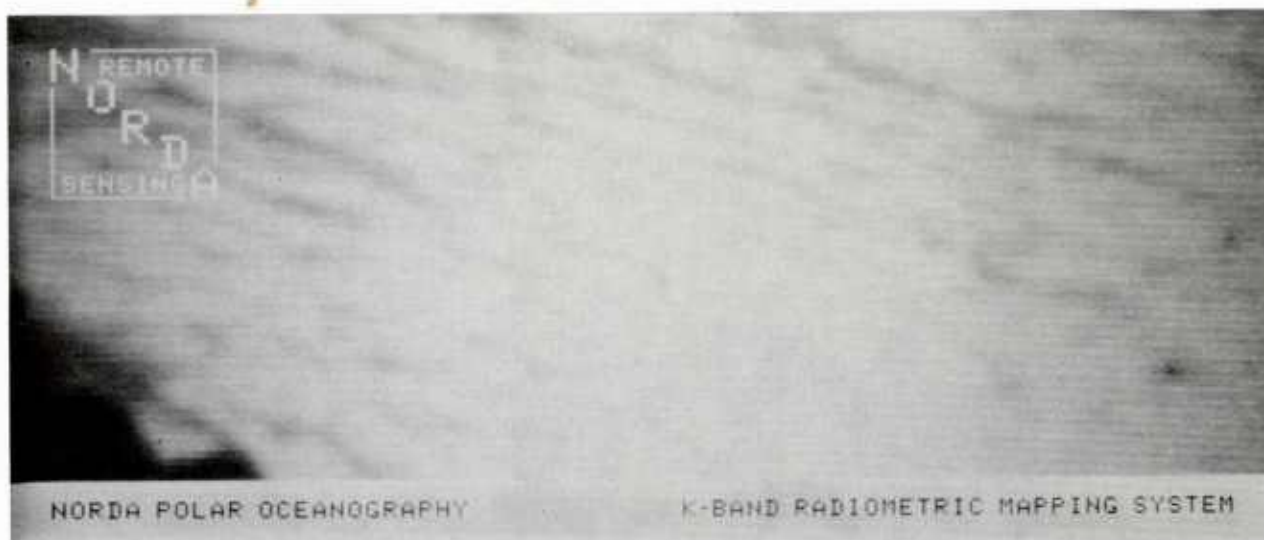


Figure 13. KRMS image of open water. Stringers and tadpoles of frazil and slush appear as radiometrically warm bands and splotches (grey) within radiometrically cold open water (white). Young/first-year ice is present in the lower left-hand corner of the image.

known normalization curves for open water, first-year ice, and other uniform surfaces that are imaged, according to some function. Additional data must be acquired over radiometrically uniform surfaces characterized by a wide range of brightness temperatures before a complete family of curves can be established and this relationship can be defined. The normalization method outlined here then can be applied effectively and images can be normalized routinely.

## Numerical approach to image classification

Typical KRMS scenes include complex assemblages of surface types. Open water, new ice, nilas, young ice, first-year ice of various thicknesses, second-year ice, and multi-year ice with included meltponds, ridges, and fractures can occur in proximity to each other (Fig. 1). A successful ice classification scheme must discriminate between these surface types.

Previous experiments (Gloersen *et al.*, 1981a; Troy *et al.*, 1981, 1982; Cavalieri *et al.*, 1983; Comiso, 1983) suggest that open water, first-year ice, and old ice can be distinguished from each other on the basis of their radiometric characteristics at  $K_a$ -band frequencies (26.5 to 40.0 GHz) (Fig. 14). Each of these surfaces, then, should be portrayed uniquely in images composed of brightness temperature measurements made within the  $K_a$ -band. Conventional, nonnumeric methods of image interpretation applied to uncalibrated KRMS imagery support this conclusion (Ketchum and Lohanick, 1977; Ketchum *et al.*, 1983).

Conventional methods of image analysis employ visual cues to discriminate between surface types. Information concerning

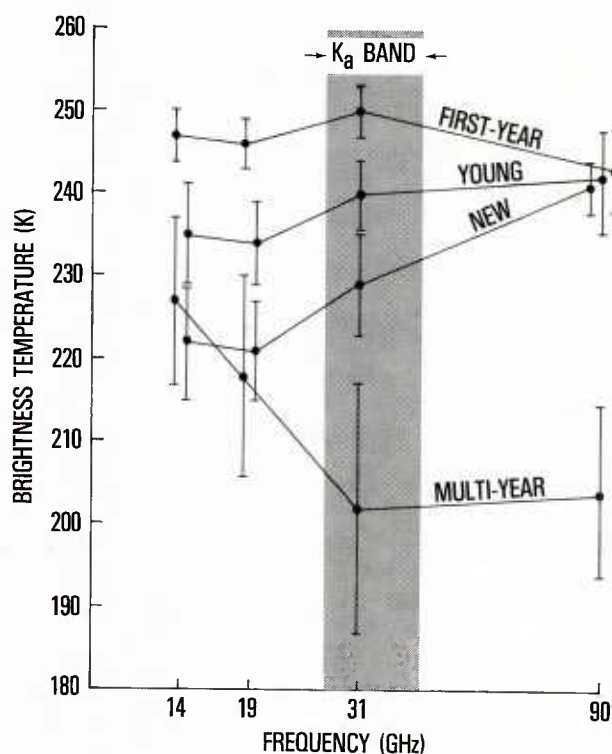


Figure 14. Radiometric brightness temperature as a function of frequency between 14 and 90 GHz for four ice types (from Troy *et al.*, 1981). Within the range of  $K_a$ -band frequencies (shaded), brightness temperatures measured for first-year ice, young ice, new ice, and multi-year ice fall within discrete ranges that do not overlap.



overall brightness temperature, the arrangement of pixels of different brightness temperature within the area of interest (texture), and the shape of outlines bounding a given area is assimilated mentally to identify ice of a particular type. A trained image analyst, for example, identifies multi-year floes by their low brightness temperature, inclusion of ridges and meltponds within the floe boundary, and their typical rounded shape. An automated ice classifier must perform these same functions to achieve comparable accuracy.

The ice classification scheme discussed here represents a first step toward automated image classification. The scheme is based only on brightness temperature and is designed to define the extent of information contained in brightness temperature alone. Neither textural characteristics of imaged surfaces nor shape attributes of regions encompassed by a given surface type are considered. Both of these parameters, texture and shape, contain information related to surface type and ultimately must be used.



*Figure 15. Aerial photo mosaic of the March 1983 NORDA ice camp. The camp is located at the center of the image on a large multi-year ice floe. First-year ice and young ice of various thicknesses surround the camp floe. Flight altitude is 3000 ft.*

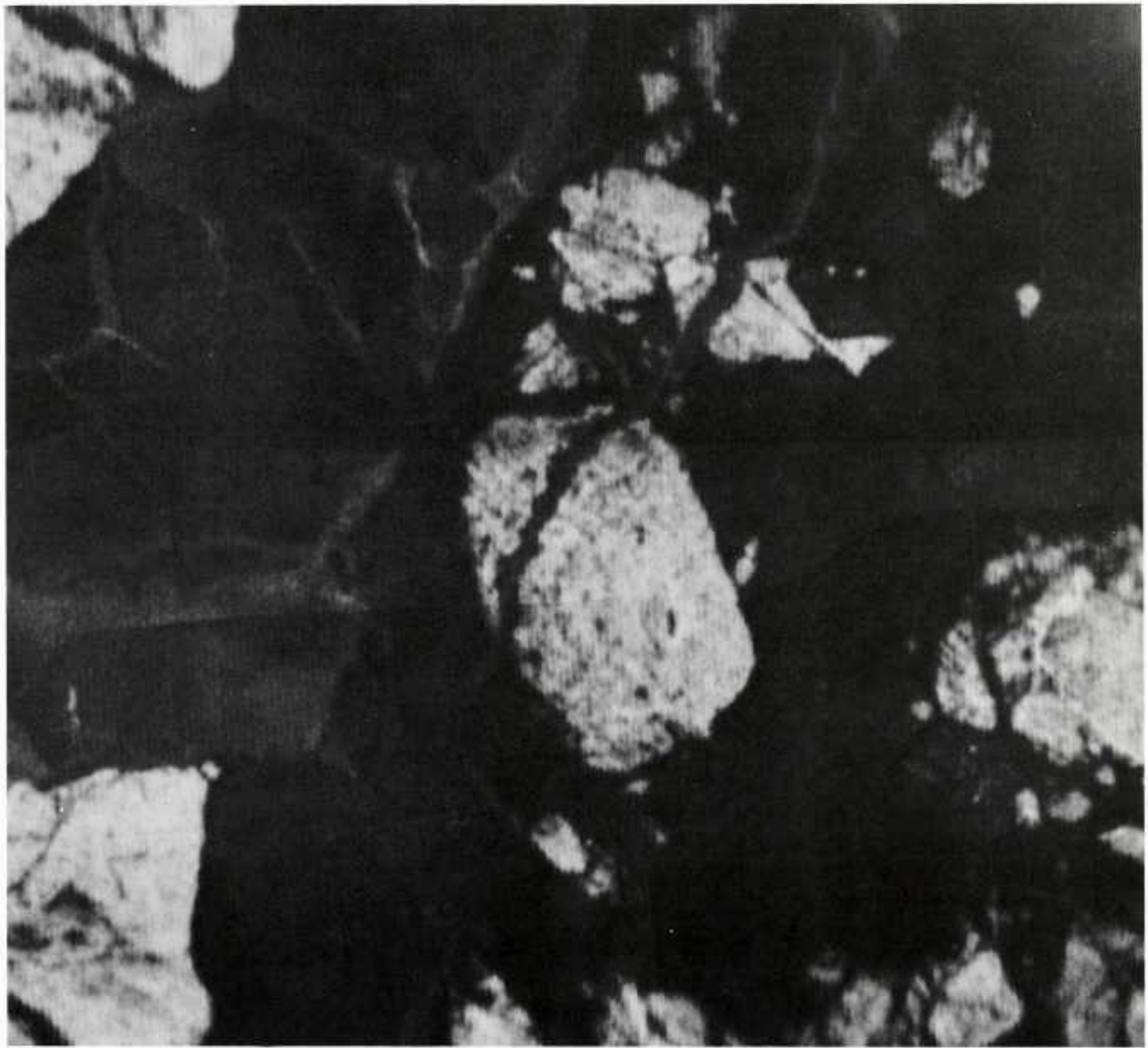


Figure 16. Mosaic of KRMS images of the camp floe. Photographs of this same scene are presented in Figure 15. The multi-year camp floe is the cold (white) object at the center of the image. Radiometrically warmer first-year ice and young ice (dark tones) surround the floe. Flight altitude is 3000 ft.

## Field data

Data utilized for this study were collected on 20 March 1983 over the Beaufort Sea north of Barrow, Alaska. High resolution aerial photography (Wild RC-10), surface temperature traces (Barnes PRT-5 radiometer), and surface roughness profiles (Spectra-Physics Laser Profiler) were obtained in conjunction with the KRMS. A field party was placed on the ice to provide in situ measurements that included surface temperature (Barnes PRT-5 radiometer), ice properties (salinity, ice thickness, and snow cover), meteorologic conditions, and surface microwave characteristics. Surface microwave measurements using NORDA's

portable 33.6-GHz radiometer to profile small sections of the KRMS ground track were planned. The experiment was planned to meet two objectives. First, to obtain detailed imagery of an area surrounding the ice camp so that ground truth data related directly to KRMS imagery could be acquired. Second, to obtain KRMS imagery of a wide variety of ice types over a long traverse at different altitudes to test the utility of the KRMS as an ice imaging system.

The camp floe was imaged successfully on 20 March 1983 at 1000-, 3000-, and 10,000-ft altitudes. Hard copy KRMS prints of the ice camp and adjacent area made at 1000- and 3000-ft



altitudes were air dropped to the surface party within 30 min of acquisition. An aerial photographic mosaic (Fig. 15) and a KRMS mosaic of the same area (Fig. 16) were prepared after the flight and dropped to the ice party 36 hr later. The ice party was to have used these data as an aid in locating and investigating anomalies observed in the airborne imagery. However, the ice camp floe began drifting rapidly out of range of shore support shortly after imagery was obtained. The original camp was abandoned as a consequence and relocated closer to shore support before extensive ground truth data could be obtained and correlated with the airborne images.

A superb suite of high-resolution photography and coincident KRMS imagery was obtained in conjunction with the second objective of the field experiment. Data were acquired from 5000 ft of altitude along a track extending from Barrow 240 miles offshore in a north-northeasterly direction (Fig. 17). This same track was flown on the return trip to Barrow at 10,000-ft altitude. KRMS imagery was obtained over the entire route. Photography was obtained over the 5000-ft leg of the mission. Results discussed below are based primarily on these 5000-ft data.

## Histograms

Frequency distributions of pixel values (antenna temperatures) that define each scene can be represented as histograms (Fig. 18). Counts in each histogram interval correspond to the number of pixels in the scene with measured brightness temperatures that fall between temperatures marking interval boundaries. Histograms so formed typically are polymodal. The area under a particular mode indicates the relative abundance of a surface type or group of surface types of similar radiometric character. Individual modes correspond to specific ice types to the extent that pixels of different value correspond to different surface types included in the image.

The type of ice that corresponds to a specific mode cannot be determined solely from the histogram with absolute certainty. For example, it is reasonable to guess that the warmest mode in Figure 18 (224 K) represents first-year ice, the warmest surface imaged in Figure 1. It is also reasonable to guess that the large, cooler mode centered at 196 K represents old ice, the most abundant surface imaged in Figure 1. However, it is unclear whether pixels that fall in the region between these two modes (205 K to 220 K) represent cool first-year ice, warm old ice, or other types of ice imaged in the scene. It is also unclear whether the cool tail of the old ice mode (155 K to 180 K) represents very cool old ice, features that occur within old ice floes (ridges, fractures, and frozen meltponds), or surfaces that are totally unrelated to old ice.

## Training regions

To define the relationship between individual modes and specific ice types, the distribution of brightness temperatures characteristic of specific surface types was defined. Coincident aerial photographs were used to identify examples of open water, new ice (frazil, grease, and slush (Weeks and Ackley, 1982) and tadpoles (Dunbar and Weeks, 1975)), nilas, young ice, first-year ice, second-year ice, and multi-year ice on KRMS images. Histograms of scenes containing chosen examples were generated. Training regions representative of each surface type were delineated using I<sup>2</sup>S System 101 Image Processor System (Stephenson, 1983). Pixel coordinates delineating each training region were selected using the I<sup>2</sup>S BLOTCH function. Then, the maximum and minimum brightness temperatures and the mean and standard deviation of all pixels within each BLOTCHed region were computed using TRAIN. Multiple regions were selected for each surface type.

Figures 19-23 are examples of training regions selected for open water, young ice, first-year ice, second-year ice, and multi-year ice. Each figure shows a raw KRMS image, a mosaic of coincident aerial photographs taken at the same time the KRMS image was acquired, and histograms of brightness temperature distributions that are representative of the scene. Training set statistics that include the mean, standard deviation, and the maximum and minimum values of the type of surface sampled from the scene are plotted on respective histograms. Dimensions of the area shown in each KRMS scene are 3600 m (11,900 ft) in the cross-track direction (side to side) and 3200 m (10,500 ft) in the down-track direction (top to bottom). Dimensions of the area shown in each photo-mosaic are 2300 m (7500 ft) cross-track and 3200 m (10,500 ft) down-track. Note that whereas the field of view presented in KRMS images is 100°, the field of view of photographic coverage is 74°.

## Open water

Examination of open water training regions (Fig. 19) reveals that floating frazil in the form of wind blown streamers and tadpole bodies (Dunbar and Weeks, 1975) are included in the blotched area from which statistics were calculated. This accounts for the relatively broad range of temperatures encompassed by the open water region. Open water that is free of ice crystals should, in theory, display a narrow range of very cold brightness temperatures that show little variance about a mean (Swift, 1980). Thus, warmer temperatures within the open water category represent stringers of frazil or other types of new ice included in the training region.

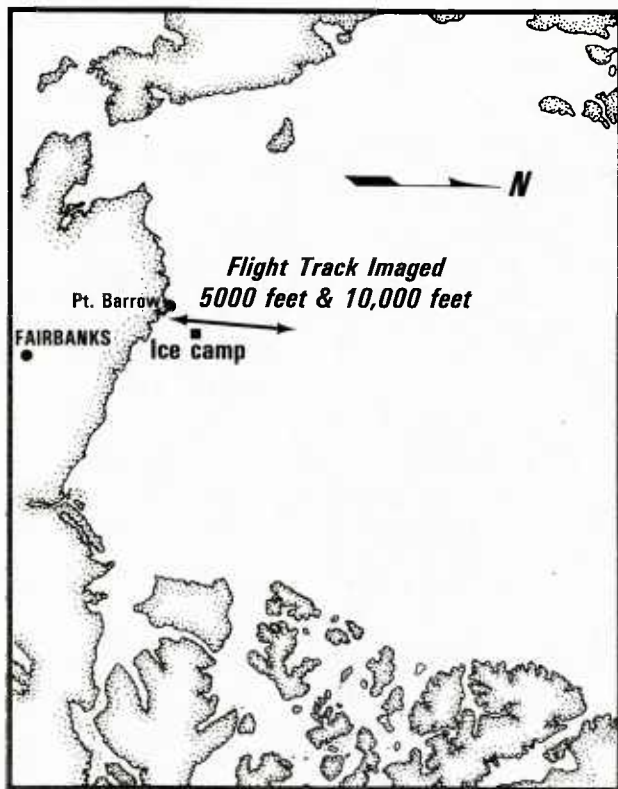


Figure 17. Map of the Beaufort Sea showing location of the flight line along which data presented here were collected.

## Old ice

The range of brightness temperatures spanned by old ice (second-year ice, Fig. 20; and multi-year ice, Fig. 21) is greater than that spanned by either open water or young ice and first-year ice.

A division within the old ice category is suggested by differences in the range of brightness temperatures characteristic of multi-year and second-year ice (Figs. 20c and 21c). The range of multi-year ice is greater than that of second-year ice and extends to warmer temperatures. Occurrence of well-developed, radiometrically warm frozen fresh-water meltponds and the presence of cold relict ridges on multi-year floes present a broader range of surface types than is present on younger second-year ice.

## First-year and young ice

Brightness temperature distributions measured for grey-white ice and ridged, rafted, and smooth first-year ice are not sufficiently different to permit discrimination between these groups on the basis of brightness temperature alone. In subsequent discussions they are combined to form the first-year ice category. This is not to say that grey-white ice and ridged, rafted, and smooth first-year ice are indistinguishable from one another in KRMS imagery. Although ranges of brightness temperatures

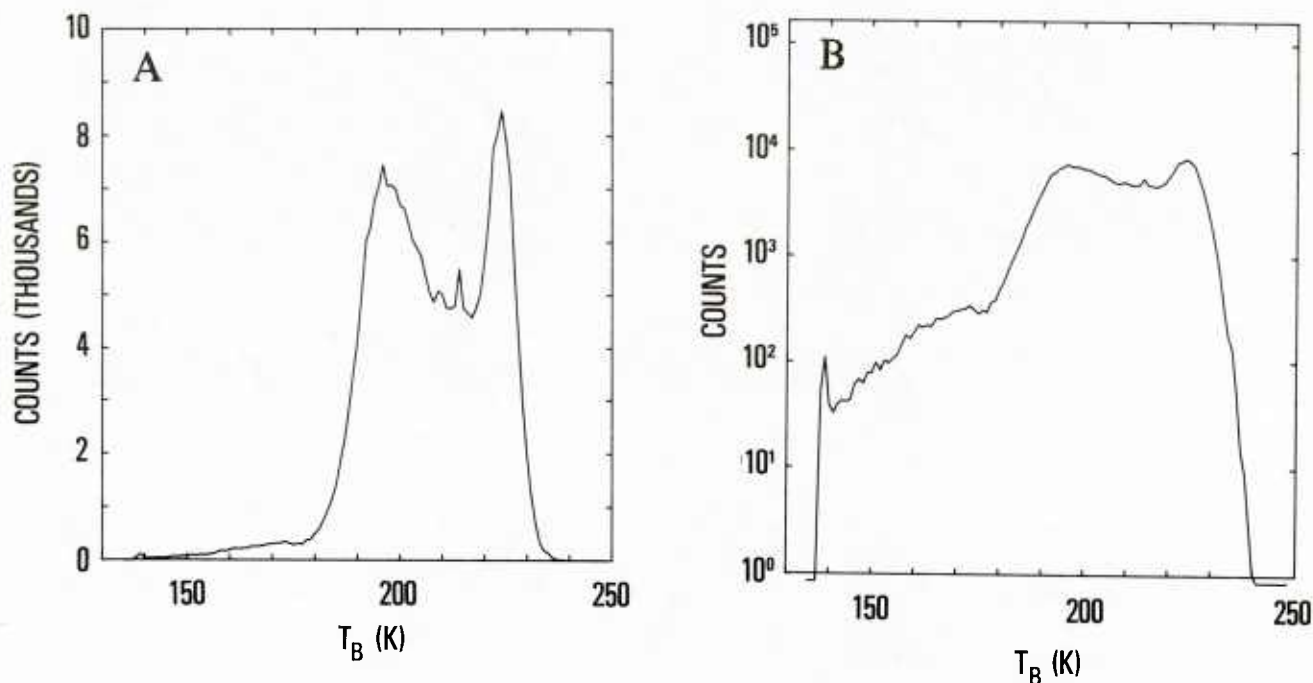


Figure 18. Frequency distribution of brightness temperatures in the scene imaged in Figure 1 of this report. Two renditions of the same data are shown. Counts are presented both on a linear scale (A) and on a logarithmic scale (B).





Figure 19a.

Figure 19. Example of training regions selected to characterize brightness temperatures typical of open water. The calibrated KRMS image is shown in a. Brightness temperatures of pixels enclosed within blotched areas (grey lines) were used to determine the range and distribution of temperatures typical of open water. Coincident aerial photographs of the central portion of the image are shown in b. Frequency distributions of pixels within the scene are shown in c.

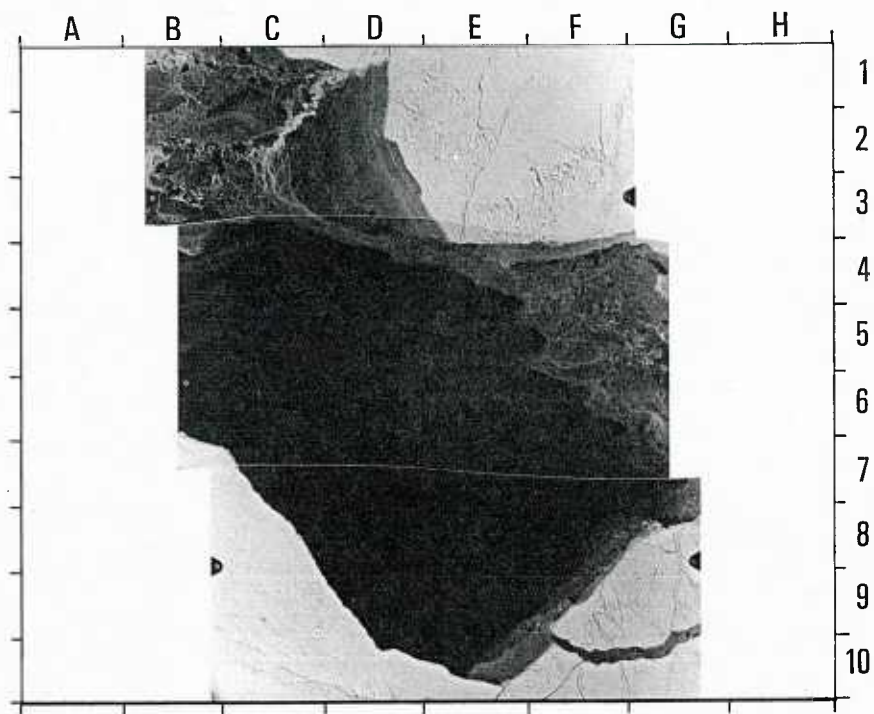


Figure 19b.

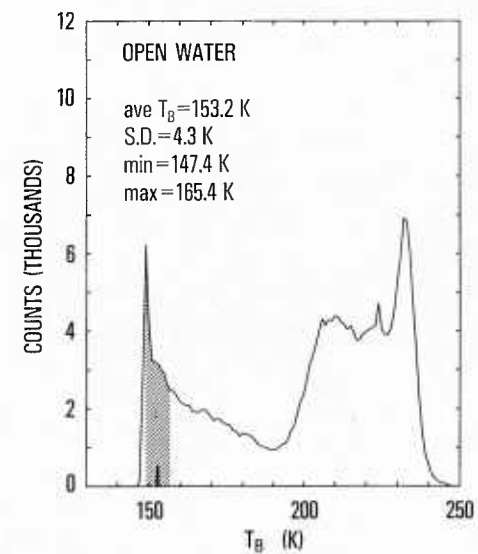
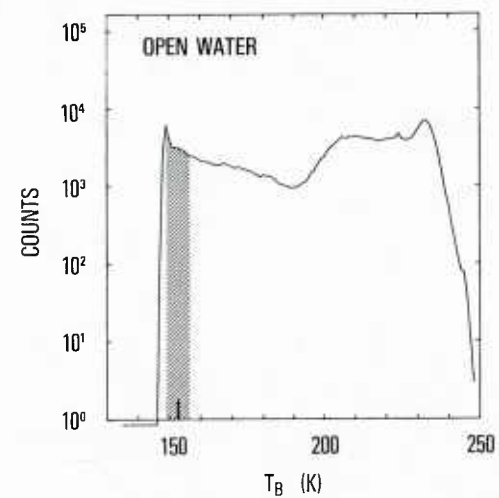


Figure 19c.

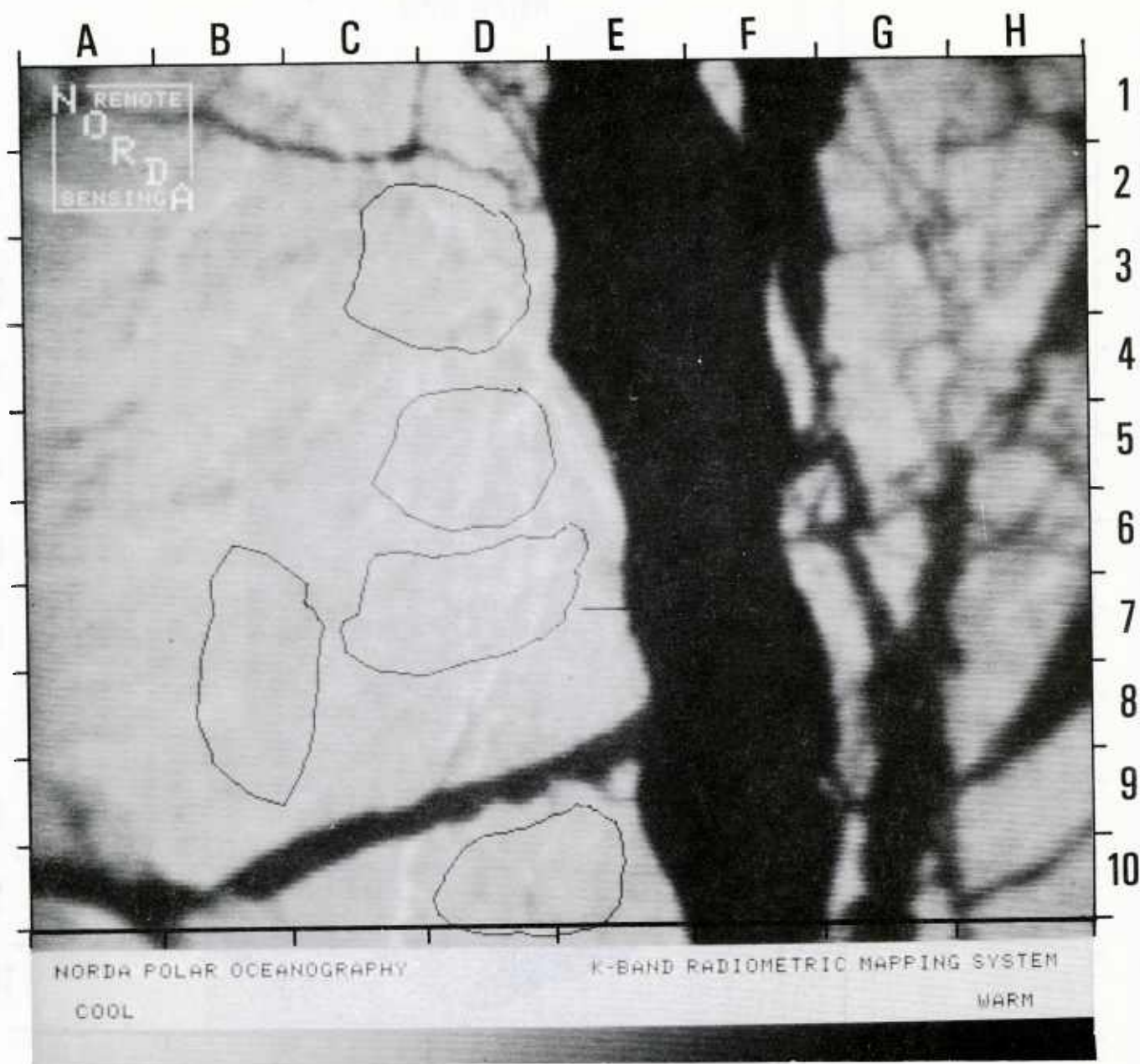


Figure 20a.

Figure 20. Example of training regions selected to characterize second-year ice. The calibrated KRMS image is shown in a. Brightness temperatures of pixels enclosed within blotched areas (grey lines) were used to determine the range and distribution of temperatures typical of open water. Coincident aerial photographs of the central portion of the image are shown in b. Frequency distributions of pixels within the scene are shown in c.

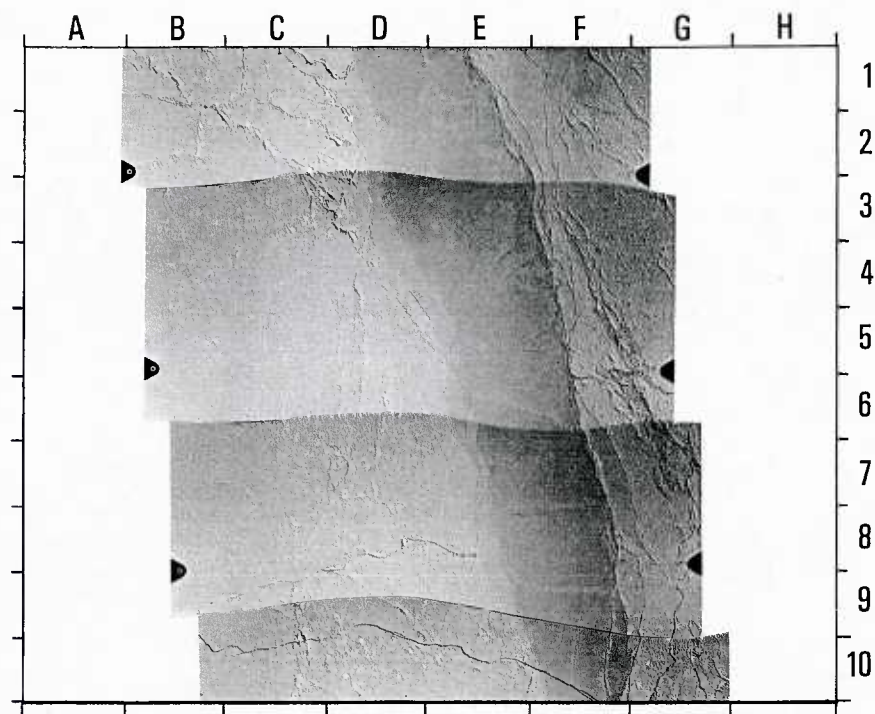


Figure 20b.

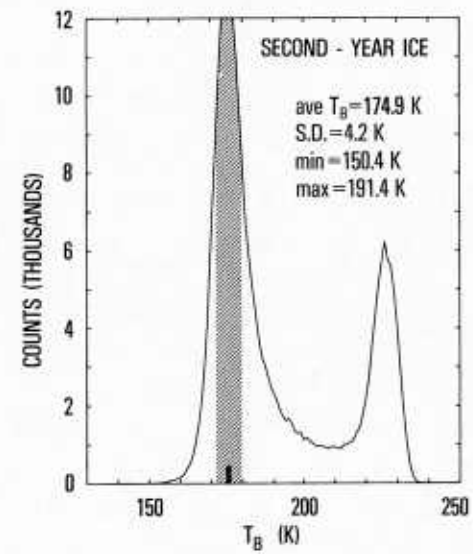
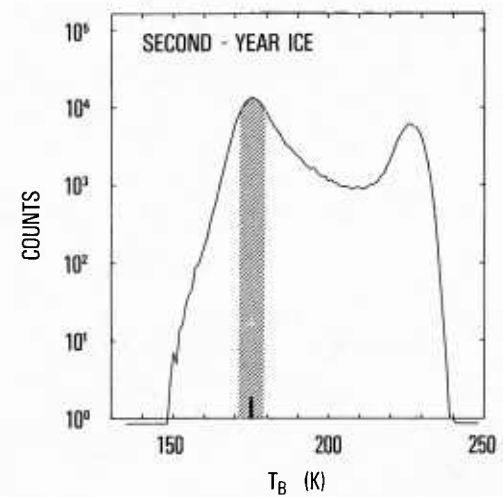


Figure 20c.





Figure 21a.

Figure 21. Example of training regions selected to characterize multi-year ice. The calibrated KRMS image is shown in a. Brightness temperatures of pixels enclosed within blotched areas (grey lines) were used to determine the range and distribution of temperatures typical of open water. Coincident aerial photographs of the central portion of the image are shown in b. Frequency distributions of pixels within the scene are shown in c.

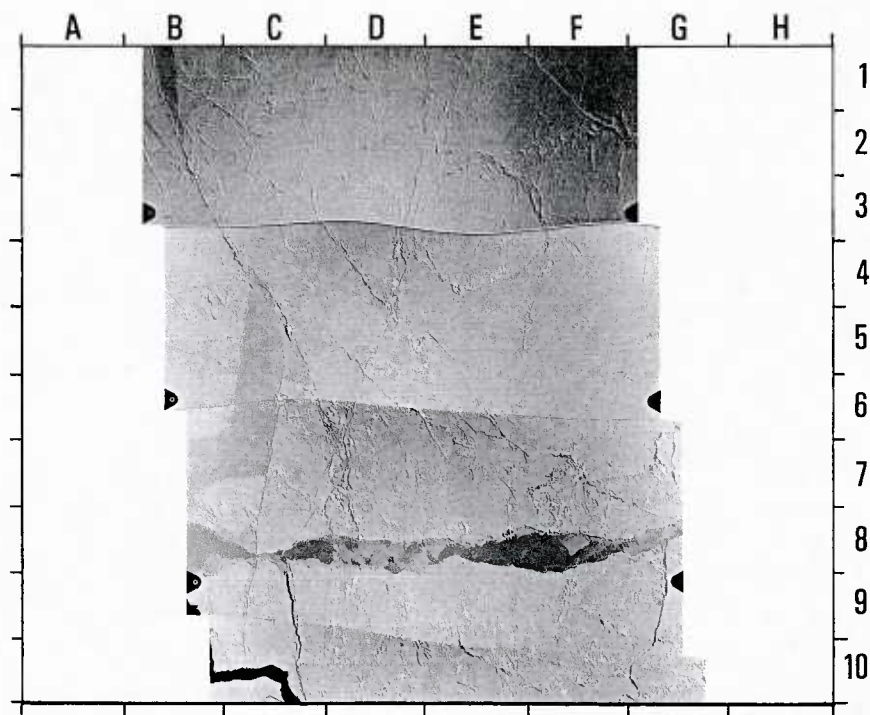


Figure 21b.

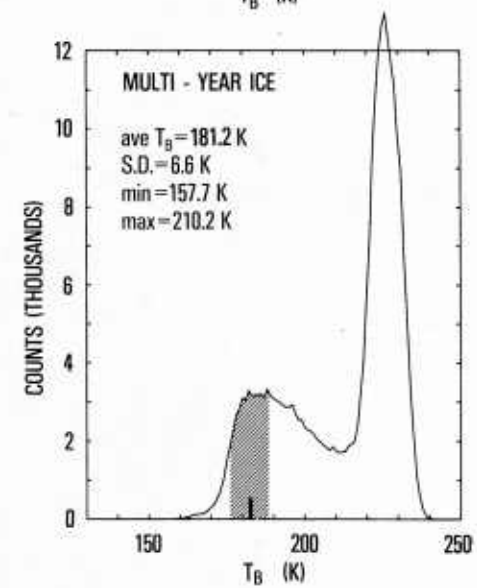
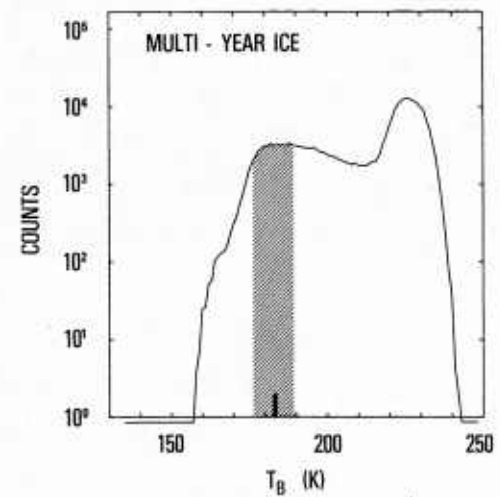


Figure 21c.



Figure 22a.

Figure 22. Example of training regions selected to characterize young ice. The calibrated KRMS image is shown in a. Brightness temperatures of pixels enclosed within blotched areas (grey lines) were used to determine the range and distribution of temperatures typical of open water. Coincident aerial photographs of the central portion of the image are shown in b. Frequency distributions of pixels within the scene are shown in c.

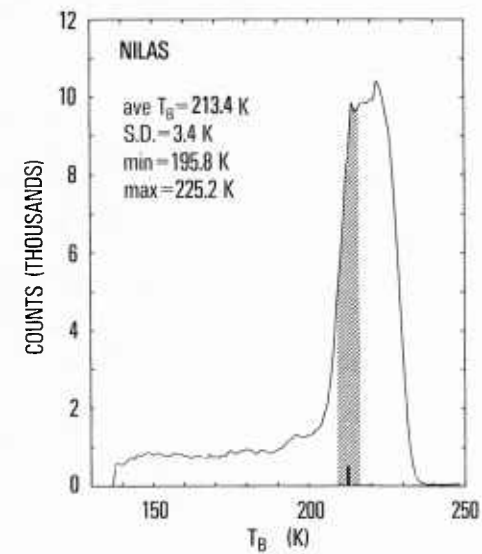
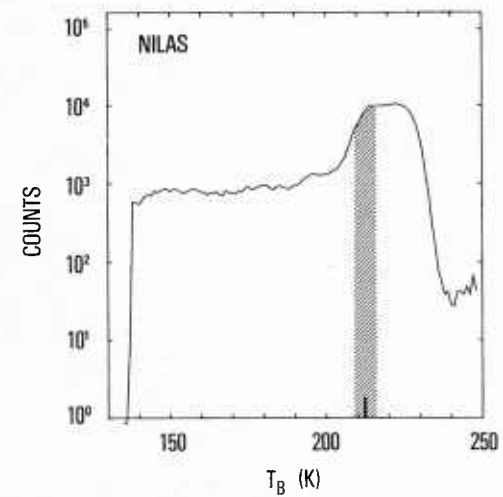
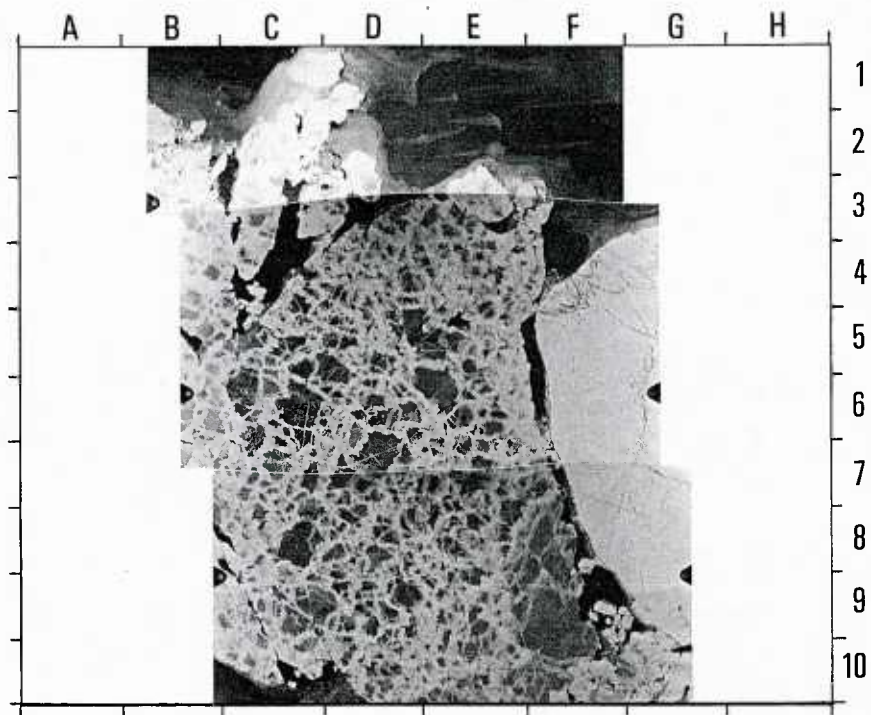


Figure 22c.





Figure 23a.

Figure 23. Example of training regions selected to characterize first-year ice. The calibrated KRMS image is shown in a. Brightness temperatures of pixels enclosed within blotched areas (grey lines) were used to determine the range and distribution of temperatures typical of open water. Coincident aerial photographs of the central portion of the image are shown in b. Frequency distributions of pixels within the scene are shown in c.

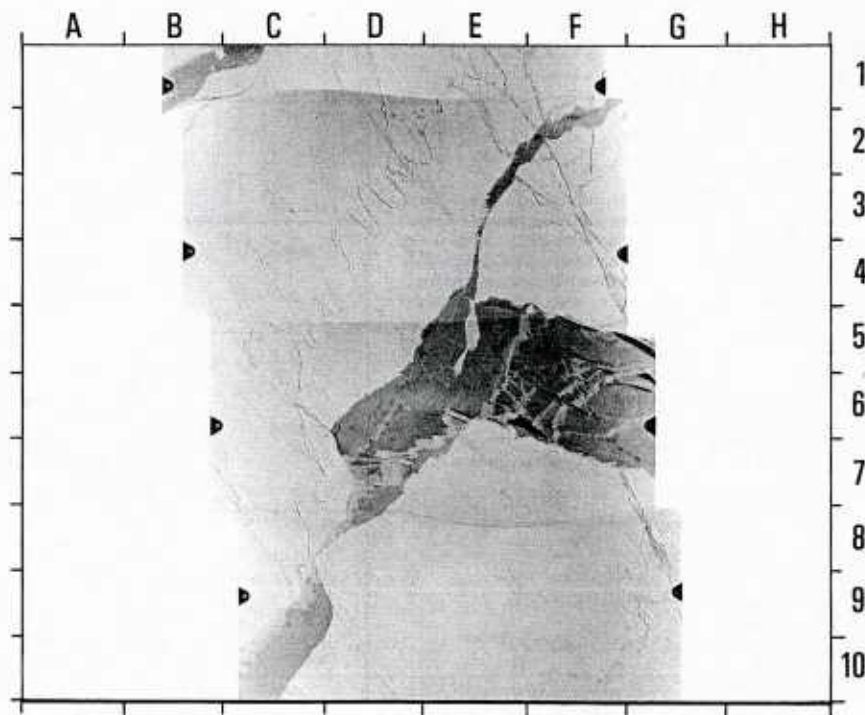


Figure 23b.

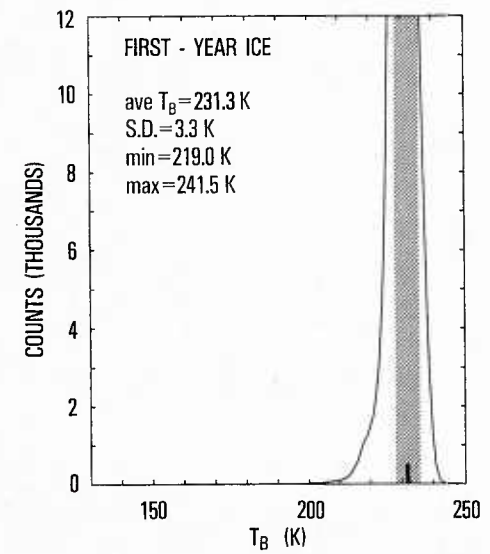
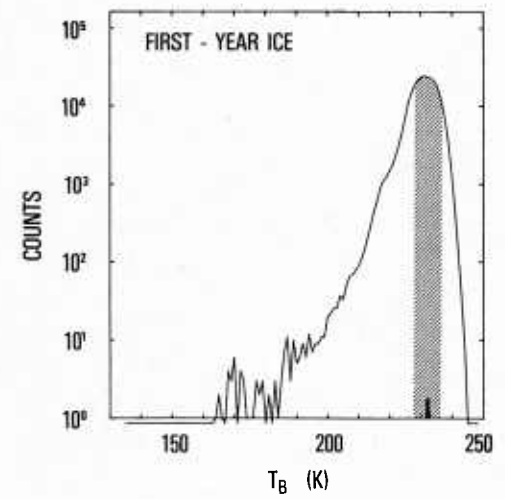


Figure 23c.

displayed by these ice types overlap, mean values of some distributions can be distinguished from each other (e.g., first-year ice, Fig. 22). Moreover, information regarding ice type or deformational features within a given ice type sometimes is contained in textural information that techniques used here fail to extract. For example, ridges in first-year ice are observed in some KRMS images as linear zones of warm brightness temperatures. The number of warm pixels that mark such ridges is small when compared to the large number of cooler pixels representative of surrounding first-year ice. These warmer pixels, though they broaden the range of values characteristic of ridged first-year ice, fail to shift distribution means significantly.

## Other ice types

Nilas (Fig. 23) and young ice types associated with newly frozen leads and bodies of open water span a wide range of brightness temperatures that coincide chiefly with old ice. Limited overlap with cooler sections of first-year ice forms also is evident (Figs. 22 and 23). A relationship between brightness temperature and ice thickness appears to exist for newly formed ice. Nilas and young ice become warmer as they grow thicker. Lack of ground truth data, however, precludes quantitative estimation of thickness on the basis of brightness temperature at this time.

## Summary statistics

Statistics for all training regions analyzed are presented in Table 3. Nomenclature used to describe ice within individual classes

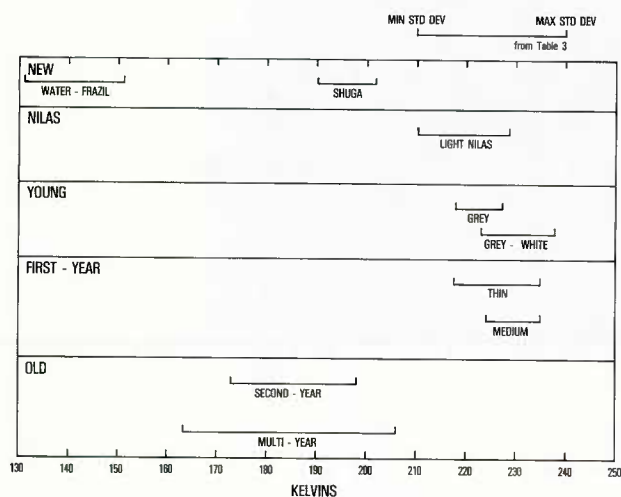


Figure 24. Summary statistics for training class data. The range of values plotted for each ice category is based on statistics calculated for pixels within BLOTCHed areas as given in Table 3. The lower end of each bar represents the minimum value calculated for one standard deviation below means given within each category (Table 3). The upper end of each bar represents the maximum value calculated for one standard deviation above means given for each category (Table 3).

(i.e., new, nilas, young, first-year, old) and subdivisions therein is based on World Meteorological Organization conventions (WMO, 1970). Broad categories of ice types defined by the mean and variance of training class statistics (Fig. 24) form an ice classification scheme based on brightness temperature. Open water represents the coldest ( $T_B$ ) surface in any of the scenes

Table 3. Training class statistics (in Kelvins)

	-1.0 st. dev.	MEAN	1.0 st. dev.
<b>NEW:</b>			
FRAZIL	130.8 141.7	139.4 147.1	148.0 151.2
GREASE		no data	
SLUSH		no data	
SHUGA	190.0	195.9	201.8
<b>NILAS:</b>			
LIGHT NILAS	210.0 222.4	213.4 225.5	216.8 228.6
DARK NILAS		no data	
ICE RIND		no data	
<b>YOUNG:</b>			
GREY	218.4 220.9 226.2 217.9	222.5 223.9 228.8 220.3	226.6 226.9 231.4 222.7
GREY-WHITE	230.9 229.2 226.7 227.6 218.6 222.7	234.3 232.1 229.1 230.7 221.1 225.3	237.7 235.0 234.5 233.8 223.6 227.9
<b>FIRST-YEAR:</b>			
THIN	224.6 228.0 222.8 228.3 224.7 220.7 224.5 216.7	228.3 231.3 225.0 230.6 227.1 223.5 227.0 220.8	232.0 234.6 227.2 232.9 229.5 226.3 229.5 224.9
MEDIUM	223.7 224.0 226.6 224.9 223.2	226.4 227.2 230.7 227.8 226.2	229.1 230.4 234.8 230.7 229.2
THICK		no data	
<b>OLD:</b>			
SECONDEYEAR	178.4 170.7 174.6 187.0 172.2 175.6	181.6 174.9 181.2 192.7 176.8 179.4	184.8 179.1 187.8 198.4 181.4 183.2
MULTIYEAR	172.0 188.8 167.3 162.7 183.1 173.4 180.7	176.4 197.6 171.1 168.7 187.6 179.3 189.5	180.8 206.4 174.9 174.7 192.1 185.2 198.3

analyzed and defines a category at the low end of the brightness temperature spectrum. Brightness temperatures measured within areas of open water fall between 135 K and 155 K. Old ice falls in the intermediate portion of the spectrum and defines a second category. Temperatures of old ice range from approximately 155 K to 210 K. Young ice and first-year ice are the warmest surfaces in the scene and constitute a third category at the upper end of the brightness temperature range. Brightness temperatures characteristic of young ice and first-year ice fall between 210 K and 248 K.

## Piecewise linear interpolation

KRMS scenes were classified at a three-class level using these interval boundaries. The I<sup>2</sup>S PLIM function (Stephenson, 1983) was employed to perform a piecewise linear interpolation on several images. The PLIM function sets all pixels with values that fall within a given interval to the same chosen value. Lower and upper boundaries that define the three ice categories given above were used to define the intervals. Values of pixels that fall within the bounds of a given interval were set to an arbitrary level chosen for that interval. Next, the I<sup>2</sup>S COLORS function was used to assign colors to pixels in each interval, producing images in which surfaces that corresponds to the specific brightness temperature ranges defined by PLIM were cast in identifying colors.

Several KRMS scenes were classified according to this three level scheme. Although open water, first-year ice, and old ice surfaces generally were classified correctly, several shortcomings of the three-level scheme became evident. First, zones of frazil and extremely thin, newly formed ice were classified incorrectly as open water. Therefore, the range of brightness temperatures usually assigned to open water (135 K to 155 K) was divided into two categories, one from 135 K to 145 K that corresponds primarily to open water, and another from 145 K to 155 K that corresponds to frazil.

Second, detail of features within old ice floes and first-year and young ice was lost because a single color was used to represent the entire range of brightness temperatures assigned to each category. Therefore, the range of values representative of each category was divided into several smaller groups. Each group was assigned a color similar to other colors within the category. The young/first-year ice category was arbitrarily divided into four subcategories (210 K to 219 K, 219 K to 224 K, 224 K to 230 K, and 230 K to 248 K) to display deformational features that occur within first-year ice. Old ice was divided into five groups (155 K to 168 K, 168 K to 183 K, 183 K to 195 K, 195 K to 200 K, and 200 K to 210 K) to accentuate meltpond and ridge structures, and to attempt discrimination between second-year and multi-year ice.

Incorporation of these changes results in an 11-color image in which four types of surfaces are classified: 1) open water (135 K to 145 K), 2) new (frazil) (145 K to 155 K), 3) old ice (155 K to 210 K), and 4) young/first-year ice (210 K to 248 K). This color classification scheme is shown in Figure 25.

## Interpretation of KRMS images

More than 30 KRMS images recorded at 5000-ft altitude were classified according to procedures discussed previously. False-color images of each scene were made by applying the 11-color scheme (Fig. 25). Three examples of color-classified KRMS images are presented here (Figs. 26-28). Each figure consists of four parts: a) the raw black and white KRMS image, b) coincident aerial photographs, c) the color classified KRMS image, and d) histograms of brightness temperature distributions observed across each scene.

### Example 1 (Figure 26)

Figure 26 shows a scene in which radiometrically cold ice floes (blue) are set in a matrix of radiometrically warm young ice (tan) (Fig. 26c A8, C1 to A5, D8, H8) and thin first-year ice (brown) (Fig. 26c E2, H2). Aerial photographs (Fig. 26b) show that the surface of the old-ice floe at F6 is relatively smooth. Small-scale roughness attributed to snow cover and ablation features is present throughout the flow, suggesting second-year ice. The cold radiometric signature (blue) coupled with small-scale roughness of the surface (ablation features) make classification as second-year ice most likely. Other radiometrically cold floes in the scene (Fig. 26b D1 to H1, A2) probably are composed of multi-year ice rather than second-year ice. Surface textures on these floes are rougher; ablation features are more pronounced; and ridges, some of which are annealed (Fig. 26b C1 to D1), are more numerous than on the second-year ice floe at F6 (Fig. 26b).

Ridges within old ice generally (though not always) are correlative with lineaments in KRMS images. For example, the ridge that extends from F3 to G1 on the photograph (Fig. 26b) corresponds to a broad lineament that is radiometrically warmer than surrounding ice and extends from F2 to G1 on the KRMS images (Figs. 26a and 26c). In another example, the ridge that extends from D3 to D7 in Figure 26b is associated with a cool lineament that extends from E4 to D6 in Figures 26a and 26c.

Young ice, depicted in brown and tan, extends across the bottom third of the image (Fig. 26c A7 to H7, A9 to H9). Although most of this area is comprised of rafted young grey ice, some areas of light nilas are present (Fig. 26b B9 to C9). Rifts in the young ice cover appear as short, cold lineaments on the raw KRMS image (Fig. 26a E7, F7, E8, E9). Histograms of brightness temperatures present in the scene (Fig. 26d) fail to show





Figure 25. Color scheme used to classify KRMS images on the basis of brightness temperature. Temperature ranges that each color represents are shown to the right of the color bar along with color names used in the text to describe color classified images.

temperatures typical of open water and frazil (135 to 155 K), indicating that these rifts contain new ice and do not expose water.

A small area filled with medium first-year ice occurs between old ice floes at E2-F2 in Figure 26a (E3 in Fig. 26b). Thin first-year ice fills a lead at B4-C1 in Figure 26a (B2 in Fig. 26b). Thin first-year ice and young grey ice in this scene are characterized by similar brightness temperatures (compare B4-C1 (tan, thin first-year ice) with D8 and F10 (tan, young grey ice) in Fig. 26c). These ice types cannot be distinguished unambiguously based on brightness temperature alone and so are lumped together in terms of the classification scheme shown in Figures 24 and 25.

### Example 2 (Figure 27)

Figure 27 shows a scene in which old-ice floes (blue) border a broad frozen lead of medium first-year ice (tan and brown). These old floes (Figs. 27a and 27c B8, D3, E1, F2, H4 and Fig. 27b C8, C3, D2, E3, G5), though similar in appearance to the second-year floe in Figure 26, are characterized by slightly rougher surfaces and cooler brightness temperatures (168 K to 183 K). These floes also are believed to be composed of second-year ice due to their even texture and the lack of well-developed drainage networks.

Ridges in these second year floes (Fig. 27) range in character from old annealed ridges that show little surface relief (Fig. 27b C3, E3) to new ridges that retain a blocky, serrated appearance (Fig. 27b D3). Old ridges in photographs (Fig. 27b) commonly are correlative with the coldest features in the KRMS scene (Fig. 27d, 155-168 K) and appear as dark blue lineaments in the color image (Fig. 27c D2, F2). New ridges shown on photographs (Fig. 27b) within second year ice commonly are correlative with lineaments that are radiometrically warmer than adjacent ice in this scene and appear as light blue lineaments (Fig. 27c D1 to D3, C2 to D2, E3 to F1). Ridges in first-year ice, when they are apparent, appear radiometrically warmer than the surrounding first-year ice (Fig. 27b D5 to E8 and Fig. 27c E4 to E9).

### Example 3 (Figure 28)

The third classified scene (Fig. 28) shows a more complex assemblage of ice types than either of the two previous examples. Old ice floes (blue-green) occur with thin first-year ice (tan, Fig. 28c D5, G1 to H5), nilas and young ice of various thicknesses (brown-green-blue, Fig. 28c C9, D10, E10), and small areas of open water (black) and new ice (blue-pink, Fig. 28c D1 to E2). Old ice floes are characterized by hummocky surfaces (Fig. 28b). Annealed ridges (Fig. 28b D3, D6, F5) are common. The range of brightness temperatures typical of these multi-year floes (168-210 K) is warmer than that typical of second-year floes imaged in Figures 26 and 27 (155-195 K). Classification of these floes as multi-year ice is based primarily on surface morphology (annealed ridges and meltponds) and their rounded shapes.

First-year ice in the scene is characterized by uniform texture (Figs. 28a and 28b). Brightness temperatures fall within the upper range for first-year ice (224-248 K, Fig. 25). Ridges observed in photographs (Fig. 28b C2 to D4, E6 to G6) are associated with radiometrically warm lineaments in KRMS images (Figs. 28a and 28c C2 to D4, E6 to G6).

Brightness temperatures characteristic of nilas and young ice fall within a broad range (168-224 K) and overlap temperatures typical of old ice (168-200 K) and, to a lesser extent, first-year ice (210-248 K). Textural characteristics of nilas and young ice (Fig. 28c C9 to E9, C10 to E10) differ markedly from the uniform appearance of first-year ice (Fig. 28c G1 to H5). Nilas and young ice in the KRMS scene (Figs. 28a and 28c) are characterized by banded textures that are caused by lateral transitions between ice of different physical character (thickness, salinity, surface moisture, snow cover). A bull's eye pattern characterizes new ice types that surround three small areas of open water (Fig. 28c D1 to E2). Here, new ice (pink) and nilas (dark blue to dark brown) encroach on open water areas (black).



Figure 26a.

Figure 26. Color-classified KRMS image of second-year and young/first-year ice. The calibrated black and white KRMS image is shown in a. Coincident aerial photographs of the central portion of the KRMS image are shown in b. The color-classified KRMS image is shown in c. Frequency distributions of measured brightness temperatures are shown in d. Area imaged in KRMS scenes shown here and in Figures 27 and 28 is 3600 m (11,900 ft) cross-track (side to side) and 3200 m (10,500 ft) down-track (top to bottom). Area shown in photo-mosaics is 2300 m (7500 ft) cross-track and 3200 m (11,900 ft) down-track.

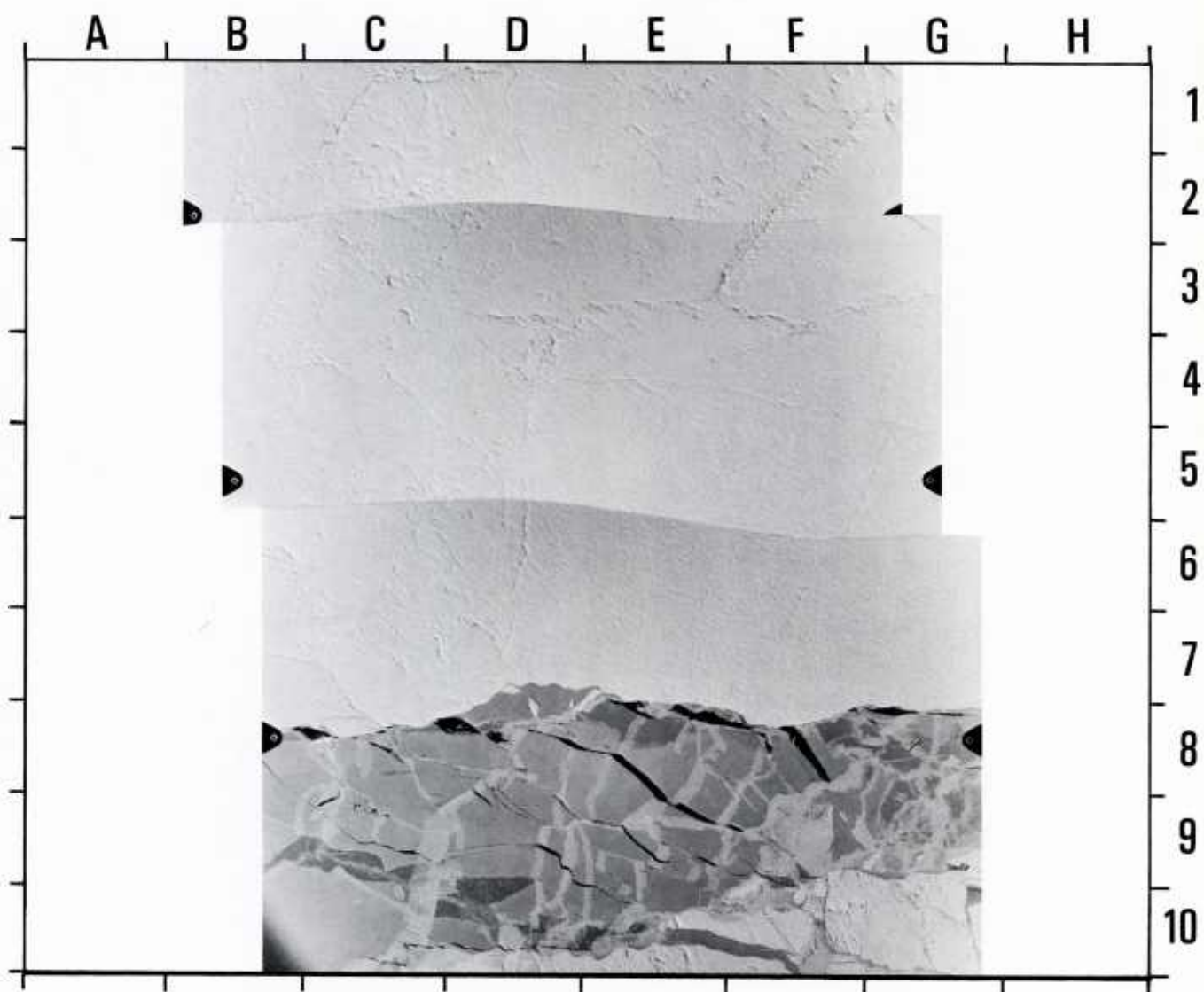


*Figure 26b.*



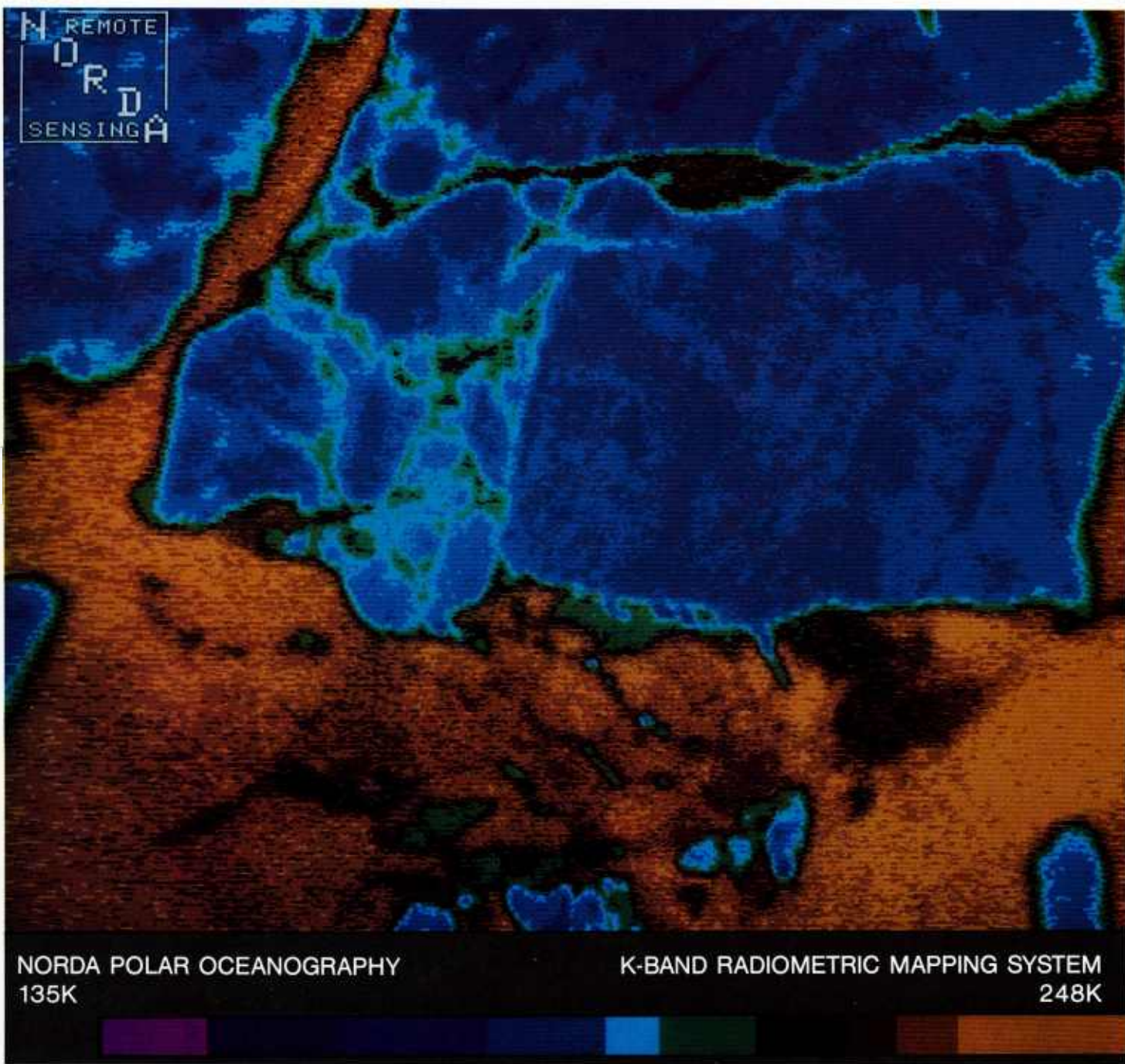


Figure 26c.

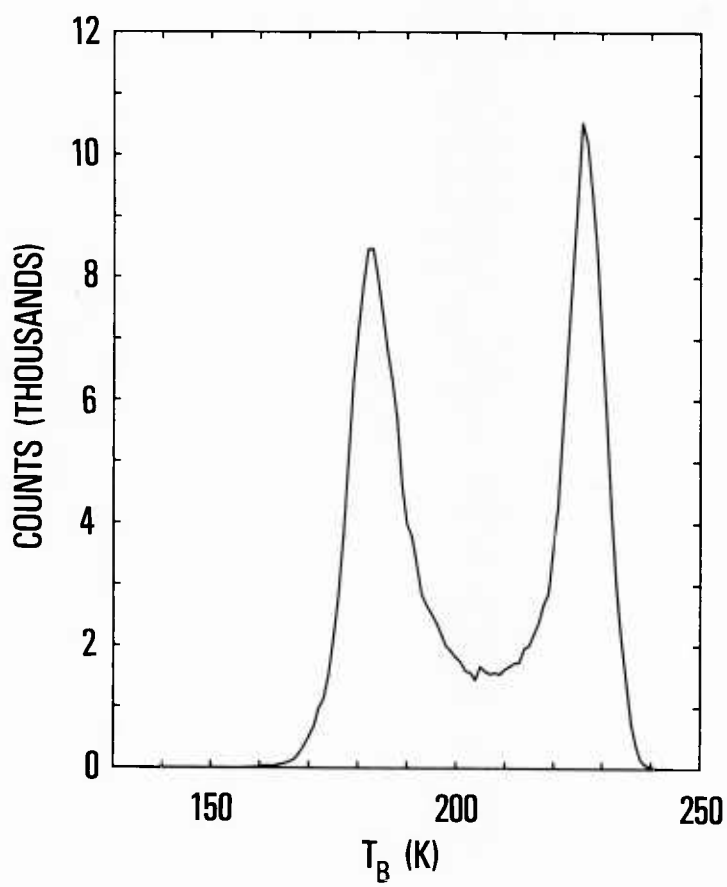
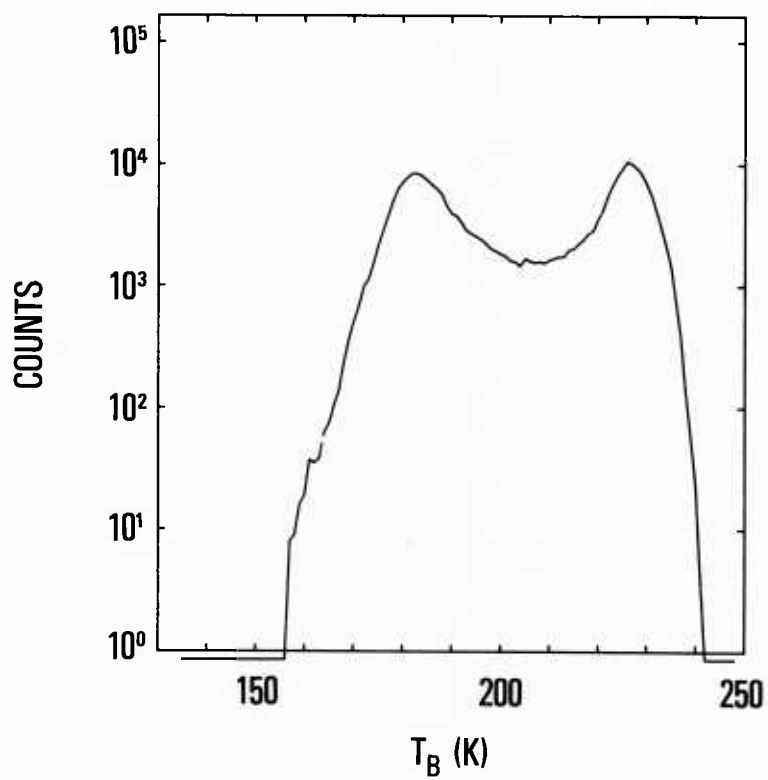


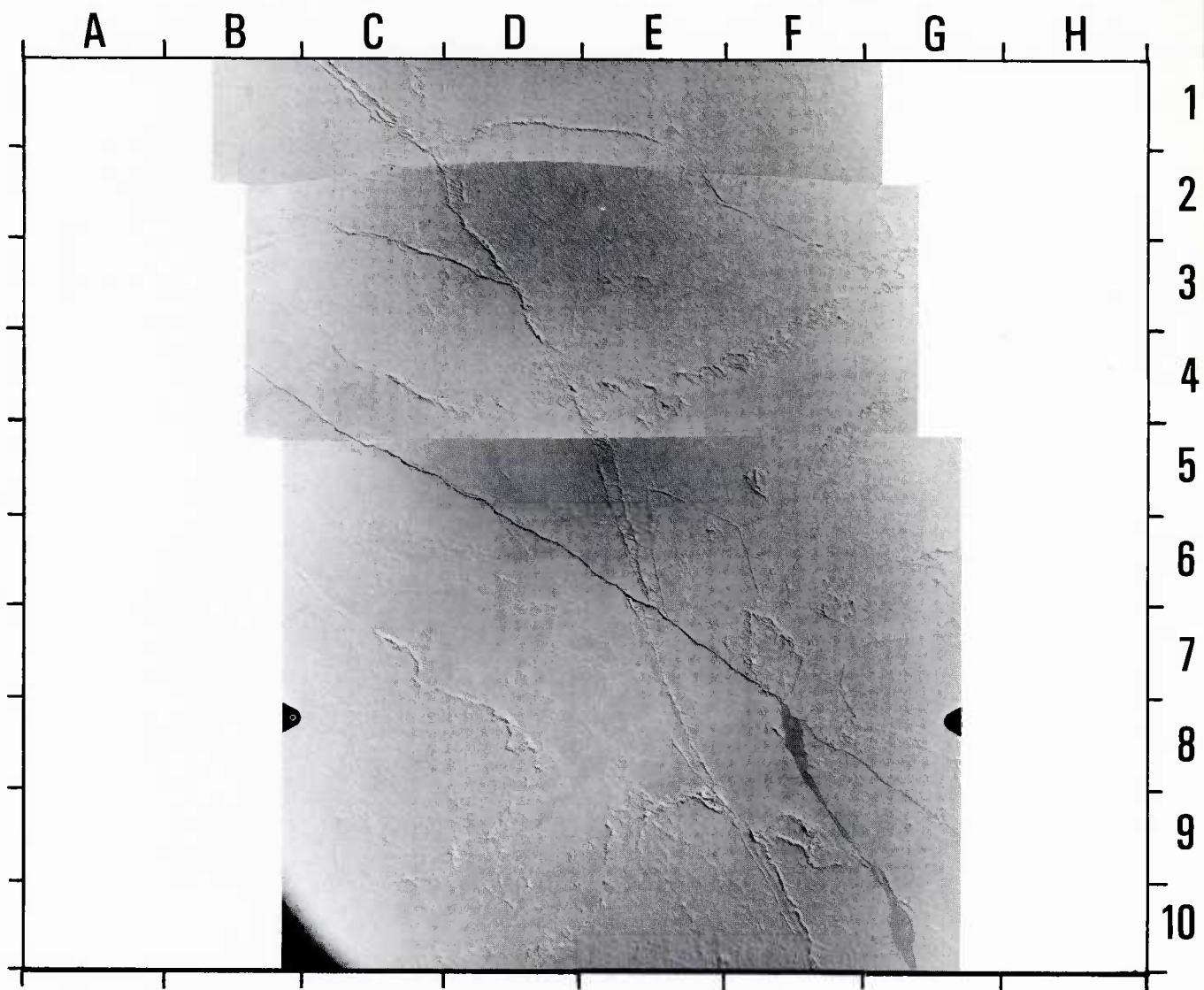
Figure 26d.



Figure 27a.

Figure 27. Color-classified KRMS image of second-year and young/first-year ice. The calibrated black and white KRMS image is shown in a. Coincident aerial photographs of the central portion of the KRMS image are shown in b. The color-classified KRMS image is shown in c. Frequency distributions of measured brightness temperatures are shown in d. Area imaged in KRMS scenes shown here and in Figures 27 and 28 is 3600 m (11,900 ft) cross-track (side to side) and 3200 m (10,500 ft) down-track (top to bottom). Area shown in photo-mosaics is 2300 m (7500 ft) cross-track and 3200 m (11,900 ft) down-track.





*Figure 27b.*



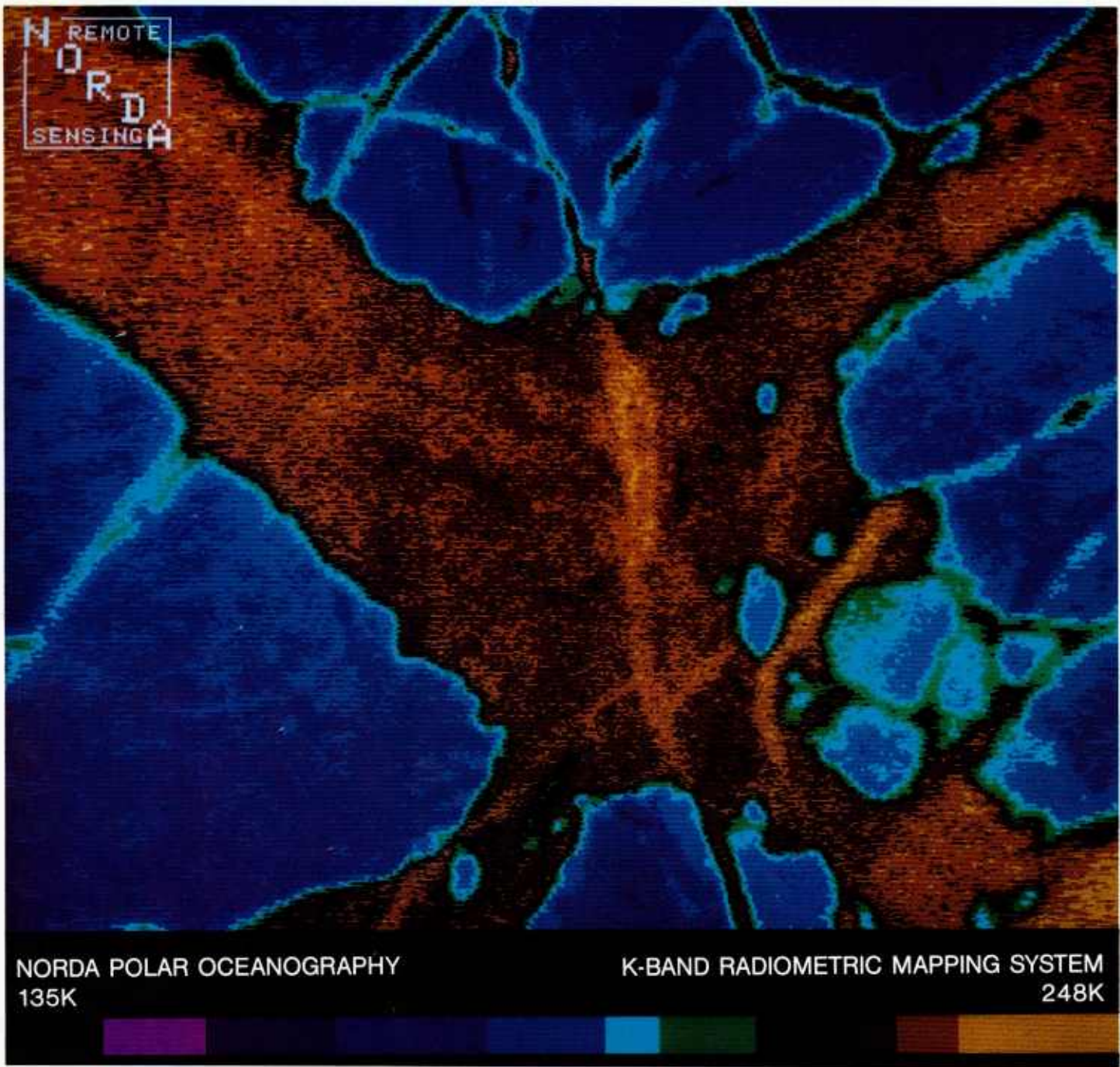


Figure 27c.

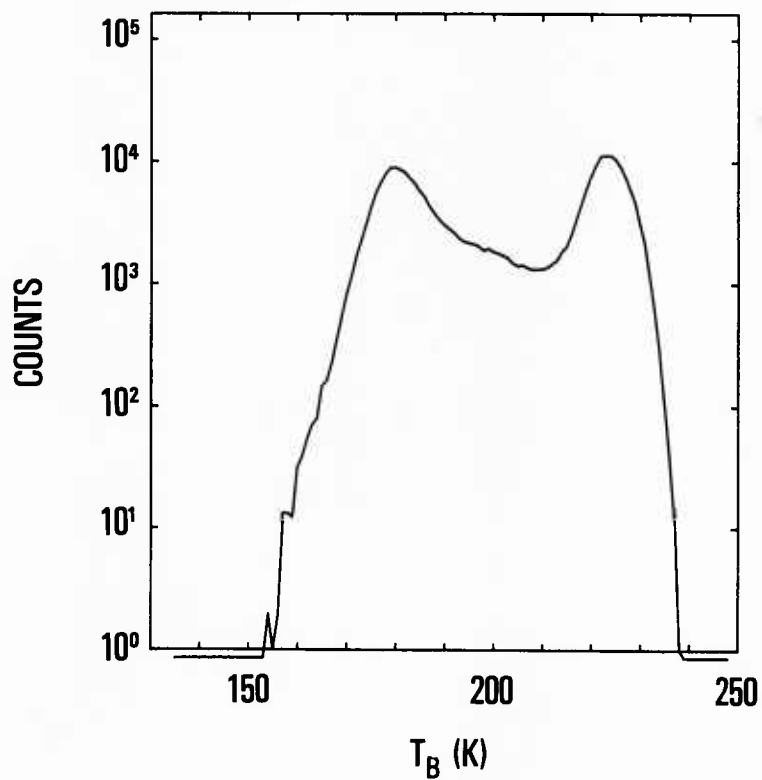
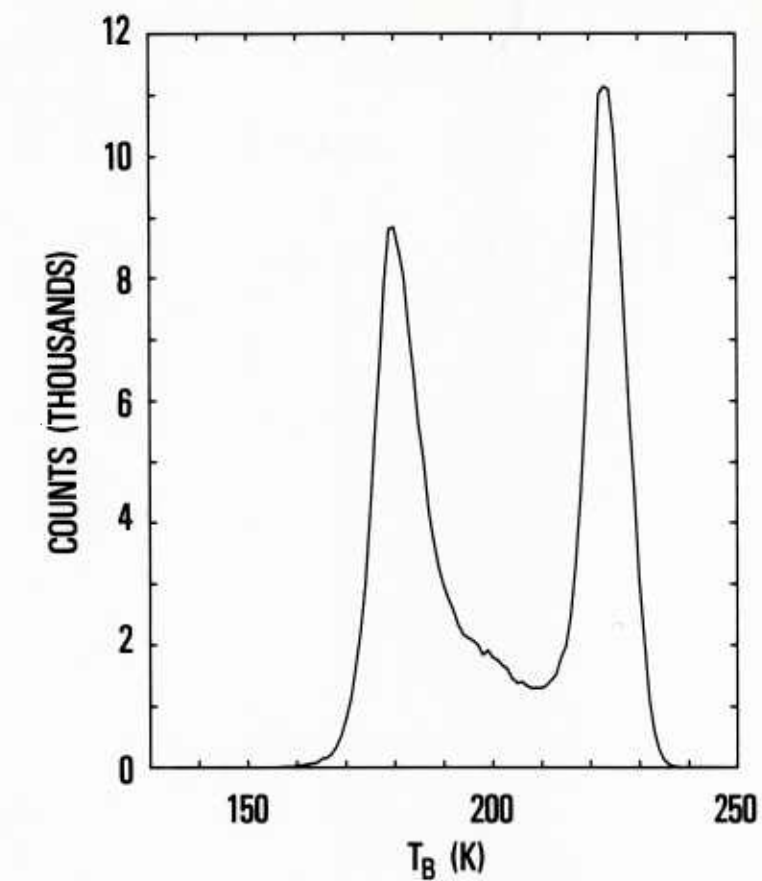


Figure 27d.

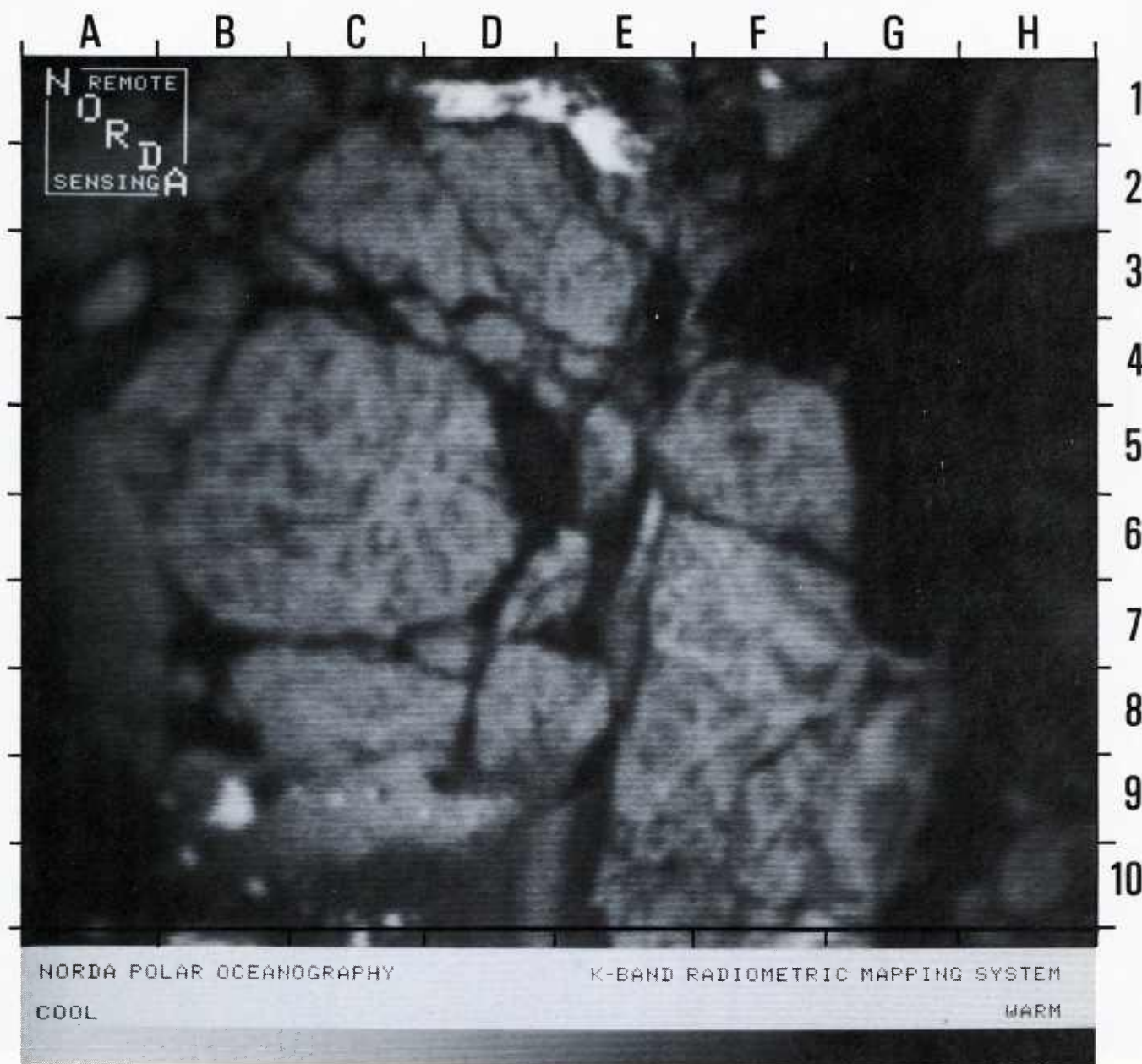
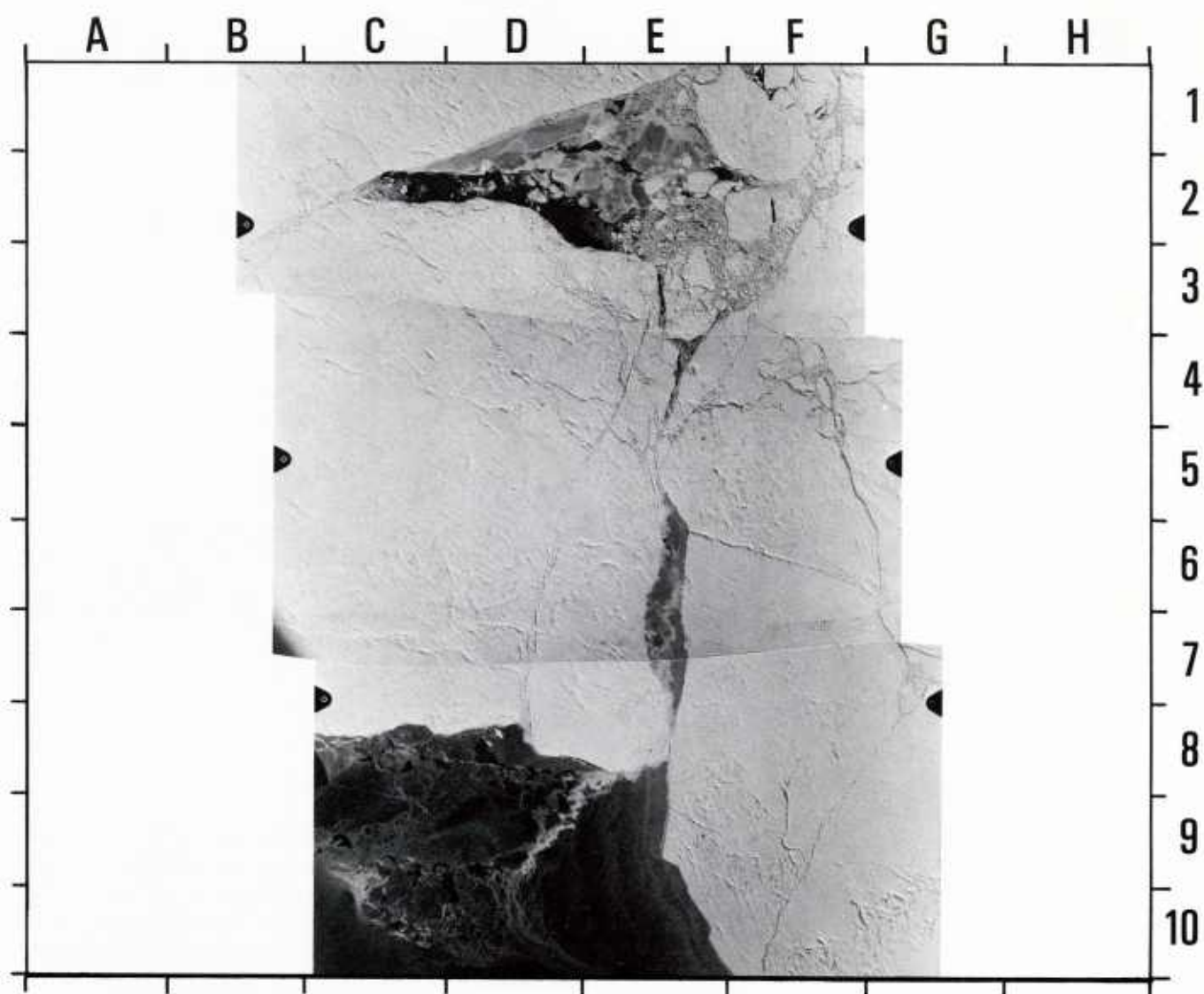


Figure 28a.

Figure 28. Color-classified KRMS image of multi-year ice, young/first-year ice, new (frazil) ice, and open water. The calibrated black and white KRMS image is shown in a. Coincident aerial photographs of the central portion of the KRMS image are shown in b. The color-classified KRMS image is shown in c. Frequency distributions of measured brightness temperatures are shown in d. Area imaged in KRMS scenes shown here and in Figures 27 and 28 is 3600 m (11,900 ft) cross-track (side to side) and 3200 m (10,500 ft) down-track (top to bottom). Area shown in photo-mosaics is 2300 m (7500 ft) cross-track and 3200 m (11,900 ft) down-track.





*Figure 28b.*



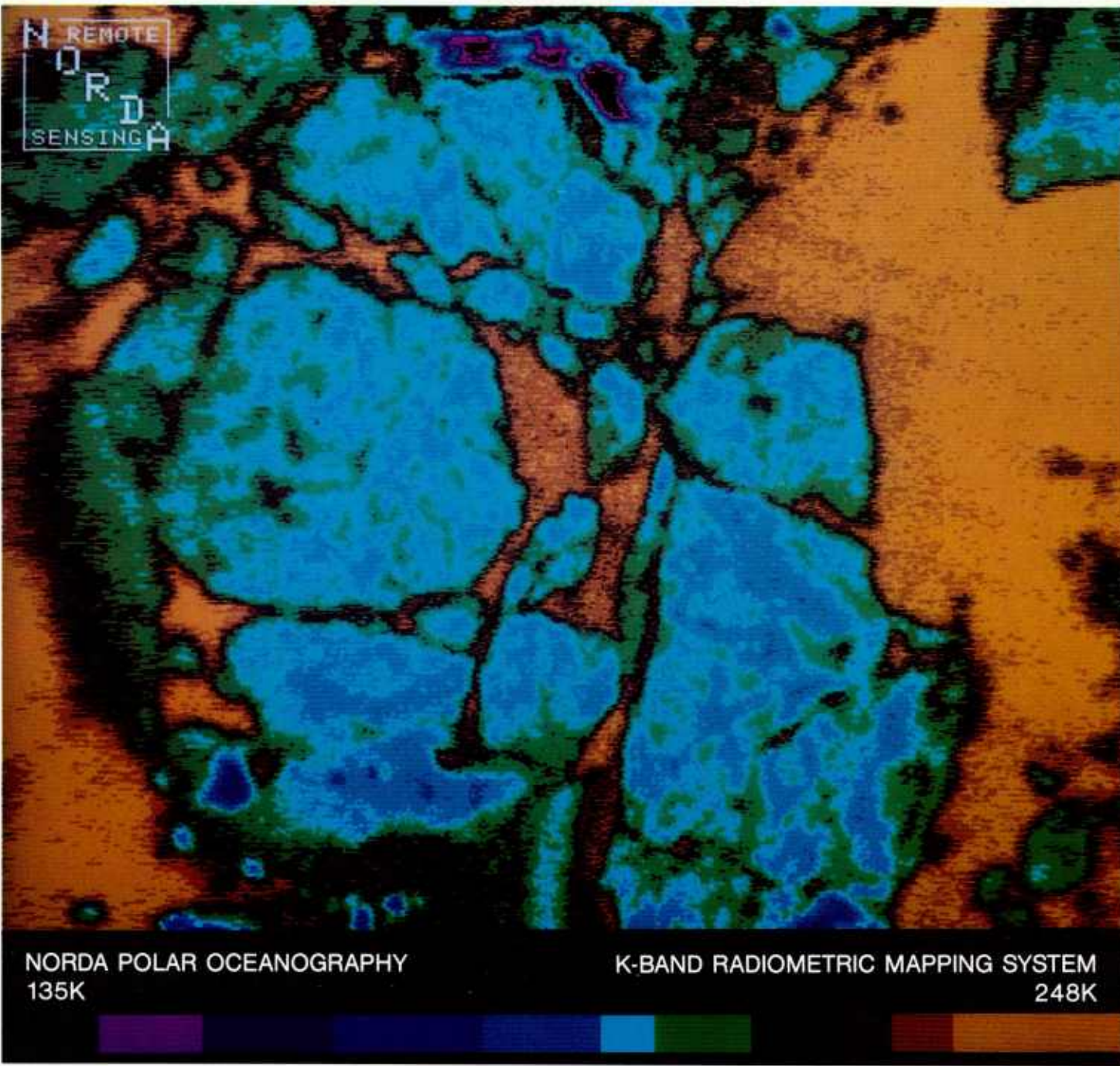


Figure 28c.

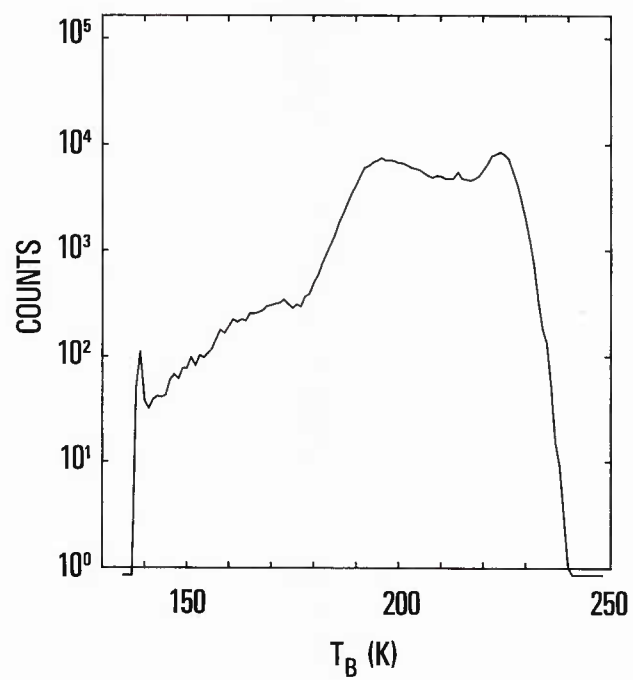
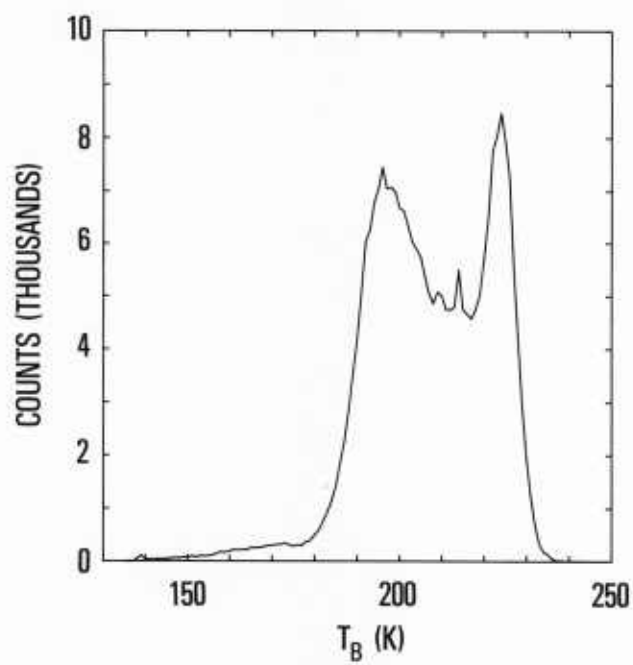


Figure 28d.

## Classification error

Work outlined above defines the extent to which winter ice in KRMS imagery can be classified on the basis of measured  $K_a$ -band brightness temperature alone. Young/first-year ice, new ice (frazil), and open water can be distinguished from other surface types without substantial ambiguity. Brightness temperatures of young ice and first-year ice define a discrete class at the warm end of the spectrum, the mean temperature of which extends from approximately from 215 K to 235 K (Table 3, Fig. 24). In some instances, nilas and grey ice (Fig. 26c G8; Fig. 28c D10) display brightness temperatures that are similar to radiometrically cold forms of first-year ice (Fig. 26 E2 to F2). Insofar as new ice, nilas, and grey ice are not abundant in winter imagery, this constitutes a minor source of error with regard to this data set.

New ice (frazil) forms a second discrete class near the cold end of the spectrum between 145 K and 155 K. Isolated areas on cold ridges that occur in multi-year floes sometimes fall within this interval. The extent of each of these areas typically is limited in size to fewer than 10 pixels (Fig. 20), and their effect on estimates of new ice concentration is negligible.

Open water represents the (radiometrically) coldest surface imaged in any scene and defines a third discrete class between 135 K and 145 K. Estimates of the areal extent of exposed water that are based on brightness temperature thus are anticipated to be quite accurate.

Old ice and nilas are not easily separable from each other on the basis of brightness temperature alone. Both surfaces display brightness temperatures in the midrange of values between new ice (frazil) and young/first-year ice (155 K to 210 K) (Fig. 24). The range of temperatures observed for old ice extends from 150 K to 213 K with mean temperatures extending from 175 K to 195 K (Fig. 29). Brightness temperatures for new ice and nilas coincide with temperatures measured for old ice and span the entire midrange between new ice (frazil) and young/first-year ice (155 K to 210 K). This observed overlap leads to ambiguous classification of old ice, nilas, and new ice in schemes based on  $K_a$ -band brightness temperature alone.

In marginal ice zones, new ice, nilas, and young ice are abundant relative to the concentration of old ice. Here, ice concentrations derived from midrange temperatures (155 K to 210 K) represent concentrations of new ice and nilas. Errors in estimates of the concentration of new ice and nilas will be small as long as old ice floes are sparse or absent. In the central pack the reverse is true under winter conditions. Concentrations of new ice and nilas are low relative to concentrations of old ice. Most surfaces encountered with midrange temperatures, then, probably will be multi-year ice. Accordingly, the error in estimating old ice concentration will be small in the pack interior.

In intermediate zones where neither nilas and new ice nor old ice predominate, concentration of either is difficult to derive. Estimates of old ice concentrations from brightness temperature data might be possible if the concentration of new ice and nilas can be estimated from the concentration of open water. New ice and nilas are only produced when open water freezes; thick ice does not efface and become thin to form nilas or new ice. Therefore, the percentage of new ice and nilas present at a given time is a function of the amount of open water that has been exposed in the recent past. If a well-behaved relationship between open water concentration and the concentration of new ice and nilas can be shown to exist, errors involved in estimating old ice concentration can be reduced.

Erroneous classification observed for some surfaces arises from inherent characteristics of the sensor. The chief source of error is related to beamwidth characteristics of the KRMS antenna. Analog voltages processed by KRMS electronics are measures of energy integrated across the antenna footprint. If the beam spot straddles the boundary between surfaces of different radiometric character, energy from both surfaces is averaged to produce an intermediate temperature value. KRMS brightness temperatures measured at boundaries between first-year ice and second-year floes commonly are intermediate between the measured temperatures for first-year and second-year ice as a consequence, even though ground-based radiometer measurements suggest sharp transitions without intermediate temperatures. Green rings that occur around second-year floes in color-coded classified images (Figs. 26c and 27c), thus, are artifacts of the imaging system and do not necessarily reflect characteristics of ice at floe margins. Estimates of the abundance of ice characterized by this range of temperatures (195 K to 210 K), therefore, are inflated.

## Discussion

KRMS imagery acquired during the March 1983 mission contains a diverse assemblage of surface types that range from open water through new, nilas, and young-ice forms to first-year ice, second-year ice, and multi-year ice. Visual discrimination between surface types that occur within a particular scene is based on four factors: 1) the overall range of brightness temperatures displayed by each surface type, 2) the texture or spatial arrangement of pixels of different brightness temperatures within each surface type, 3) the shape of the area bounded by a specific ice type, and 4) the environment in the scene.

A comprehensive classification scheme might require that each of the four factors be used to achieve required accuracy. However, because some of the information contained in each factor is duplicated in others, adequate classification might be achieved using fewer than four factors. Neither the relative importance of each factor, the type of information carried by each, nor the



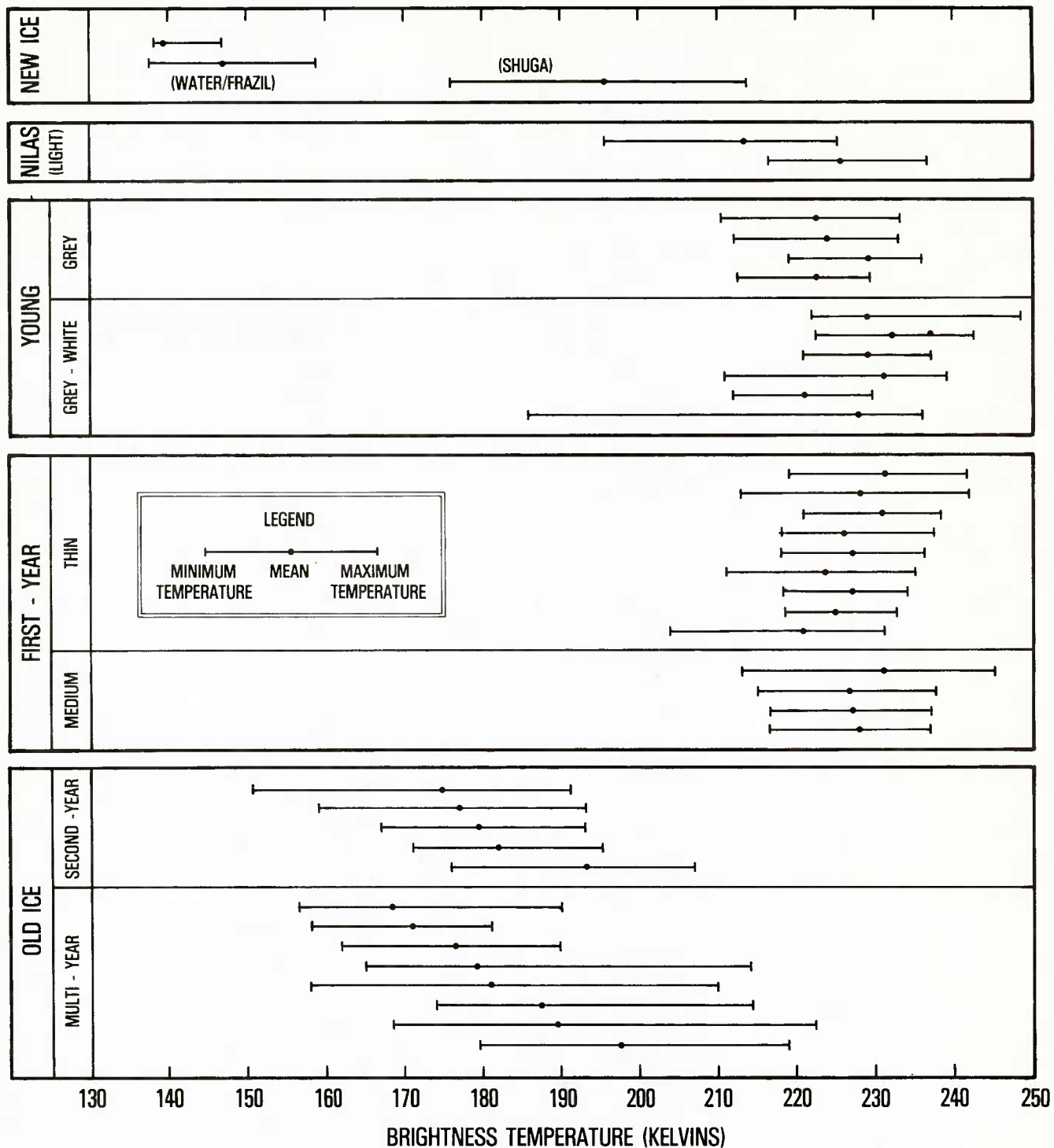


Figure 29. Summary statistics for training class data. The minimum, mean, and maximum values of pixels sampled for each ice type are shown. Each line represents a different training area.



degree to which information is redundant between them has been established to date.

Conventional ice classification schemes that utilize microwave imagery typically are based on brightness temperature characteristics and ignore texture and shape (Gloersen *et al.*, 1981b; Martin *et al.*, 1982; Troy *et al.*, 1982; Cavalieri *et al.*, 1983; Svendsen *et al.*, 1983). Environment is addressed peripherally, commonly in terms of assumptions regarding seasonal ice types that can be excluded from consideration because they are not expected to be present in significant abundances. Such schemes enjoy success in part because they employ multi-spectral data from as many as eight channels at four frequencies (Gloersen *et al.*, 1981b; Svendsen *et al.*, 1983).

Use of single-channel brightness temperature data severely limits discrimination between different surface types as shown by arctic ice classification attempts associated with the Nimbus ESMR (Gloersen *et al.*, 1974, 1978; Zwally *et al.*, 1979; Carsey, 1982; Comiso and Zwally, 1982). Because the KRMS is a single-channel instrument, acceptable ice classification algorithms evidently are not possible if brightness temperature alone is examined. Ambiguities that we have shown in classifying old ice, nilas, new ice, and young ice demonstrate this point. This is not to say, however, that adequate classification cannot be achieved from single-band imagery. Both textural differences and shape differences between areas encompassed by multi-year, second-year ice, nilas, new ice, and young ice make visual discrimination of these surface types reasonably unambiguous (Fig. 28). Use of textural, shape, and environmental information ultimately must be examined in conjunction with brightness temperature to determine whether automated classification of single-band imagery can be achieved.

## Textural analysis

Textural analysis involves recognition of features, patterns, or surface textures in imaged scenes that distinguish one type of surface from another. For example, old floes commonly include frozen meltponds and cold features associated with ridges that are never seen in young ice. Identification of these features alone is sufficient to distinguish old ice from young ice. Although visual recognition of ridges and meltponds is rapid and efficient, machine recognition of such features can be slow and inaccurate, since their presence is inferred by numeric descriptors of patterns that occur in the spatial variation of brightness temperatures across a scene.

More readily obtained statistical measures of spatial temperature variation can be used to assess differences in texture from area to area. Differences in the mean, variance, skewness, kurtosis, and range of temperature characteristic of different surfaces reflect the nature of features that occur on each surface (Table 3, Figs. 24 and 29). If a small number of pixels is viewed through a

window moving from point to point across an image, textural differences between surface types will result in changing values of the mean, variance, skewness, kurtosis, and range displayed within the window. Surfaces in which brightness temperature is uniform (nilas, new ice, open water), or in which variation in brightness temperature is characterized by a narrow range but by a large spatially random component (young ice, first-year ice), will display less variation in these parameters than surfaces in which nonrandom variation in brightness temperature occurs (old ice). The size of the window can be varied to match the spatial scale of features to be characterized. Large windows are required to detect large-scale features. Small windows capture small-scale features.

## Shape analysis

The shape of boundaries that delineate surface types is a parameter of potential importance that has not been incorporated into past classification schemes. Floe shape is a function of the interaction between dynamic processes within the pack and physical characteristics of ice involved. Image analysts use floe shape subjectively to determine floe age (first-year, second-year, multi-year) and to estimate the local intensity of processes of abrasion, erosion, deformation, and fragmentation of floes.

Floe shape, once defined, is a more stable, less transient indicator of ice properties than are brightness temperature data when images of nonwinter scenes are considered. Although individual floes change shape with time, the aggregate shape attributes characteristic of a given type of ice remain relatively constant. Old ice floes typically are rounded and new ice floes invariably are angular regardless of season.  $K_a$ -band brightness temperatures, in contrast, are subject to rapid changes as freeze-thaw processes alternately create wet and dry surfaces during summer months. Where brightness temperatures yield ambiguous results, shape characteristics might provide consistent classification criteria.

Shape can be quantified using one-dimensional closed-form Fourier descriptors (Ehrlich and Weinberg, 1970). Coordinates of pixels that delineate floe outlines are transformed to a series of harmonics. Specific harmonics that reflect relevant ice parameters can be identified using well-established statistical and multivariate data analysis techniques (Ehrlich *et al.*, 1980; Full *et al.*, 1981, 1982). Comparison of harmonics calculated for a specific floe with harmonics typical of floes in specific categories (*e.g.*, first-year, second-year, multi-year) will provide a means of classification based on shape.

## Image enhancement

Classification based on texture and shape is optimized if images are enhanced before they are analyzed. When relevant features such as ridges, meltponds, fractures, and floe outlines

are accentuated and image noise is suppressed, the efficiency and accuracy of textural and shape classifiers is increased. Elimination of extraneous information that obscures textural features and masks floe outlines is accomplished by one of three methods.

## Differencing

Differencing enhances features that differ between two renditions of the same scene. Different renditions are presented by imagery made at different altitudes, different wavelengths, or different times of the day. Features common to both scenes are used to register and overlay two images using the I<sup>2</sup>S WARP function (Stephenson, 1983). Pixels in one scene are then subtracted from those in the other using the ADD function, and the differences are displayed in the output image. Features such as edges that are exactly the same in both images cancel and do not appear in the differenced image. Features that appear in one scene but not in the other are enhanced.

Figure 30 shows a differenced image that was produced by subtracting two KRMS images of the same scene made at two altitudes (5000 ft and 10,000 ft). The resulting image shows changes in surface detail that arise from decreased altitude. Ridges and meltponds on multi-year floes as well as floe boundaries in general are enhanced as a result of differences in spatial resolution between the two images. Differencing thus permits ridges, meltponds, and other surface features to be placed in a separate image where they can be examined apart from background clutter evident in the original undifferenced frames. With floe boundaries isolated, edge-finding algorithms that form part of shape analysis procedures can be streamlined.

A second differenced image that also shows the effect of changed altitude is presented in Figure 31. Here, second-year floes are imaged in a matrix of first-year ice. Note that, although floe boundaries are accentuated as in Figure 30, ridges and other features within second-year floes are not enhanced as they were in multi-year floes (Fig. 30). This suggests that differencing could form the basis for discriminating between multi-year and second-year ice.

## Two-dimensional Fourier transform

Two-dimensional Fourier analysis quantifies textural characteristics displayed in digital scenes. Images shown in this report are displayed in what is termed the spatial domain. Specific features are expressed as assemblages of brightness temperatures that are arrayed in a two-dimensional plane. Spatial relationships between pixels are used to define each image.

Images also can be displayed in the frequency domain. In the frequency domain, specific features are described in terms of the frequency with which they recur in the spatial domain. For example, a series of equally spaced, parallel ridges, fractures,

or leads that occur repeatedly across an image define localized "sharp" features in the frequency domain. In contrast, white noise that gives some images a speckled appearance occurs at all frequencies simultaneously (and, therefore, at no single spatial frequency in particular), and is expressed as a diffuse feature in the frequency domain.

Two-dimensional Fourier analysis (Howard, 1981a, 1981b) is used to transform images from the spatial domain to the frequency domain. In the frequency domain, signatures that correspond to specific features or patterns can be identified. Features can be enhanced by removing (filtering) all frequencies not included in their particular frequency signature. Conversely, if features (such as moire patterns due to periodic noise) described by the signature are undesirable, they can be eliminated. The enhanced image then is reconverted to the spatial domain using the inverse Fourier transform. Back in the spatial domain, comparison of the enhanced image with the original image reveals surfaces from which key features have been removed.

## Level slicing

Procedures involved in level slicing are those used above to produce color images that display surface classifications (Figs. 28 to 30). Classifications, as such, are enhancements of age and thickness information that is contained within the imagery. To invoke level slicing procedures, all pixels within predetermined brightness temperature intervals are set to a common value using I<sup>2</sup>S PLIM. Resulting images may be displayed either in black and white as a series of grey tones, or in color via the COLORS function. Intervals used as input to PLIM are selected on the basis of brightness temperatures that characterize features to be enhanced. This enhancement technique could prove useful in determining growth patterns of young and first-year ice, in investigating effects of snow cover on measured brightness temperatures for multi-year and first-year ice, and in estimating thicknesses of first-year ice.

## Conclusions

Work reported here assesses the feasibility of identifying and classifying winter ice types on the basis of radiometric brightness temperatures contained in single-band (33.6 GHz) digital microwave images. Analysis of K<sub>a</sub>-band images and coincident high-resolution photographs made over the Beaufort Sea in March 1983 permits the following conclusions concerning identification of ice types under winter conditions:

1. Measured brightness temperature data obtained from a single-channel K<sub>a</sub>-band imager probably are sufficient to classify most types of winter ice uniquely when used in conjunction with textural descriptors that characterize spatial patterns of brightness temperature variation.

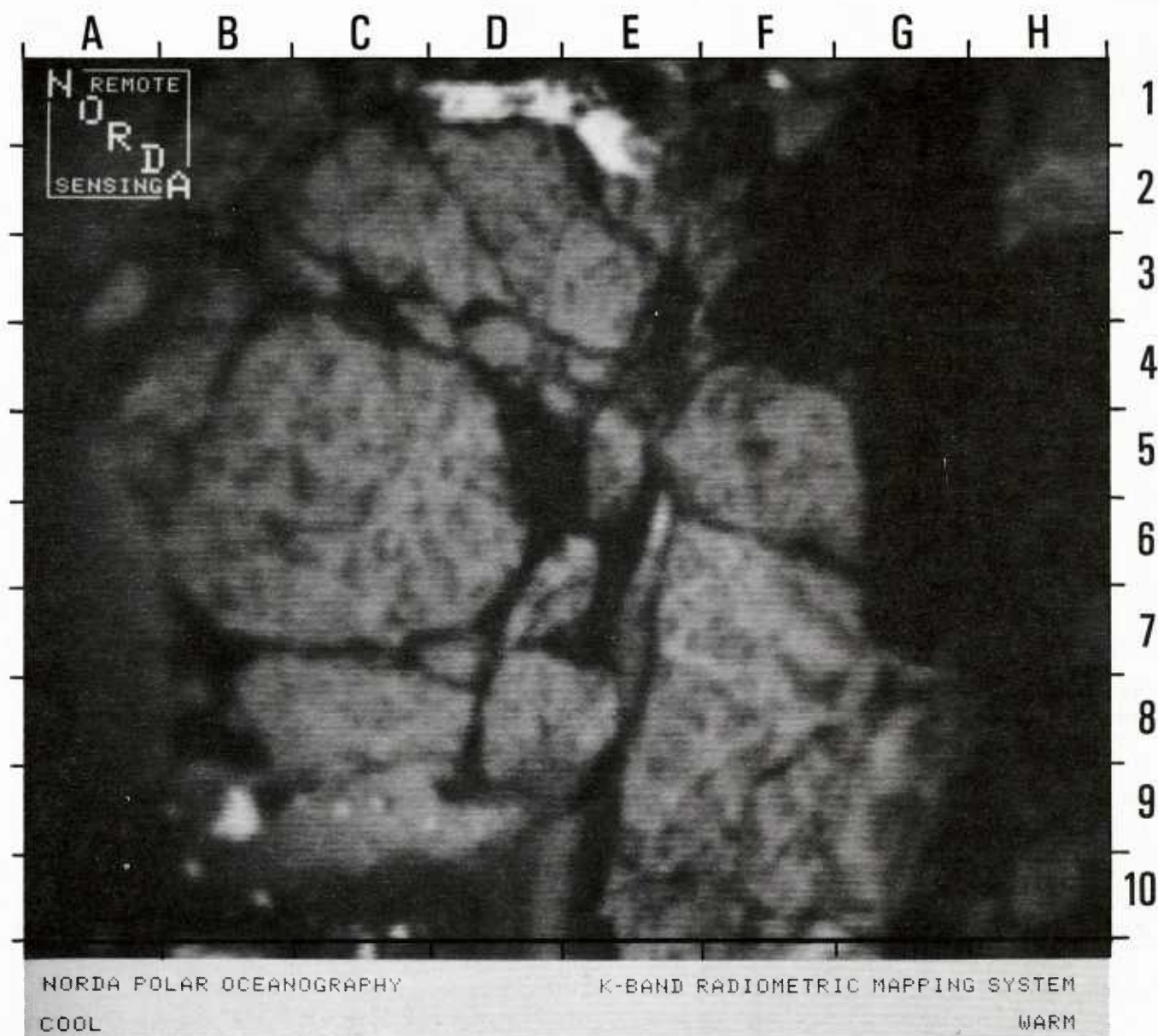
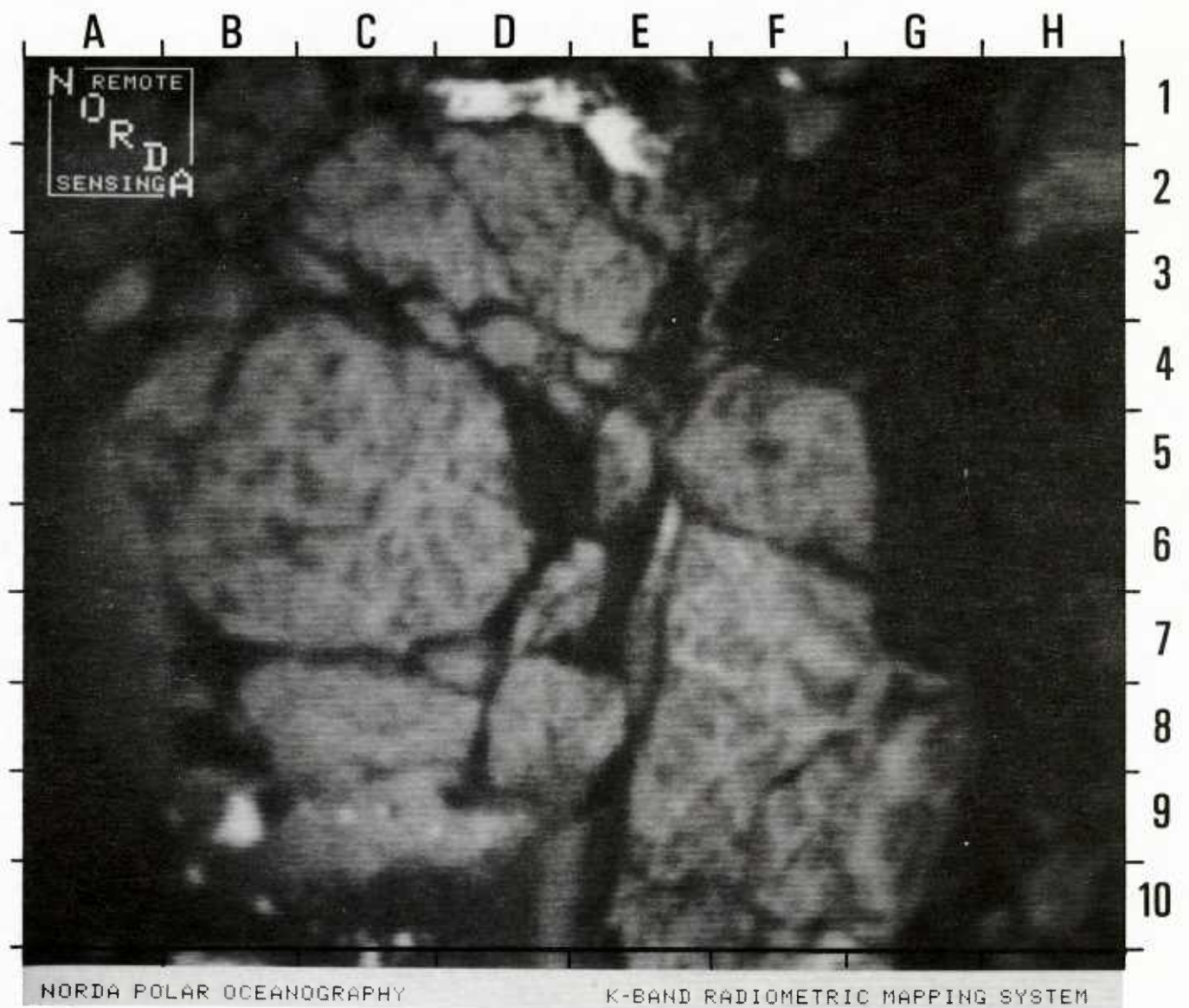


Figure 30a.

Figure 30. Differenced image of multi-year ice. An image in which multi-year ice predominates was imaged at 5000 ft (a) and 10,000 ft (b). The 10,000-ft image was registered to the 5000-ft image and subtracted. The resulting differenced image (c) represents features present on either image, but not on both images. Texture within multi-year floes that occurs at a scale visible at 5000 ft but not visible at 10,000 ft is enhanced.





*Figure 30b.*



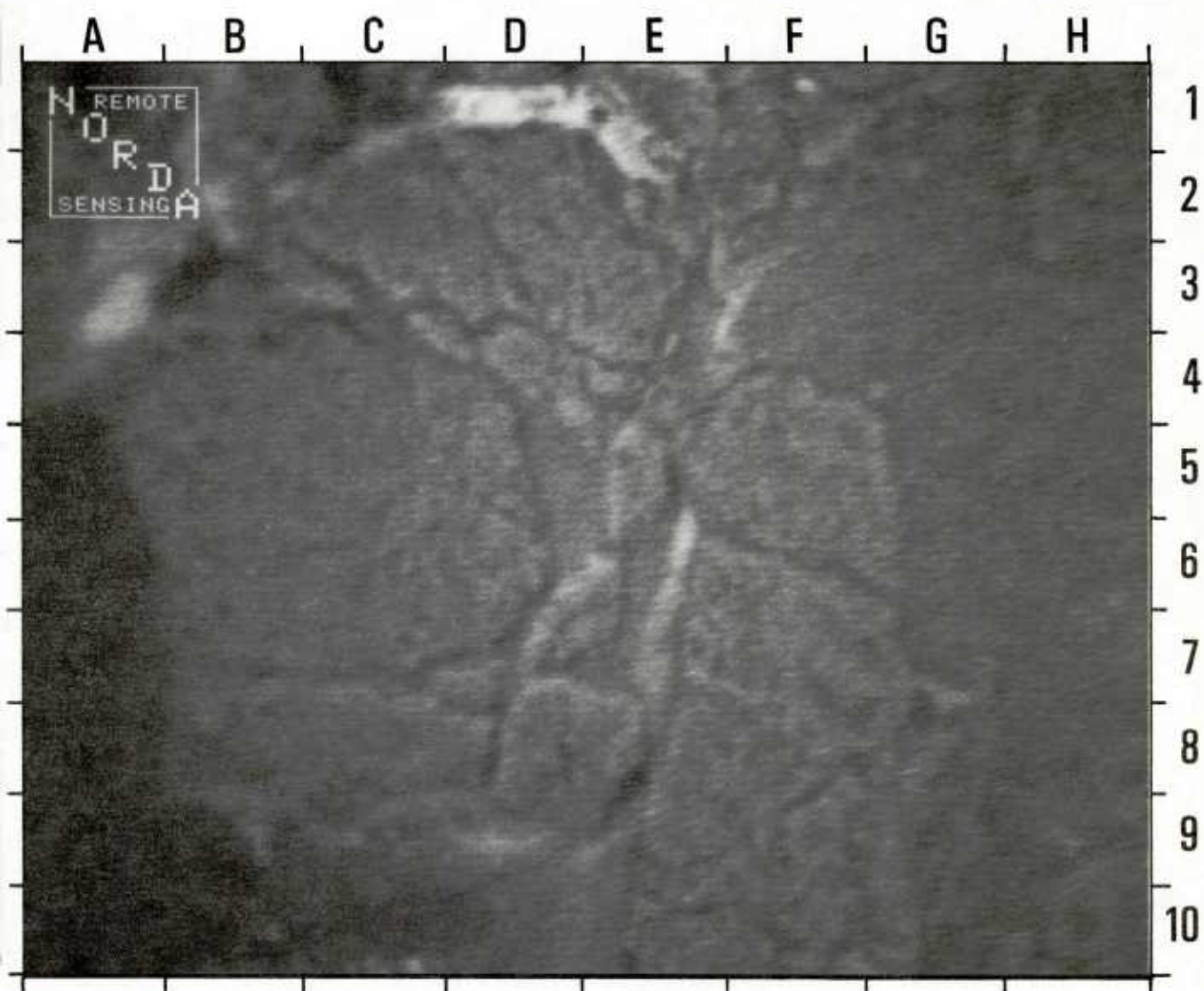


Figure 30c.



Figure 31a.

Figure 31. Differenced image of second-year ice. An image in which multi-year ice predominates was imaged at 5000 ft (a) and 10,000 ft (b). The 10,000-ft image was registered to the 5000-ft image and subtracted. The differenced image (c) highlights deformational features bordering floes. Otherwise, second-year floes are characterized by absence of texture in the differenced image. Textural differences between second-year ice and multi-year ice can be isolated using this technique.



Figure 31b.

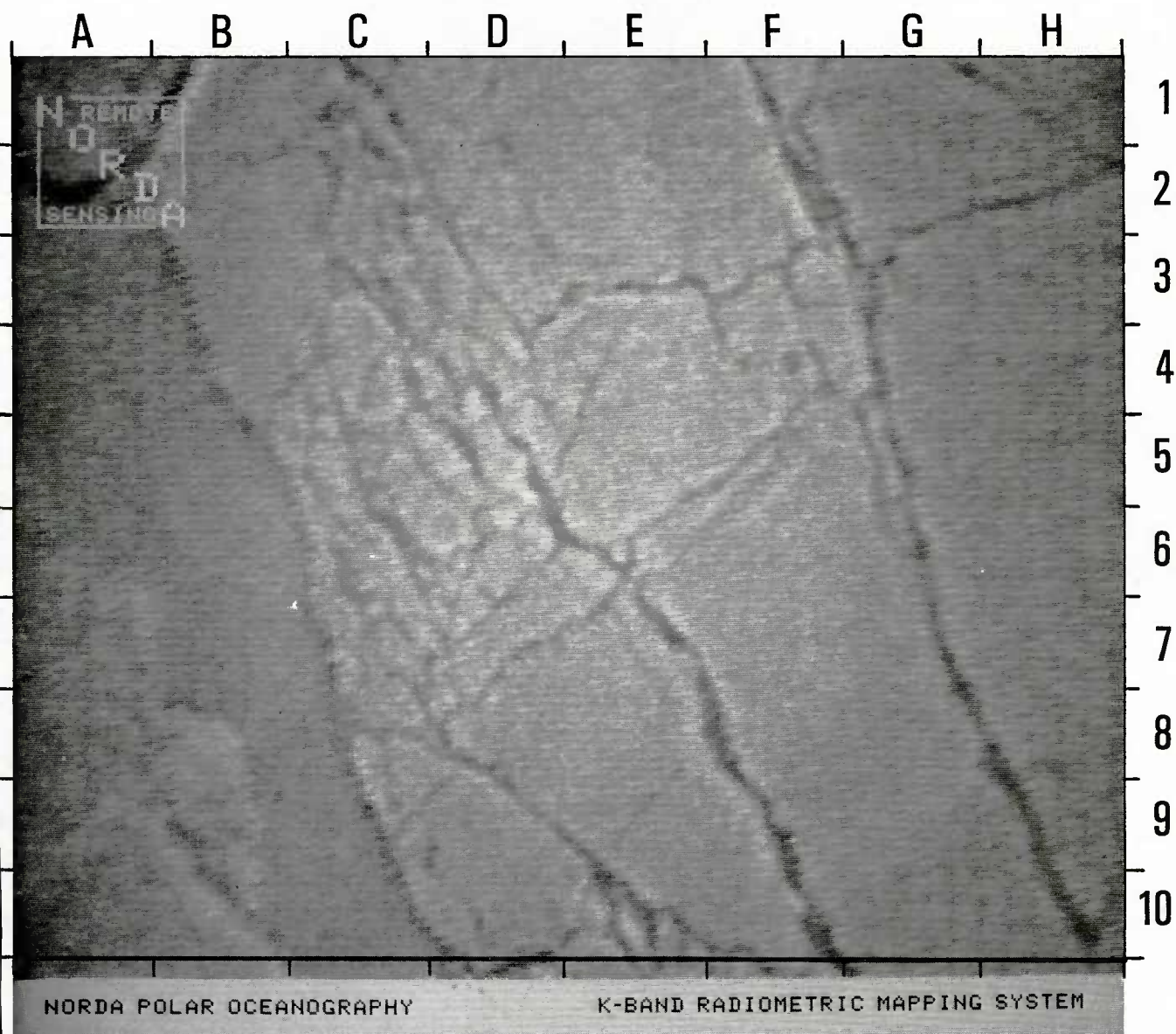


Figure 31c.



2. Measured brightness temperatures ( $K_a$ -band) that characterize four types of winter surfaces imaged in KRMS scenes fall within discrete ranges: 1) open water (135 K to 145 K), 2) new (frazil) (145 K to 155 K), 3) old ice (155 K to 200 K), and 4) young/first-year ice (210 K to 248 K). Discrimination between these surfaces can be achieved on the basis of measured  $K_a$ -band brightness temperature alone.

3. Winter brightness temperatures characteristic of nilas and new ice fall within a broad range (155 K to 224 K) that overlaps temperatures characteristic of old ice (155 K to 200 K) and, to a lesser extent, young ice and first-year ice (210 K to 248 K). Errors that arise from the presence of nilas and new ice are associated primarily with estimates of old ice concentration, but estimates of the young/first-year ice concentration may be affected as well. The presence of nilas and new ice inflates estimates of the amount of old ice that is present. Estimates of the young/first-year ice concentration, though more robust, are affected similarly if concentration estimates are based solely on measured brightness temperature data. However, textural differences observed in KRMS images between nilas/new ice and other ice types might permit unambiguous classification of scenes in which nilas and new ice are present if textural classifiers are used in conjunction with brightness temperature data.

4. Multi-year ice (168 K to 210 K) typically is radiometrically warmer than second-year ice (155 K to 195 K) in winter images analyzed here. Although multi-year ice and second-year ice can be readily discerned by visual means, overlap between brightness temperatures characteristic of multi-year and second-year ice precludes automated discrimination based on brightness temperature alone. Textural classifiers that describe meltponds and ridges that are common on multi-year floes but atypical of second-year floes might permit machine discrimination between multi-year and second-year ice.

5. Open water is, radiometrically, the coldest surface observed in any scene. Lack of overlap between brightness temperatures characteristic of other surfaces indicates that estimates of the areal extent of open water based on  $K_a$ -band brightness temperature alone are accurate.

6. The effect of incidence angle on measured brightness temperature, typically observed as generally higher brightness temperatures near image edges, can be removed from KRMS images without *a priori* knowledge of nadir brightness

temperatures of surfaces measured at off-nadir angles. Off-nadir brightness temperatures can be normalized to nadir values given incidence angle and measured off-nadir brightness temperature.

7. Ridge detection from KRMS data is complex and will require extensive surface investigation with coordinated KRMS overflights before acceptable answers can be provided. Analysis of the present data set, however, suggests several trends where ridge interpretation is concerned. First, where new ridges observed in photographs are correlative with lineaments on KRMS images, these lineaments are radiometrically warmer than surrounding ice. Second, where annealed ridges in old ice are correlative with lineaments in KRMS images, these lineaments are radiometrically colder than surrounding old ice. Finally, where extremely fresh, new ridges occur within a single ice type (versus fresh ridges between floes of different age), corresponding lineaments are not evident in KRMS images.

The classification scheme presented here is based on analysis of winter brightness temperature data collected over the Beaufort Sea. Although ice types classified within the scheme are not optimum in all cases (*e.g.*, young ice and first-year ice are lumped together), these preliminary results suggest that single-band brightness temperature data contain adequate information to allow development of semi-automated ice classification systems, at least for scenes imaged in winter. Inasmuch as surface conditions affect radiometric characteristics of imaged scenes, a classification scheme using these same brightness temperature intervals (Fig. 25) probably will not be effective if applied to nonwinter data from the Beaufort Sea or to data from other Arctic regions regardless of season. This is because breakpoints that define boundaries between ice types must be adjusted to account for radiometric differences brought about by seasonal and regional changes.

A comprehensive Arctic classification scheme that employs analytic methods used here thus will consist of a set of seasonal-regional classification algorithms. Each algorithm will be based on two or more variables (*e.g.*, brightness temperature, texture, or floe shape). We recognize that environments may well exist in which ice types cannot be classified adequately using single-band data. Such environments will become evident as new data are acquired and processed. We also recognize that a wealth of promising image processing techniques remain to be applied to ice classification problems. Some of these may succeed where conventional analyses of brightness temperature data fail.

## References

- Carsey, F. D. (1982). Arctic Sea Ice Distribution at the End of Summer 1973-1976 from Satellite Microwave Data. *Journal of Geophysical Research*, v. 87, n. C8, pp. 2032-2044.
- Cavalieri, D. J., S. Martin, and P. Gloersen (1983). Nimbus 7 SMMR Observations of the Bearing Sea Ice Cover During March, 1979. *Journal of Geophysical Research*, v. 88, n. C5, pp. 2743-2754.
- Comiso, J. C. (1983). Sea Ice Effective Microwave Emissivities from Satellite Passive Microwave and Infrared Observations. *Journal of Geophysical Research*, v. 88, n. C12, pp. 7686-7704.
- Comiso, J. C. and H. J. Zwally (1982). Antarctic Sea Ice Concentrations Inferred from Nimbus-5 ESMR and Landsat Imagery. *Journal of Geophysical Research*, v. 87, n. C8, pp. 5836-5844.
- Dunbar, M. and W. F. Weeks (1975). Interpretation of Young Ice Forms in the Gulf of St. Lawrence Using Side-Looking Airborne Radar and Infrared Imagery. CRREL Research Report 337, U.S. Army Cold Regions Research and Engineering Laboratory, Hanover, New Hampshire, 41 pp.
- Ehrlich, R. and B. Weinberg (1970). An Exact Method for the Characterization of Grain Shape. *Journal of Sedimentary Petrology*, v. 40, pp. 205-212.
- Ehrlich, R., P. J. Brown, J. M. Yarus, and D. T. Eppler (1980). Analysis of Particle Morphology Data, in Beddow, J. K. and Meloy, T. P., *Advanced Particulate Morphology*. CRC Press, Boca Raton, Florida, pp. 101-119.
- Full, W. E., R. Ehrlich, and J. E. Klovian (1981). EXTENDED Q-MODEL-Objective Definition of External End Members in the Analysis of Mixtures. *Mathematical Geology*, v. 13, n. 4, pp. 331-334.
- Full, W. E., R. Ehrlich, and J. C. Bezdek (1982). FUZZY Q-MODEL-A New Approach for Linear Unmixing. *Mathematical Geology*, v. 14, n. 3, pp. 259-270.
- Fung, A. K. and M. F. Chen (1981). Emission from an Inhomogeneous Layer with Irregular Interfaces. *Radio Science*, v. 16, n. 3, pp. 289-298.
- Gloersen, P., W. Nordberg, T. J. Schmugge, and T. T. Wilheit (1973). Microwave Signatures of First-Year and Multi-Year Sea Ice. *Journal of Geophysical Research*, v. 78, n. 18, pp. 3564-3572.
- Gloersen, P., T. T. Wilheit, T. C. Chang, W. Nordberg, and W. J. Campbell (1974). Microwave Maps of the Polar Ice of the Earth. *Bulletin American Meteorological Society*, v. 55, n. 12, pp. 1442-1448.
- Gloersen, P., H. J. Zwally, T. C. Chang, D. K. Hall, W. J. Campbell, and R. O. Ramseier (1978). Time Dependence of Sea-Ice Concentration and Multi-Year Ice Fraction in the Arctic Basin. *Boundary-Layer Meteorology*, v. 13, pp. 339-359.
- Gloersen, P., W. J. Campbell, and D. Cavalieri (1981a). Global Maps of Sea Ice Concentration, Age, and Surface Temperature Derived from Nimbus-7 Scanning Multichannel Microwave Radiometer Data: A Case Study, in Gower, J. F. R. (ed.), *Oceanography from Space*. Plenum Press, New York, pp. 777-783.
- Gloersen, P., D. Cavalieri, and W. J. Campbell (1981b). Derivation of Sea Ice Concentration, Age, and Surface Temperature from Multispectral Microwave Radiances Obtained with the Nimbus-7 Scanning Multichannel Microwave Radiometer, in Gower, J. F. R. (ed.), *Oceanography from Space*. Plenum Press, New York, pp. 823-829.
- Henderson, F. M. (1983). A Comparison of SAR Brightness Levels and Urban Land-Cover Classes. *Photogrammetric Engineering and Remote Sensing*, v. 49, n. 11, November 1983, pp. 1585-1591.
- Howard, S. J. (1981a). Method for Continuing Fourier Spectra Given by the Fast Fourier Transform. *J. Opt. Soc. Am.* 71, 3 pp.
- Howard, S. J. (1981b). Continuation of Discrete Fourier Spectra Using a Minimum-Negativity Constraint. *J. Opt. Soc. Am.* 71, 6 pp.
- Ketchum, R. D. and A. W. Lohanick (1977). Passive Microwave Signatures of Sea Ice Features. *NORDA Technical Note 9*, 16 pp.
- Ketchum, R. D., L. D. Farmer, and J. P. Welsh (1983). K-band Radiometric Mapping of Sea Ice. *NORDA Technical Note 179*, 18 pp.
- Kong, J. A., R. Shin, J. C. Shive, and L. Tsang (1979). Theory and Experiment for Passive Microwave Sensing of Snowpacks. *Journal of Geophysical Research*, v. 84, n. B10, pp. 5669-5673.
- Martin, S., D. J. Cavalieri, P. Gloersen, and S. L. McNutt (1982). The Bering Sea Ice Cover during March 1979: Comparison of Surface and Satellite Data with the Nimbus-7 SMMR. U.S. Department of Commerce Report, Contract MO-A01-78-00-4335, University of Washington, Seattle, 50 pp.
- Stephenson, G. G. (1983). A Description of the NORDA Satellite Remote Sensing Hardware/Software for Prospective Users. *NORDA Technical Note 205*, 96 pp.

Stogryn, A. (1970). The Brightness Temperature of a Vertically Structured Medium. *Radio Science*, v. 5, n. 12, pp. 1397-1406.

Stogryn A. (1981). Electromagnetic Properties of Random Media. Technical Report TR-1, Report Number 6140, Aerojet Electric Systems Company, Azusa, California, 115 pp.

Svendsen, E., K. Kloster, B. Farrelly, O. M. Johannessen, J. A. Johannessen, W. J. Campbell, P. Gloersen, D. Cavalieri, and C. Matzler (1983). Norwegian Remote Sensing Experiment: Evaluation of the Nimbus-7 Scanning Multichannel Microwave Radiometer for Sea Ice Research. *Journal of Geophysical Research*, v. 88, n. C5, p. 2781-2791.

Swift, C. T. (1980). Passive Microwave Remote Sensing of the Ocean—A Review, in Gower, J. F. R. (ed.), *Passive Radiometry of the Ocean*. D. Reidel Publ. Co., Boston, pp. 25-54.

Troy, B. E., J. P. Hollinger, R. M. Lerner, and M. M. Wisler (1981). Measurement of the Microwave Properties of Sea Ice at 90 GHz and Lower Frequencies. *Journal of Geophysical Research*, v. 86, n. C5, pp. 4283-4289.

Troy, B. E., J. P. Hollinger, M. F. Hartman, R. O. Ramseier, and S. A. Digby (1982). Preliminary Report on Passive Microwave and Millimeter-Wave Measurements of Arctic Sea Ice, October/November 1981. Naval Research Laboratory, NRL Memorandum Report 4861, 134 pp.

Weeks, W. F. and S. F. Ackley (1982). The Growth, Structure, and Properties of Sea Ice. CRREL Monograph 82-1, U.S. Army Cold Regions Research and Engineering Laboratory, Hanover, New Hampshire, 130 pp.

WMO (1970). WMO Sea-Ice Nomenclature. Secretariat of the World Meteorological Organization, Geneva, Switzerland, 147 pp.

Zwally, H. J. and P. Gloersen (1977). Passive Microwave Images of the Polar Regions and Research Applications. *Polar Research*, v. 18, pp. 431-450.

Zwally, H. J., C. L. Parkinson, F. D. Carsey, P. Gloersen, W. J. Campbell, R. O. Ramseier (1979). Seasonal Variation of Total Antarctic Sea Ice Area, 1973-1975. *Antarctic Journal of the United States*, v. 14, n. 5, p. 103.

# Appendix: Symbols

---

$A_R$	KRMS recorder attenuation level
$a$	effective radius of a scatterer
$d$	thickness of a dielectric layer
$\epsilon$	dielectric constant
$\epsilon_g$	dielectric constant of the ground
$\epsilon_0$	permittivity of free space
$\epsilon_r$	dielectric constant of a dielectric layer
$\epsilon_s$	dielectric constant of a spherical scatterers
$e$	emissivity
$e_p$	emissivity for polarization p
$F$	effective fractional volume of a scatterer
$f$	frequency
$G$	total gain (or attenuation) involved in reading the KRMS signal
$h$	horizontal polarization
$K$	constant to relate brightness temperature to measured KRMS voltage
$K_1$	constant associated with calibration of the cold reference source
$K_2$	constant associated with calibration of the hot reference source
$L$	fixed loss associated with KRMS circuit components
$L_A$	precision attenuator loss
$L_F$	feed loss
$L_J$	ferrite switch loss
$L_R$	radome loss
$R_p$	Fresnel coefficient for polarization p
$T_O$	physical temperature
$T_A$	precision attenuator temperature (radiometric)
$T_B$	brightness temperature (radiometric)
$T_F$	feed temperature (radiometric)
$T_H$	radiometric temperature of the heated calibration load
$T_h$	brightness temperature for horizontal polarization
$T_J$	ferrite switch temperature (radiometric)
$T_p$	radiometric brightness temperature for polarization p
$T_s$	antenna temperature (radiometric)



$T_{\text{sky}}$	sky temperature (radiometric)
$T_v$	brightness temperature for vertical polarization
$T_1$	radiometric temperature associated with the cold reference source
$T_2$	radiometric temperature associated with the hot reference source
$v$	vertical polarization
$V_D$	measured KRMS volts per digital pixel level
$V_m$	measured KRMS analog voltage
$\omega$	albedo
$\tau_d$	optical depth
$\theta$	incidence angle

## Distribution List

Mr. Charles Reeves  
Naval Scientific Intelligence Center  
3201 Suitland Road  
Washington, DC 20020

Mr. Quincy Robe  
U. S. Coast Guard  
R & D Center  
Avery Point  
Groton, CT 06340

International Ice Patrol  
U.S. Coast Guard  
R & D Center  
Avery Point  
Groton, CT 06340

Mr. Jan Zisko  
National Oceanic and Atmospheric Administration  
Office of Aircraft Operations  
P. O. Box 020197  
Miami, FL 33102-0197

LCDR Mike Stewart  
Operations Officer  
VXN-8  
Naval Air Station  
Patuxent River, MD 20670

Mr. Barry Dillon  
Naval Air Systems Command  
NAVAIR Code 340J  
Washington, DC 20361

Dr. Ronald L. Woodfin  
Systems Safety Technology Division  
Sandia National Laboratories  
Albuquerque, NM 87185

Director  
Canada Center for Remote Sensing  
Energy Mines & Resources Center  
ATTN: Dr. A. L. Gray  
2464 Sheffield Road  
Ottawa, Ontario K1A 0Y7  
Canada

Director  
Defence Research Board  
National Defense Headquarters  
ATTN: Dir. of Physics Research  
Ottawa 4 Ontario  
Canada

Director  
Intera Env. Consultants, Ltd.  
2841 Riverside Drive, Suite 204  
Ottawa, Ontario K1V 8N4  
Canada

Cold Regions Remote Sensing  
ATTN: Ms. Lyn Arsenault  
Box 526  
Stittsville, Ontario KOA 3G0  
Canada

Director  
National Aeronautics and Space Admin.  
Goddard Space Flight Center  
ATTN: Dr. P. Gloerson  
Greenbelt, MD 20771

Commander  
Naval Surface Weapons Center  
ATTN: Mr. M. Kleinerman  
White Oak, MD 20910

Director  
U. S. Geological Survey  
University of Puget Sound  
1500 N. Warner St.  
ATTN: Dr. W. J. Campbell  
Tacoma, WA 98416

Director  
ATTN: Mr. R. Larson  
Env. Res. Institute of Michigan  
P. O. Box 618  
Ann Arbor, MI 48107

Director  
Memorial Univ. of Newfoundland  
ATTN: J. Rossiter  
Elizabeth Avenue  
St. John's Newfoundland A1C 5X1  
Canada

F. G. Bercha & Associates  
ATTN: Dr. Lyn McNutt  
640 11th Avenue S.W.  
Calgary, Alberta T2R OE2  
Canada

Dr. F. Deily  
P. O. Box 2189  
Exxon Production Research Co.  
Houston, TX 77001

Mr. C. Durand  
R & D Center, Transport Canada  
Box 549  
1000 Sherbrooke St. W.  
Montreal, P. Q. H3A 2R3

Dr. P. Gudmandsen  
Electromagnetics Institute, Bldg. 348  
Technical Univ. of Denmark  
Dk 2800, Lyngby  
Denmark

Dr. R. K. Hawkins  
Dept. of Energy, Mines & Resources  
Canada Centre for Remote Sensing  
2464 Sheffield Rd.  
Ottawa, Ontario K1A 0Y7  
Canada

Mr. Brian Jonasson  
Petro-Canada  
1350 Guinness House  
727 7th Avenue, SW  
Calgary, Alberta T2P OZ6

Mr. T. Keliker  
Newfoundland Institute for Cold Ocean Science  
Memorial Univ. of Newfoundland A1B 3X7

Mr. W. Markham  
Ice Branch, Atmospheric Environmental Service  
4905 Dufferin St.  
Downsview, Ontario, M3H 5T4

Dr. B. Mercer  
Dome Petroleum  
P. O. Box 200  
Calgary, Alberta, T2P 2H8

Dr. Richard Moore  
Remote Sensing Laboratory  
University of Kansas  
2291 Irving Hue Drive  
Lawrence, KS 66045

Dr. G. Pilkington  
Gulf Canada CTD  
P. O. Box 150  
Calgary, Alberta T2P 2X6  
Canada

Mr. D. Schwab  
Gulf Resources Inc.  
Frontier Research  
Box 130  
Calgary, Alberta

Mr. G. Spedding  
ESSO  
Production Research Division  
ESSO Resources Canada  
339 50th Ave. S.W.  
Calgary, Alberta T2G 2B3

Dr. P. Teleki  
U.S. Geological Survey  
Office of Marine Geology  
USGS Mail Stop 915  
Reston, VA 22092

Mr. Raymond Godin  
Naval Polar Oceanography Center  
4301 Suitland Road  
Washington, DC 20390

Dr. Thomas Grenfell  
Department of Atmospheric Sciences  
University of Washington, AK-40  
Seattle, WA 98195

Mr. Charles A. Luther  
Office of Naval Research  
800 N. Quincy Street  
Arlington, VA 22217

Dr. Wilford F. Weeks  
USA CRREL  
72 Lyme Road  
Hanover, NH 03755

Dr. Lloyd Breslau  
USA CRREL  
72 Lyme Road  
Hanover, NH 03755

Technical Library  
USA CRREL  
72 Lyme Road  
Hanover, NH 03755

Dr. R. O. Ramseier  
Atmospheric Environment Service  
Department of Environment  
473 Albert Street  
Ottawa, Ontario K1A 0H3  
Canada

Dr. Bill Stringer  
Geophysical Institute  
U. of Alaska  
Fairbanks, Alaska 99701

Dr. Peter Wadhams  
Scott Polar Research Institute  
University of Cambridge  
Lensfield Road  
Cambridge CB2 1ER  
England

Dr. Drew Rothrock  
Polar Science Center  
University of Washington  
4057 Roosevelt Way, NE  
Seattle, WA 98105

Dr. Frank D. Carsey  
Mail Stop 183-501  
Jet Propulsion Laboratory  
4800 Oak Grove Drive  
Pasadena, CA 91109

Mr. Jim Cornelius  
Fleet Numerical Oceanography Center  
Monterey, CA 93943

Naval Research Laboratory  
ATTN: Dr. Robert Hayes  
4555 Overlook Avenue  
Southwest Washington  
Washington, DC 20375

Chief Naval Material Command  
ATTN: Mr. Charles J. Infosino  
Surface/Aerospace Surveillance  
Washington, DC

Defense Advanced Research Projects Agency  
(DARPA)  
ATTN: Mr. Sherman Karp  
Washington, DC

Chief Naval Operations  
OP-97C  
ATTN: Mr. Robert P. Moore  
Washington, DC

Department of Defense  
Mail Stop R732  
9800 Savage Road  
Fort Meade, MD

Naval Weapons Center  
NWC Code 3521  
China Lake, CA

Naval Weapons Center  
Technical Library  
NWC Code 343  
China Lake, CA

Commander  
Naval Ocean Systems Center  
Code 1603  
ATTN: Rod Buntzen  
San Diego, CA 92152

TRW  
One Space Park  
ATTN: James Eninger  
R1/1038  
Redondo Beach, CA 90278

Mr. Len Fedor  
NOAA/ERL/WPL, R/E/WP5  
325 Broadway  
Boulder, CO 80302

Officer in Charge  
Naval Underwater Systems Center  
ATTN: Dr. Peter Cable  
Code 01Y  
New London Laboratory  
New London, CT 06321

Department of the Navy  
Asst Secretary of the Navy  
(Research Engineering & System)  
Washington, DC 20350

NAVOCEANO VXN-8 Detachment  
Code 6421  
Naval Air Station  
Patuxent River, MD 20670

Department of the Navy  
Chief of Naval Operations  
ATTN: OP-951  
Washington, DC 20350



Department of the Navy  
Chief of Naval Operations  
ATTN: OP-952  
Washington, DC 20350

Department of the Navy  
Chief of Naval Operations  
ATTN: OP-987  
Washington, DC 20350

Department of the Navy  
Chief of Naval Material  
Washington, DC 20360

Commander  
Naval Air Development Center  
Warminster, PA 18974

Commander  
Naval Air Systems Command  
Headquarters  
Washington, DC 20361

Commander  
Naval Electronic Systems Com  
Headquarters  
Washington, DC 20360

Commanding Officer  
Naval Environmental Prediction Research Facility  
Monterey, CA 93940

Commanding Officer  
Naval Ocean Research and Development Activity  
ATTN: Codes 100/110/111/112  
NSTL, MS 39529

Commanding Officer  
Naval Ocean Research and Development Activity  
ATTN: Code 125L  
NSTL, MS 39529

Commanding Officer  
Naval Ocean Research and Development Activity  
ATTN: Code 300  
NSTL, MS 39529

Commanding Officer  
Naval Ocean Research and Development Activity  
ATTN: Code 115T  
NSTL, MS 39529

Commanding Officer  
NORDA  
ATTN: Code 200  
NSTL, MS 39529

Commanding Officer  
Naval Research Laboratory  
Washington, DC 20375

Commander  
Naval Oceanography Command  
NSTL, MS 39529

Commanding Officer  
Fleet Numerical Ocean Cen  
Monterey, CA 93940

Commanding Officer  
Naval Oceanographic Office  
NSTL, MS 39522

Commander  
Naval Ocean Systems Center  
San Diego, CA 92152

Commander  
Naval Sea System Command  
Headquarters  
Washington, DC 20362

Commander  
Naval Surface Weapons Center  
Dahlgren, VA 22448

Commanding Officer  
Naval Underwater Systems Center  
ATTN: NEW LONDON LAB  
Newport, RI 02841

Superintendent  
Naval Postgraduate School  
Monterey, CA 93940

Project Manager  
ASW Systems Project (PM-4)  
Department of the Navy  
Washington, DC 20360

Defense Technical Info Cen  
ATTN: DTIC-DDAC  
Cameron Station  
Alexandria, VA 22314

Director, Liaison Office  
Naval Ocean Research and Development Activity  
800 N. Quincy Street  
Ballston Tower #1  
Arlington, VA 22217

Woods Hole Oceanographic Inst  
86-96 Water St.  
Woods Hole, MA 02543

Director  
University of California  
Scripps Institute of Oceanography  
P. O. Box 6049  
San Diego, CA 92106

Working Collection  
Texas A & M University  
ATTN: Dept of Ocean Working Collection  
College Station, TX 77843

Department of the Navy  
Chief of Naval Research  
ATTN: Dr. Dennis Conlon  
800 N. Quincy Street  
Arlington, VA 22217

Department of the Navy  
Chief of Naval Research  
ATTN: OP-952E, CDR D. Honhart  
800 N. Quincy Street  
Arlington, VA 22217

Commanding Officer  
Naval Environmental Prediction Research Facility  
ATTN: Mr. Bob Fett  
Monterey, CA 93940

Superintendent  
Naval Postgraduate School  
ATTN: Ocean Dept., Dr. J. Mueller  
Monterey, CA 93940

Superintendent  
Naval Postgraduate School  
ATTN: Ocean Dept., Dr. S. Tucker  
Monterey, CA 93940

Chief  
Earth Resources Lab  
ATTN: Mr. D. Mooneyhan  
NSTL, MS 39529

Director  
National Aeronautics & Space Adm  
Goddard Space Flight Center  
ATTN: CDR R. Kirk  
Greenbelt, MD 20771

Director  
National Aero & Space Admin.  
Headquarters  
ATTN: D. Broome  
Washington, DC 20546

Chief of Naval Material  
Office of Naval Technology  
ATTN: MAT-0724, CAPT E. Young  
800 N. Quincy Street  
Arlington, VA 22217

Director  
National Oceanic & Atmos Admin  
ATTN: A. F. Rock  
6010 Exec. Blvd.  
Rockville, MD 20852

Director  
Woods Hole Oceanographic Inst.  
Woods Hole, MA 02543

Executive Director  
Bigelow Lab for Ocean Sciences  
McKown Point  
ATTN: Dr. C. Yentsch  
W. Boothbay Harbor, ME 04575

President  
University of Wisconsin  
ATTN: Env. Studies Inst.,  
Dr. J. L. Scarpace  
1225 West Dayton Street  
Madison, WI 53706

President  
University of Miami  
RSMAS  
ATTN: Ctr for Mar. Studies,  
Dr. O. Brown  
4600 Rickenbacker Causeway  
Miami, FL 33149

President  
University of Miami  
ATTN: Dr. H. Gordon  
Coral Gables, FL 33124

Director  
Bedford Inst of Oceanography  
ATTN: Atl Ocean Lab,  
Dr. R. Hendry  
Dartmouth NOVA SCOTIA B7Y 4A2  
Canada

Director  
Instituto Espanol de Oceanographia  
ALCALA 27-40  
ATTN: Cristina G. Gernandez  
MADRID  
SPAIN

Ingenieur de la Meteorologie  
Chef de Centre de Meteorologie  
ATTN: Michele C. Philippe  
LANNION 22300  
FRANCE

Director  
DFVLR  
Nachrichtentechnik und Erkundung  
ATTN: Heinz vander Peipen  
D-8031 Wessling/Obb  
WEST GERMANY

Naval Ocean R & D Activity  
ATTN: Code 321 - Nita Chase  
Code 321 - Sam Oriol  
Code 321 - Jeff Hawkins  
Code 321 - Gerry Stephenson  
NSTL, MS 39529

Computer Science Corp  
ATTN: Hillary Mesic  
NSTL, MS 39529

U216944